

## Mechanisms of short pitch rail corrugation

Li, S.

**DOI**

[10.4233/uuid:ee0e14ec-c4b2-4bcf-81cf-d09c3bb8b8c1](https://doi.org/10.4233/uuid:ee0e14ec-c4b2-4bcf-81cf-d09c3bb8b8c1)

**Publication date**

2022

**Document Version**

Final published version

**Citation (APA)**

Li, S. (2022). *Mechanisms of short pitch rail corrugation*. [Dissertation (TU Delft), Delft University of Technology]. <https://doi.org/10.4233/uuid:ee0e14ec-c4b2-4bcf-81cf-d09c3bb8b8c1>

**Important note**

To cite this publication, please use the final published version (if applicable).  
Please check the document version above.

**Copyright**

Other than for strictly personal use, it is not permitted to download, forward or distribute the text or part of it, without the consent of the author(s) and/or copyright holder(s), unless the work is under an open content license such as Creative Commons.

**Takedown policy**

Please contact us and provide details if you believe this document breaches copyrights.  
We will remove access to the work immediately and investigate your claim.

# **Mechanisms of short pitch rail corrugation**

***Shaoguang LI***



# Mechanisms of short pitch rail corrugation

Dissertation  
for the purpose of obtaining the degree of doctor  
at Delft University of Technology  
by the authority of the Rector Magnificus Prof.dr.ir. T.H.J.J. van der Hagen;  
Chair of the Board for Doctorates  
to be defended publicly on  
Wednesday 12 January 2022 at 15:00 o'clock

By

***Shaoguang LI***

Master of Engineering in Mechatronics, Northeastern University, China  
Born in Henan, China

This dissertation has been approved by the promotor.

Composition of the doctoral committee:

Rector Magnificus,	Chairperson
Prof.dr. Z. Li	Delft University of Technology, promotor
Prof.dr.ir. R.P.B.J. Dollevoet	Delft University of Technology, promotor

Independent members:

Prof. dr.ir. J. Sietsma	Delft University of Technology
Prof.dr. W. Zhu	University of Maryland, Baltimore County
Prof.dr. R. Chen	Southwest Jiaotong University
Prof. dr. ir. E.G. Vadillo	University of the Basque Country
Prof.dr. M. Veljkovic	Delft University of Technology

This dissertation was financially supported by:



ISBN: 978-94-6384-283-9

Printed by: Gildeprint - Enschede

Copyright © 2022 by Shaoguang Li ([shaoguangli2016@gmail.com](mailto:shaoguangli2016@gmail.com))

An electronic copy of this dissertation is available at <http://repository.tudelft.nl/>

*To my family*  
致我的家人



## SUMMARY

Short pitch corrugation is a (quasi-) sinusoidal rail vertical defect on rail surface, and it was first found more than one century ago. The wavelength of short pitch corrugation is 20-80 mm, and its amplitude can be up to 100  $\mu\text{m}$ . It mainly develops on straight tracks or at gentle curves with comparatively light axle loads. Due to short pitch corrugation, dynamic wheel-rail contact forces increase considerably, and hence the degradations of vehicle-track components are accelerated. In addition, the corrugation excited vibration is a source that radiates “roaring” noise.

Because of those negative aspects, researchers have spent many efforts to understand and theoretically explain the problem. At present, the corrugation phenomenon is usually understood through a damage mechanism and a wavelength-fixing mechanism. Based on the explanation, almost all types of corrugations can be explained with their corresponding mechanisms, and countermeasures were confirmed to be capable of effectively mitigating them. Nevertheless, there has been yet no consensus on the mechanisms of short pitch corrugation due to: 1) it only appears at some tracks and some locations, 2) different from other types of corrugation, short pitch corrugation (after this shortened as “corrugation”) changes minorly with the change in train speed.

In this dissertation, a three dimensional (3D) dynamic finite element (FE) vehicle-track frictional rolling contact model, which was initially used to research rail squats, is extended to understand the corrugation enigma. The goal is to investigate if the model can explain the root causes of the corrugation. A second goal is to characterize the rail material damages from rail corrugation metallurgically.

After an introduction, the 3D dynamic FE vehicle-track frictional rolling contact model is applied to rail corrugation research. The damage mechanism evaluated is differential wear, and it is considered proportional to the frictional work. Nominal parameters and boundary conditions are used in the model. Corrugations with different phase angles are added to the rail model to investigate whether they can consistently grow. Similar to conclusions from previous research, the obtained differential wear is in phase with the corrugation, which means the corrugation will be worn off and not grow. Nevertheless, it is found that the longitudinal track vibration modes may be dominant for short pitch corrugation initiation, and the vertical modes become dominant at certain stages. The consistency of longitudinal and vertical contact forces, differential wear, and corrugation should determine the development of short pitch corrugation.

Then in the second part of this thesis, through the variation of fastening modeling, an initial differential wear with large amplitudes is identified to form from the smooth rail. This differential wear is found to be correlated to the rail longitudinal dynamics. The corrugation



explained by this differential wear can consistently initiate and grow up to 80  $\mu\text{m}$ . Additionally, the corrugation from the numerical analysis agrees well with a rail corrugation recorded from the field. Consistency is shown during the corrugation growth between the vertical and longitudinal contact force, the differential wear, and the corrugation. Besides, a corrugation wavelength selection phenomenon can also be explained by this consistency. These results confirm the insights from the first part of the thesis, reveal the whole development process of corrugation, and explain its root cause.

The third part of this thesis is a study of the rail material structural damage from a corrugation. A metallurgical study was performed to analyze the rolling contact fatigue damage of a rail sample with corrugation. Besides the well-known white etching layer (WEL), an extra layer called the brown etching layer (BEL) was identified with distinctly lower hardness and brown colour contrast. It bears some similar properties as the WEL, such as brittle though much softer. Compared to WEL, the cracks formed in the BEL were found to propagate downwards without branching and can lead to rail fracture in the end. It is unknown if the BEL is a transitional state from the pearlite structure to the WEL, if it forms after the WEL, or if it is a different layer formed under certain thermomechanical conditions.

In conclusion, this thesis extends a 3D dynamic FE vehicle-track rolling contact model for the mechanism of corrugation study. Based on the research results, the root cause of the corrugation found on the Dutch railway network is identified. This finding opens the possibility to design methods to avoid or mitigate corrugation by optimising track structure parameters. Finally, the finding of BEL brings a new concept that will help to understand the rail material damage mechanisms from rail corrugation. The understanding of BEL will provide insight into crack development mechanisms, as BEL can lead to rail fracture. A complete understanding of rail material is crucial for the development of new rail technologies.

## SAMENVATTING

Golfslijtage is een verticaal (quasi-)sinusoïdaal defect op het railoppervlak en werd meer dan een eeuw geleden voor het eerst gevonden. De golflengte van golfslijtage is 20-80 mm en de amplitude kan tot 100  $\mu\text{m}$  bedragen. Het ontwikkelt zich voornamelijk op rechte sporen of in flauwe bochten met relatief lichte asbelasting. Vanwege golfslijtage neemt de dynamische contactkracht tussen wiel en rail aanzienlijk toe, waardoor de degradatie van voertuig- en spoorcomponenten wordt versneld. Bovendien is de door golfslijtage opgewekte trilling ook een bron van een 'brullend' geluid.

Vanwege die negatieve aspecten hebben onderzoekers veel moeite gedaan om het probleem te begrijpen en theoretisch te verklaren. Tegenwoordig wordt het verschijnsel van golfslijtage gewoonlijk begrepen via een schademechanisme en een golflengte-bevestigingsmechanisme. Op basis van deze verklaring kan bijna elk type golfslijtage worden beschreven aan de hand van de bijbehorende mechanismen, en is bevestigd dat deze effectief kunnen worden aangepakt met tegenmaatregelen. Toch is er nog geen consensus over de mechanismen van golfslijtage, omdat: 1) het slechts op bepaalde sporen en bepaalde locaties voorkomt, 2) in tegenstelling tot andere typen golfslijtage, verandert golfslijtage nauwelijks naarmate de treinsnelheid verandert.

In dit proefschrift wordt een dynamisch, driedimensionaal (3D) model van eindige elementen (FE) voor het wrijvingscontact tussen voertuig en spoorbaan, dat aanvankelijk werd gebruikt voor onderzoek naar 'squats' in het spoor, uitgebreid om het raadsel van de golfslijtage te begrijpen. Het doel is om te onderzoeken of het model de grondoorzaken van de golfslijtage te kan verklaren. Een tweede doel is om de schade aan het spoorwegmateriaal als gevolg van de golfslijtage metallurgisch te karakteriseren.

Na een introductie wordt een dynamisch 3D-model FE voor het wrijvingscontact tussen voertuig en spoor toegepast in het onderzoek naar golfslijtage op het spoor. Het schademechanisme is differentiële slijtage, en wordt beschouwd als evenredig met de wrijvingsarbeid. In het model worden nominale parameters en randvoorwaarden gebruikt. Golven met verschillende fasehoeken worden aan het railmodel toegevoegd om te onderzoeken of zij consistent kunnen groeien. Vergelijkbaar met conclusies uit eerder onderzoek, bevindt de verkregen differentiële slijtage zich in dezelfde fase als de golf, wat betekent dat de golf zal worden afgesleten en niet zal groeien. Desondanks is gebleken dat de longitudinale trillingswijzen van het spoor dominant kunnen zijn bij het ontstaan van golfslijtage, en dat de verticale trillingswijzen in bepaalde stadia dominant worden. De consistentie van longitudinale en verticale contactkrachten, differentiële slijtage en golfslijtage zou bepalend moeten zijn voor de ontwikkeling van golfslijtage.

Dan in het tweede deel van dit proefschrift, gebaseerd op de variatie van bevestigingssysteem-modellering, vormt zich een initiële differentiële slijtage met grote amplituden van de vlakke rail. De differentiële slijtage blijkt gecorreleerd te zijn met de rail

longitudinale dynamiek. De golfslijtage door de differentiële slijtage kan gelijkmatig ontstaan en tot 80  $\mu\text{m}$  aangroeien. Daarbij komt dat de golfslijtage uit de numerieke analyse goed overeenkomt met een in het veld geregistreeerde golfslijtage van het spoor. De consistentie wordt getoond tijdens de groei van de golfslijtage in de verticale en longitudinale contactkracht, de differentiële slijtage en golfslijtage. Bovendien kan een fenomeen van golflengteselectie ook worden verklaard door de consistentie. Deze resultaten bevestigen de inzichten uit het eerste deel van het proefschrift, onthullen het hele ontwikkelingsproces van golfslijtage en verklaren de oorzaak ervan.

Het derde deel is een studie van de structurele schade aan het spoormateriaal door golfslijtage. Er werd een metallurgische studie uitgevoerd om de vermoeiingsschade door rolcontacten van een railmonster met golfslijtage te analyseren. Naast de bekende witte etslaag (WEL) werd een extra laag, genaamd de bruine etslaag (BEL), geïdentificeerd met een duidelijk lagere hardheid en het bruine kleurcontrast. Het heeft een aantal vergelijkbare eigenschappen als de WEL, zoals broos, maar veel zachter. Vergeleken met WEL bleken de in de BEL gevormde scheuren zich naar beneden toe te verspreiden, zonder vertakking, en kunnen zij uiteindelijk leiden tot een spoorstaafbreek. Het is niet bekend of de BEL een overgangstoestand is van de perlietstructuur naar de WEL, of deze zich na de WEL vormt, dan wel of het een andere laag is die onder bepaalde thermomechanische omstandigheden wordt gevormd.

Concluderend breidt dit proefschrift een dynamisch 3D-model FE voor het wrijvingscontact tussen voertuig en spoor uit met het mechanisme van golfslijtage. Op basis van de onderzoeksresultaten wordt de hoofdoorzaak van de golfslijtage op het Nederlandse spoorwegnet vastgesteld. Deze bevinding opent de mogelijkheid om methoden te ontwerpen om golfslijtage te voorkomen of te verminderen door de parameters van de spoorstructuur te optimaliseren. Ten slotte brengt de bevinding van BEL een nieuw concept met zich mee dat zal helpen bij het begrijpen van de railmateriaal schademechanismen van het spoor door golfslijtage. Het begrip van BEL zal inzicht verschaffen in scheurontwikkelingsmechanismen, aangezien BEL kan leiden tot spoorbreek. Een volledig begrip van spoormateriaal is cruciaal voor de ontwikkeling van nieuwe spoortechnologie.

## CONTENTS

<b>Summary .....</b>	<b>i</b>
<b>Samenvatting .....</b>	<b>iii</b>
<b>Contents .....</b>	<b>v</b>
<b>Introduction .....</b>	<b>1</b>
1.1 Motivation .....	2
1.2 Overview of short pitch corrugation .....	2
1.3 Consequences of corrugation.....	3
1.4 Numerical-approach studies on corrugation.....	5
1.4.1 Modelling of vehicle-track dynamics .....	5
1.4.2 Modelling of wheel-rail contact mechanics .....	6
1.4.3 Numerical analysis of wear .....	8
1.5 Metallurgical investigation on corrugated rail materials .....	9
1.6 Problem statement.....	10
1.7 Outline of the dissertation .....	11
References.....	12
<b>2. New insights into the short pitch corrugation enigma based on 3D-FE coupled dynamic vehicle-track modelling of frictional rolling contact .....</b>	<b>15</b>
2.1 Introduction.....	16
2.2 Model .....	20
2.2.1 FE model.....	20
2.2.2 Corrugation model .....	23
2.2.3 Validity of the model.....	25
2.3 Contact solutions at corrugation.....	26
2.3.1 Normal contact .....	26
2.3.2 Tangential contact.....	29
2.4 Wear and corrugation simulation.....	31

## Contents

---

2.4.1 Wear model .....	31
2.4.2 Prediction of major field observations.....	32
2.4.3 Analysis of longitudinal and vertical rail modes.....	34
2.4.4 Additional comments .....	36
2.5 Relationship between contact forces and wear as well as new insights.....	37
2.5.1 Normal and longitudinal forces do not exactly follow corrugation in wavelength and phase.....	37
2.5.2 Preferred frequency of contact forces .....	38
2.5.3 Frequencies converge to develop uniform corrugation .....	40
2.5.4 Importance of the proposed modelling approach and track parameters .....	41
2.5.5 Additional discussions .....	42
2.6 Conclusions and future work.....	43
References.....	45
<b>3. Mechanism of short pitch corrugation: initial excitation and consistency condition for initiation and growth .....</b>	<b>49</b>
3.1 Introduction.....	50
3.1.1 Problem statement and literature review .....	50
3.1.2 Gap to bridge: Identify an initial excitation for corrugation initiation and a condition for consistent growth .....	51
3.1.3 Structure of this paper .....	52
3.2 Hypothesis for a consistent corrugation initiation and growth process .....	53
3.3 Model and methods .....	55
3.3.1 FE model.....	55
3.3.2 Railpad models.....	57
3.3.3 Wear model .....	58
3.4 Corrugation initiation .....	59
3.4.1 The initial excitation.....	59
3.4.2 Initial differential wear.....	59
3.4.3 Longitudinal force dominates the corrugation initiation .....	61

3.5 Corrugation consistent growth.....	63
3.5.1 Consistency between $2A_{\max} = 0$ and $10\ \mu\text{m}$ .....	63
3.5.2 Consistency when $2A_{\max} > 10\ \mu\text{m}$ .....	63
3.5.3 Wavelength selection and fixing.....	71
3.5.4 Relation with eigen frequencies .....	71
3.5.5 Summary .....	71
3.6 The corrugation-initiating wear is caused by rail longitudinal compression modes .	72
3.6.1 Vertical rail bending is not responsible for the corrugation initiation .....	72
3.6.2 Longitudinal rail shear is not responsible for the corrugation initiation .....	75
3.6.3 The corrugation-initiating wear is caused by longitudinal rail modes .....	78
3.6.4 Influence of rail inclination is negligible.....	78
3.7 Conclusions.....	81
References.....	82
<b>4. “Brown etching layer”: a possible new insight into the crack initiation of rolling contact fatigue in rail steels? .....</b>	<b>87</b>
4.1 Introduction.....	88
4.2 Sample description and experimental details .....	90
4.2.1 Sample.....	90
4.2.2 Specimen preparation and experimental tools .....	92
4.3 Experimental results.....	92
4.3.1 Microstructural features of the BEL in OM .....	92
4.3.2 Micro-hardness test .....	94
4.3.3 Microstructural features of BEL in SEM .....	95
4.3.4 BEL and cracks.....	98
4.4 Discussion .....	99
4.5 Summary.....	103
References.....	104
<b>5. Conclusions, applications and recommendations.....</b>	<b>107</b>

**Contents**

---

5.1 Conclusions..... 108

5.2 Applications of research findings ..... 110

5.3 Recommendations for future research ..... 111

References..... 111

**Acknowledgement .....113**

**Curriculum vitae .....115**

**List of publications .....117**

# 1

## INTRODUCTION



### 1.1 Motivation

Rail corrugation is a periodic wave-like rail top surface defect. Among the different types of rail corrugations defined by their damage mechanism and wavelength-fixing mechanism [1], the development of short pitch corrugation and its root causes remain elusive. This thesis aims to investigate the mechanism of a short pitch corrugation observed from the Dutch railway network with a three-dimension (3D) transient finite element (FE) vehicle-track frictional contact model and understand rail material damages from short pitch corrugation.

### 1.2 Overview of short pitch corrugation

Short pitch corrugation is a periodic wave-like rail top surface defect. It mainly develops on straight tracks or at gentle curves with comparably light axle load. The wavelength of short pitch corrugation is 20-80 mm, and it changes minorly with train speed change. The amplitude of short pitch corrugation can be up to 100  $\mu\text{m}$ .

Short pitch corrugation is usually explained and identified by two mechanisms: 1) damage mechanism and 2) wavelength-fixing mechanism. Wear is usually considered the main damage mechanism. The wavelength-fixing mechanism for most types of corrugations is a frequency-fixing mechanism with the wavelength  $\lambda$  governed by the equation

$$\lambda = \frac{v}{f} \quad (1.1)$$

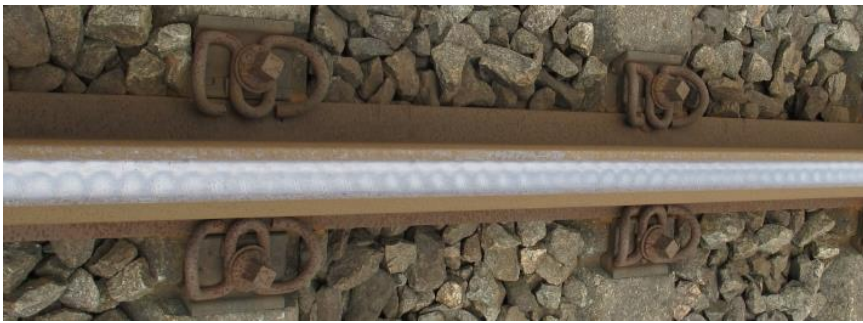
where  $v$  is the train speed, and  $f$  is the frequency corresponding to certain structural dynamics [1].

Based on this explanation, the wavelength of corrugation will linearly vary with the train speed. This mechanism can be used to explain most types of corrugations except for short pitch corrugation. Field data indicated that the short pitch corrugation wavelength is relatively insensitive to train speed changes [1, 2].

Fig. 1.1 shows an example of the short pitch corrugation (subsequently called corrugation for short) observed from the Dutch railway network. It can be seen from the three subfigures that the corrugation can be uniform in wavelength and distributes evenly along a sleeper span, or its wavelength or amplitude can vary to some extent.



(a) Uniform corrugation.



(b) A non-uniform corrugation of varying amplitudes.



(c) A non-uniform corrugation of varying wavelengths.

**Fig. 1.1.** Short pitch corrugation on the Dutch railway network.

### 1.3 Consequences of corrugation

The presence of rail corrugation can increase vehicle-track vibrations. These vibrations will negatively affect the rail profile and shorten the service life of relevant railway track system

## 1 Introduction

components. Fig 1.2 shows the fracture of fastening clips due to the presence of the corrugation. In worst scenarios, particularly critical in high-speed operations, the continuous loose and fracture of the fastening clips will oblige major maintenance activities as an increase in the risk of derailment will be experienced. In [3], it is reported that the corrugation is closely correlated to rolling contact fatigue (RCF), e.g., rail squats, which is accompanied by cracks (see Fig 1.3). The transverse propagation of cracks can finally result in rail fracture if maintenance is not conducted regularly.



**Fig. 1.2.** Fracture of fastening clips

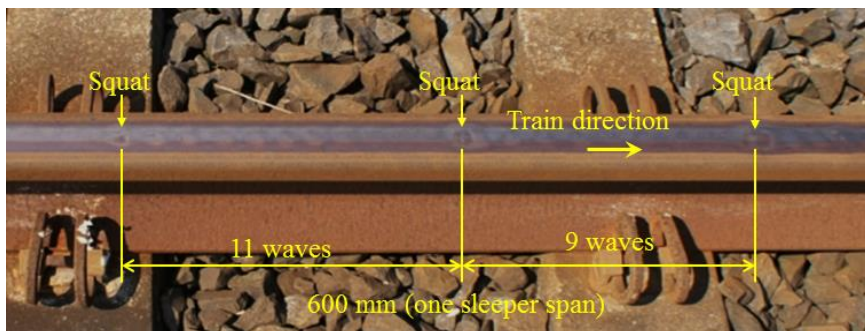


**Fig. 1.3.** Rail squats by corrugation

In addition, when trains are passing by railway tracks with corrugation, high levels of “roaring” noise is generated. Thus, corrugation brings noise pollution that affects (among others) the resident living nearby the railway tracks. This noise can be particularly critical for those metro lines running through densely inhabited districts.

## 1.4 Numerical-approach studies on corrugation

The corrugation development consists of three elements: 1) structural dynamics excitation caused by vehicle-track interactions, 2) loading response at the wheel-rail interface involving contact mechanics, and 3) feedback from contact mechanics and damage mechanisms to the structural dynamics as determined by the direct coupling between the contact mechanics and structural dynamics. Therefore, the modelling of vehicle-track dynamics coupled through contact mechanics and the consideration of damage mechanisms are essential to understand the corrugation problem.

### 1.4.1 Modelling of vehicle-track dynamics

In order to understand the mechanisms of corrugation, the following aspects are considered in the formulation of the vehicle-track dynamic interaction model. Firstly, the vibration of the structures, including the car body and bogie as rigid bodies, is usually designed not to be higher than 10 Hz [4]. This is from the consideration of ride comfort and to reduce dynamic loads from those heavy sprung structures. When it comes to the relevant vibrations related to corrugation, the frequency is usually in the order of hundreds Hz, which is much higher than the vibrations above the primary suspension. At those frequencies, the unsprung wheelset vibration becomes isolated from the vibrations of the bogie and car body through the primary suspension [4]. Therefore, it is reasonable to simplify the structure as a sprung mass supported by the primary suspension. The sprung mass above a half wheelset is 1/8 of the sprung dynamic load of a whole vehicle, which is approximately a quarter of the sprung mass carried by a bogie.

Secondly, corrugation predominantly occurs on straight tracks or at gentle curves. In those cases, the vehicle-track dynamics can be approximately assumed to distribute symmetrically at both sides of the rail, i.e., without consideration of lateral dynamics. Therefore, only a half-track structure and a half wheelset are considered. The primary suspension, the fastening system, and the ballast are modelled as parallel spring-damper elements, while the wheel, rail, and sleepers are modelled with 8-node solid elements considering their correspondingly nominal profiles. Additionally, by modelling them as three dimensional (3D) solid elements, the vehicle and the track structure are coupled with a contact model, which will be explained in the following section. Coulomb's frictional law is employed to study the frictional rolling contact problem. Fig. 1.4 shows a schematic diagram of the model.

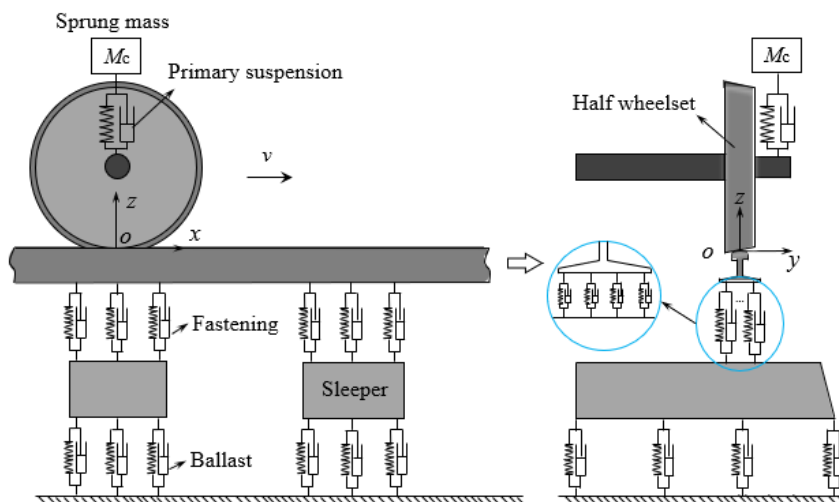
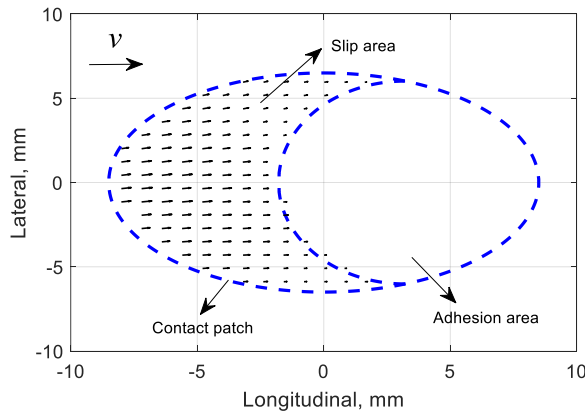


**Fig. 1.4.** Schematic diagram of the vehicle-track frictional rolling contact model

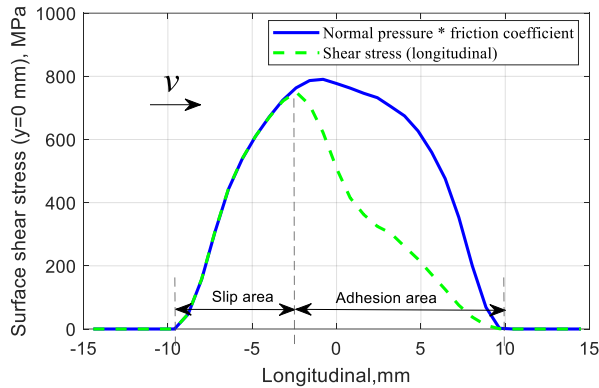
## 1.4.2 Modelling of wheel-rail contact mechanics

The vehicle is coupled with track structure through the wheel and rail contact. Therefore, contact mechanics is an essential component in modelling the vehicle-track dynamic interaction and investigating the damage mechanism. The influence of vehicle-track dynamics on rail failures will be reflected through the wheel-rail contact mechanics considering the damage mechanism.

Regarding the contact mechanics, the solutions can be divided into the normal solution and the tangential solution. The normal solution includes the characterization of contact patch size and shape (see Fig. 1.5a) and normal contact stress distribution. The tangential contact solution is a subject of frictional contact mechanics. It describes the distribution of surface shear stresses, adhesion-slip distribution and micro-slip (see Fig. 1.5). The micro-slip refers to the relative velocity between particles in contact from wheel and rail, respectively. Those parameters are determined by the applied normal load and traction power, the geometry of contact bodies at their contact patches, their material property, and the treatment of contact mechanics.



(a) Contact patch and vector of micro-slip within the slip area



(b) Distributions of surface shear stress and adhesion-slip areas.

**Fig. 1.5.** Schematic diagram of the adhesion-slip area and the micro slip in the contact patch ( $v$ : rolling speed)

The normal contact problems can be solved with Hertzian, multi-Hertzian, and non-Hertzian contact theories. Regarding the tangential contact solution, the frictional rolling contact problem was firstly solved by Carter in 1926 with a two dimensional (2D) model of the wheel as a cylinder rolling on the rail treated as an infinite half-space. In 1964, Vermeulen and Johnson extended Carter's 2D solution to 3D contact with elliptical contact patches. This theory is valid for contact problems with longitudinal and lateral creepages without spin. Kalker solved the 3D frictional rolling contact with arbitrary longitudinal and lateral creepages and spin, and proposed important theories in this field, e.g., the well-known

## 1 Introduction

---

exact solution implemented in the computer code CONTACT. Kalker's theory can be solved with the boundary element method (BEM) with the half-space assumption.

A powerful and accurate solution to frictional rolling contact problems is the finite element (FE) method. With the FE method, the contact geometry can be arbitrary, the contact state can be non-steady, and a more complex material model can be considered. The half-space assumption does not limit the method. Telliskivi and Olofsson [5] investigated with the FE method on normal contact problems of wheel tread and railhead contact, as well as wheel flange and rail gauge corner contact, with comparisons with Hertz analytical method and the program of CONTACT. The modelling and the numerical simulation are done with the software tool of ANSYS. Wiest *et al.* [6] employed a FE approach with the commercial software ABAQUS to assess the normal contact problems at the switch. Those applications are focused on normal contact problems.

Zhao and Li [7] developed a 3D FE model using an explicit time integration scheme, and both normal and tangential solutions are validated with CONTACT. The explicit integration approach renders the method available to study the high-frequency non-steady contact problems, for instance, the corrugation. The 3D FE vehicle-track structural dynamics are directly coupled with the wheel-rail contact mechanics. Continuum mechanics has been reported to play "an important role in structural analysis" [8]. Under their direct coupling, the instantaneous mutual influence of the contact mechanics and structural mechanics can be taken into consideration. This method has been extensively and successfully used to explain the root causes and development of rail squats [3, 9, 10], find the signature frequencies of different defects for their identification and detection with axle box acceleration (ABA) measurement [11], reproduce hammer test results [12], understand the dynamic vehicle-track interaction at crossings [13] and insulated rail joints [14], and thermo-mechanical coupling problems [15].

### 1.4.3 Numerical analysis of wear

Due to the light axle load, the contact stresses are not sufficient to bring plastic deformation. Thus wear, or frictional wear to make it more precisely, is usually treated as the damage mechanism of the corrugation, especially at the corrugation initiation stage when the dynamic contact load amplitudes are small. The wear develops within the slip area of the wheel-rail contact patch, where there is the relative velocity (See Fig. 1.5a). Based on the frictional power hypothesis, wear is proportional to the frictional power [16-20]. With the numerical approach, the frictional work at an element is calculated starting from the moment it is in contact until when it leaves the contact. This is specified in the equation

$$w(x, y) = kW_f(x, y) = k \sum_{i=1}^N \tau_i(x, y) v_i(x, y) \Delta t \quad (1.2)$$

where  $k$  is the wear coefficient,  $W_f(x, y)$  is the frictional work,  $\tau_i(x, y)$  and  $v_i(x, y)$  are the local tangential stress and slip, respectively, and  $N$  is the number of time steps  $\Delta t$  during which the element passes through the contact patch.

## 1.5 Metallurgical investigation on corrugated rail materials

The investigation on the corrugation problem with the numerical approach considers the damage mechanism as differential wear. This assumption is justifiable when investigating the corrugation initiation and growth without considering the attenuation process [21]. However, due to the presence of corrugation, especially when the corrugation is severe, the damage mechanism of rail material becomes complex. Besides, as the loading distributions vary along the corrugation, the microstructural features and the mechanical properties will differ at corrugation crests and troughs.

To this end, the metallurgical characterization of the corrugated rail material is undertaken to understand the material structural damages due to corrugation. The microstructure morphology of the specimens can be investigated with an optical microscope and scanning electron microscope. Moreover, the mechanical property is examined by micro-hardness tests.

The microstructural feature of the rail material at a corrugation crest is shown in Fig. 1.6. In the normal direction of the rail, three layers are identified, i.e., white etching layer, brown etching layer, and the parent material of pearlite matrix. The finding and understanding of the brown etching layer, its influence on cracks development, the characterization of microstructural features, and the mechanical property will give more insights into the rolling contact fatigue problems.



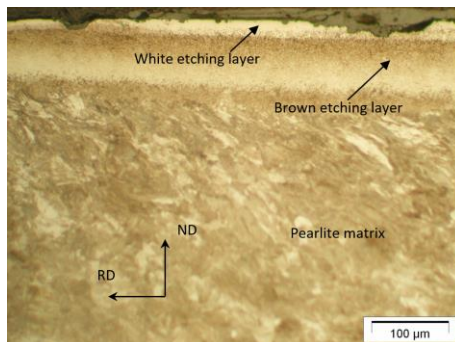


**Fig. 1.6.** Microstructural features of the BEL and WEL under optical microscopy, etched by 3 vol% Nital (RD: rolling direction; ND: rail normal direction)

### 1.6 Problem statement

The corrugation problem occurs on some types of track and at some locations (even with the same operation rolling stock). This indicates that the problem should be related to the track parameters. Most of the previous research explains the corrugation wavelength-fixing mechanism from the aspect to compare the frequency of structural dynamics and the corrugation frequency calculated by the train speed divided by the corrugation wavelength, and when there is a good match between both, the structural dynamics of the frequency is attributed to the cause of the corrugation. The whole process of the corrugation from initiation and the growing stage is not thoroughly investigated and revealed. To this end, the current research will concentrate on the following problems:

**Q1:** With a similar research methodology but different modelling approaches, could the corrugation grow?

**Q2:** When considering the variations of track parameters, could the corrugation initiate and consistently grow? Moreover, what is the physical explanation for the corrugation formation mechanism?

**Q3:** How is the influence of the corrugation on rail material damages?

## 1.7 Outline of the dissertation

The dissertation attempts to answer the above four research questions. Numerical simulations, experimental tests and metallurgical characterizations are employed. The main structure of the dissertation is shown in Fig. 1.8.

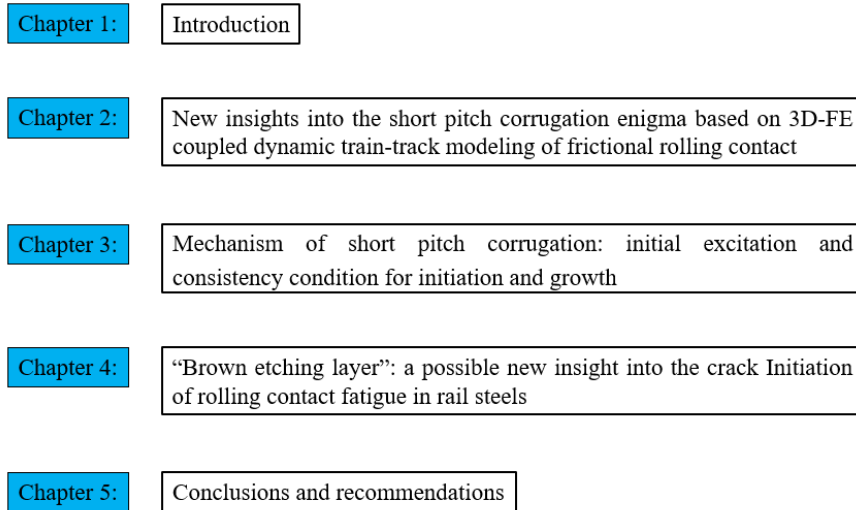


**Fig. 1.8.** Outline of the dissertation

In Chapter 1, a literature review is done to gain insights into the current research on corrugation.

In Chapter 2, a 3D transient FE train-track frictional rolling contact model is employed to study whether the corrugation can grow with a similar parametric variation study as in [19].

Motivated from the conclusions and insight in Chapter 2, Chapter 3 extensively studies: 1) whether the corrugation initiation can be reproduced with a variation of railpad modelling, 2) whether the reproduced corrugation can consistently grow, and 3) what is the explanation to the corrugation development mechanism.

Other forms of damage mechanisms could also develop in the corrugated rail material in a severe corrugation condition. Hence, Chapter 4 metallurgically investigates the changes in the material microstructures of the corrugated rail. Besides the well-known white etching layer (WEL), another hard and brittle layer with the name of the brown etching layer (BEL) is also observed. The BEL can cause fatigue cracks growing transversely and deeper, which

## 1 Introduction

---

is more detrimental to the rail service life. The wear resistance, the fatigue cracks of those layers all influence the damage mechanism of the corrugation. They should be considered when the corrugation severity is above certain stages.

Finally, some conclusions are obtained, and recommendations for future research are proposed in Chapter 5.

## References

- [1] Grassie SL. Rail corrugation: characteristics, causes, and treatments. *P I Mech Eng F-J Rai* 223 (2009) 581–596.
- [2] Kalousek J, Johnson KL. An investigation of short pitch wheel and rail corrugations on the Vancouver mass transit system. *P I Mech Eng F-J Rai* 206 (1992) 127–135.
- [3] Li Z, Zhao X, Esveld C, Dollevoet R, Molodova M, An investigation into the causes of squats—correlation analysis and numerical modelling. *Wear* 265 (2008) 1349–1355.
- [4] Knothe KL, Grassie SL, Modelling of railway track and vehicle/track interaction at high frequencies. *Vehicle Syst Dyn* 22 (1993) 209–262.
- [5] Telliskivi T, Olofsson U. Contact mechanics analysis of measured wheel-rail profiles using the finite element method. *P I Mech Eng F-J Rai* 215 (2001) 65–72.
- [6] Wiest M, Kassa E, Daves W, Nielsen J, Ossberger H. Assessment of methods for calculating contact pressure in wheel-rail/switch contact. *Wear* 265 (2008) 1439–1445.
- [7] Zhao X, Li Z. The solution of frictional wheel-rail rolling contact with a 3D transient finite element model: Validation and error analysis. *Wear* 271 (2011) 444–452.
- [8] Nishiura D, Sakaguchi H and Aikawa A, Development of Viscoelastic Multi-Body Simulation and Impact Response Analysis of a Ballasted Railway Track under Cyclic Loading. *Materials* 10 (2017) 615; doi:10.3390/ma10060615.
- [9] Li Z, Dollevoet R, Molodova M, Zhao X, Squat growth — some observations and the validation of numerical predictions. *Wear* 271 (1–2) (2011) 148–157.
- [10] Deng X, Li Z, Qian Z, Zhai W, Xiao Q, Dollevoet R. Pre-cracking development of weld-induced squat due To plastic deformation: Five-year field monitoring and numerical analysis. *Int J Fatigue* 127 (2019) 431–444.
- [11] Molodova M, Li Z, Núñez A, Dollevoet R, Validation of a finite element model for axle box acceleration at squats in the high frequency range. *Comput Struct* 141 (2014) 84–93.
- [12] Oregui M, Li Z, Dollevoet R, An investigation into the vertical dynamics of tracks with monoblock sleepers with a 3D finite-element model. *P I Mech Eng F-J Rai* 230(3) 891–908.
- [13] Wei Z, Shen C, Li Z, Dollevoet R. Wheel–rail impact at crossings: relating dynamic frictional contact to degradation. *J Comput Nonlinear Dyn* 12 (2017) 041016.

- [14] Yang Z, Boogaard A, Wei Z, Liu J, Dollevoet R, Li Z. Numerical study of wheel-rail impact contact solutions at an insulated rail joint. *Int J Mech Sci* 138–139 (2018) 310–322.
- [15] Naeimi M, Li S, Li Z, Wu J, Petrov RH, Sietsma J, Dollevoet R. Thermo-mechanical analysis of the wheel-rail contact using a coupled modelling procedure. *Tribol Int* 117 (2018) 250–260.
- [16] Hempelmann K, Hiss F, Knothe K and Ripke B. The formation of wear patterns on rail tread. *Wear* 144 (1991) 179–195.
- [17] Nielsen JCO. Numerical prediction of rail roughness growth on tangent railway tracks. *J Sound Vib* 267 (2003) 537–548.
- [18] Jin X, Wen Z, Wang K, Zhang W. Effect of a scratch on curved rail on initiation and evolution of rail corrugation. *Tribol Int* 37 (2004) 385–394.
- [19] Xie G, Iwnicki SD. Calculation of wear on a corrugated rail using a three-dimensional contact model. *Wear* 265 (2008) 1238–1248.
- [20] Meehan PA, Batten RD, Bellette PA. The effect of non-uniform train speed distribution on rail corrugation growth in curves/corners. *Wear* 366-367 (2016) 27–37.
- [21] Böhmer A, Klimpel T. Plastic deformation of corrugated rails—a numerical approach using material data of rail steel. *Wear* 253 (2002) 150–161.



## **NEW INSIGHTS INTO THE SHORT PITCH CORRUGATION ENIGMA BASED ON 3D-FE COUPLED DYNAMIC VEHICLE-TRACK MODELLING OF FRICTIONAL ROLLING CONTACT**

*A three-dimensional (3D) finite element (FE) dynamic frictional rolling contact model is presented for the study of short pitch corrugation that considers direct and instantaneous coupling between the contact mechanics and the structural dynamics in a vehicle-track system. The contribution of this paper is a global perspective of the consistency conditions that govern the evolution of short pitch corrugation. Wear is assumed to be the damage mechanism, and short pitch corrugation is modeled using wavelengths from field observations of a Dutch railway. The main insights are as follows: (1) the longitudinal vibration modes are dominant for short pitch corrugation initiation; (2) during short pitch corrugation evolution, the interaction and consistency between longitudinal and vertical modes determines the development of short pitch corrugation, and once a certain severity is reached, vertical modes become dominant; and (3) the main frequencies of the vertical contact force, longitudinal contact force, vertical vibration modes, longitudinal vibration modes and the resulting wear often differ from each other, which is inconsistent with the usual assumption that the frequency of the vertical contact force is the same as that of the short pitch corrugation passing frequency (corresponding to the wavelength of the differential wear).*

---

This chapter is based on the publication below:

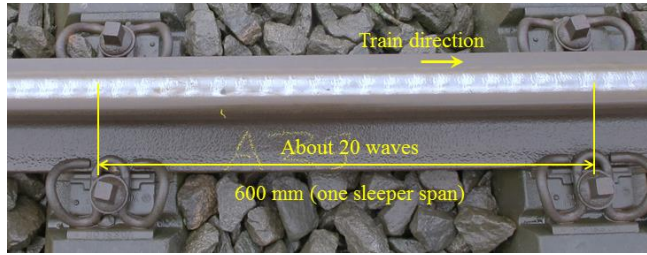
Li S, Li Z, Núñez A, Dollevoet R. New insights into the short pitch corrugation enigma based on 3D-FE coupled dynamic vehicle-track modeling of frictional rolling contact. *Applied Science* 7 (2017) 807.

### 2.1 Introduction

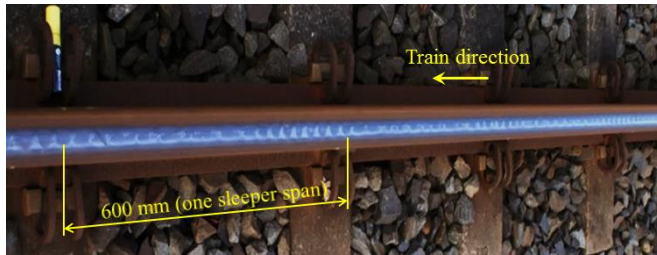
Rail corrugations are periodic defects commonly observed in all types of railway tracks. According to the current understanding of their development mechanisms, namely, the damage mechanisms and wavelength-fixing mechanisms [1], rail corrugations can be classified into six groups: heavy haul, light rail, booted sleepers, contact fatigue, rutting and short pitch corrugation. Among these groups, the development mechanisms of short pitch corrugation (subsequently called corrugation for short) are not fully understood. Although corrugation was identified more than a century ago and despite extensive research efforts [1, 2], an effective solution has not been developed to avoid the corrugation problem, which remains an enigma that has puzzled many researchers and engineers [3, 4]. Grinding appears to be the only effective corrective countermeasure; however, it increases maintenance costs and reduces the availability of the railway network. Thus, the development mechanisms of this phenomenon must be elucidated and an effective solution for its control at an early stage must be identified.

Corrugation mainly occurs on straight tracks or gentle curves where contact does not occur between the wheel flange and rail gauge corner (see Fig. 2.1), and it usually manifests as shiny ripples and dark valleys. The typical wavelength is in the range of 20 mm to 80 mm, with amplitudes up to 100  $\mu\text{m}$  [1]. Corrugation is one of the most prominent problems for railway infra managers because it increases the vibrations of the vehicle-track system and results in higher frequencies (more than 500 Hz) of the wheel-rail dynamic contact forces, which leads to accelerated degradation of vehicle-track system components and shortened service life [5]. In addition, the noise generated by vibrations is a nuisance to residents living near railway lines [1, 6]. Because of the high level of noise, corrugation is also known as “roaring rail”. Corrugation can also generate rolling contact fatigue (RCF), such as squats [7] (see Fig. 2.1c).

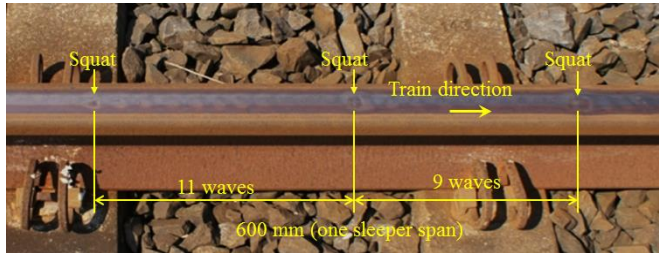
The main damage mechanism of corrugation is commonly considered to be wear caused by longitudinal wheel slip [8, 9]. Plastic deformation is another possible damage mechanism [1], and it has been investigated by a numerical approach [10] and metallurgical analyses [11]. The wear and deformation underlying corrugation are differential, i.e., they are selective processes that “consistently” occur more at certain locations than at adjacent locations, which results in the accumulation and growth of typical wave patterns [12]. In this case, “consistently” indicates that the wear and deformation caused by one-wheel passage repeats the same wavelengths and phase angle of previous wheel passages, which results in the accumulation of wear and deformations and the initiation of corrugation growth. Because damage originates in the contact patch, the contact mechanics within the



(a) Uniform corrugation with a wavelength of approximately 30 mm. Squats have not yet developed, and a ballasted track with mono-block sleepers and fastenings with a W-shaped tension clamp is shown. Photo taken near Assen, the Netherlands.



(b) Non-uniform corrugation of a constant periodicity of a sleeper span. The corrugation wavelength varies largely within a period. Squats have not yet developed, and a ballasted track with duo-block sleepers and fastenings with Deenik clips is shown. Photo taken near Steenwijk, the Netherlands.



(c) Non-uniform corrugation with a periodicity shorter than a sleeper span. The corrugation wavelength is approximately 30 mm. The squats were caused by corrugation, and a ballasted track with duo-block sleepers and fastenings with Deenik clips is shown. Photo taken near Steenwijk, the Netherlands.

**Fig. 2.1.** Short pitch corrugation and the resulting squats in the Dutch railway network. Wavelength and periodicity are distinguished (wavelength is the distance between two adjacent shining spots of ripples, and periodicity refers to the periodic pattern that contains multiple wavelengths of non-uniform amplitude of corrugation).



## 2 New insights into the short pitch corrugation enigma

---

contact patch must be examined to better understand the damage mechanisms. Because dynamic wheel-rail contact is difficult to measure, a numerical analysis that can accurately simulate the vehicle-track dynamic interaction must be developed to analyze corrugation under controlled conditions [13].

The Hertzian treatment of the contact problem has usually been used to solve normal contact problems [9], whereas Kalker's theories [14] are typically employed for the tangential direction [9]. The Hertzian solution considers that contact surfaces are frictionless smooth half-spaces. However, for worn or deformed profiles, such surface approximations may not hold in the vicinity of the contact patch [15, 16]. Nielsen [16] employed a two-dimensional (2D) non-Hertzian contact model and found that the shape of the normal stress distribution was not elliptic because of the geometrical asymmetry. Correspondingly, the tangential stress distribution varies along different positions of the corrugation and may be responsible for the development of corrugation. In addition, the Hertzian theory and Kalker's theory are based on statics. However, because the contact patch is on the order of 2 cm, which is similar to the corrugation wavelength, non-steady state processes caused by dynamic interactions must be considered [17, 18].

In addition to long-term damage mechanisms, a short-term dynamic process is believed to fix the wavelength through structural dynamics [1, 19]. The interaction between the short- and long-term mechanisms is represented by a feedback loop [1]. Three phenomena must be defined to understand corrugation development: 1) structural dynamics excitation caused by vehicle-track interactions, 2) loading response at the wheel-rail interface involving contact mechanics, and 3) feedback from the contact and damage to the structural dynamics as determined by the direct coupling between the contact mechanics and structural dynamics. In [9, 20], a crucial understanding of the contact phenomena in the corrugation problem is provided. The model used in [9, 20] solved the structural dynamics and contact mechanics problems separately in different models or steps. In addition to a reliable treatment of the contact mechanics and an accurate representation of the vehicle-track interaction, we propose a combined modelling approach that includes the coupling and interplay of both the structural dynamics and contact mechanics problems. This solution is inspired by the work of [9] and the question "why is roughness growth predicted by a simple contact model but not when complexity is increased to include non-Hertzian and non-steady contact conditions?"

The finite element method has been employed to investigate the development mechanism underlying squats in a vehicle-track system [7]. This modelling approach provides a good explanation for the development of corrugation initiated from isolated known railhead irregularities [21]. Because corrugation from isolated known railhead irregularities is of a

## 2 New insights into the short pitch corrugation enigma

---

short pitch type, this method could also be valid for investigating general types of short pitch corrugation. Corrugation that originates from railhead irregularities is caused by a dynamic force excited by known irregularities. In this case, the wavelength of the force is determined by the local track system, and the phase of the force is determined by the location of the irregularities. Thus, clear mechanisms of wavelength and phase fixing are involved. The wavelength and phase of the force at a given irregularity are always the same. Consequently, the resulting differential wear and/or plastic deformation is always in phase and damage accumulates under different wheel passages. In this way, corrugation can initiate and grow.

In the case of the general type of short pitch corrugation, a visually identifiable initiation source is not observed. Although the wavelength might be fixed by the track structure, e.g., the “pin-pin” resonance [22] or the stick-slip process [23], the randomness of passing wheels and the track can lead to phase variations of the contact force so that the total effect of many wheel passages may cancel out or suppress the differential wear and deformation.

Regarding the latter situation, we must identify the causes of the dynamic forces that result in differential wear and differential plastic deformation, which remain in phase for the multitude of different passing wheels such that the wear and deformation accumulate and corrugation can initiate and grow. Although the entire mechanism of the initiation and development of short pitch corrugation was not identified in this paper, we present new insights based on numerical modelling that are consistent with field observations and can contribute to a better understanding of this enigma. We expect that the new insights provided here will trigger many new research efforts in the field that will ultimately produce a more complete understanding of the enigma and a final solution.

In this paper, a 3D finite element (FE) approach is presented. This approach combines the vehicle-track interaction model of [7] with the solution for transient frictional rolling of [24]. The vehicle-track structural dynamics are directly coupled to the wheel-rail contact mechanics through the continuum treatment of the wheel and rail in the structure. The simulation of continuum mechanics has been reported to play “an important role in structural analysis” [25] and allows the instantaneous mutual influence of the contact mechanics and the structural mechanics to be simulated. This approach was presented in [26] to analyze the phase relationship between the given corrugation and the resulting periodic wear, and a similar approach was employed to study corrugation in a high-speed railway [27]. In this paper, the transient states of the rolling contact and wear are evaluated under a variety of loading conditions in relation to the dynamic forces excited by a passing wheel over a rail with and without corrugation. The damage mechanism is assumed to be limited to wear because the focus of this paper is on the conditions that may lead to the

## 2 New insights into the short pitch corrugation enigma

consistent initiation and growth of corrugation. To account for plasticity, the method of [28] can be readily incorporated, which will be our future research focus.

## 2.2 Model

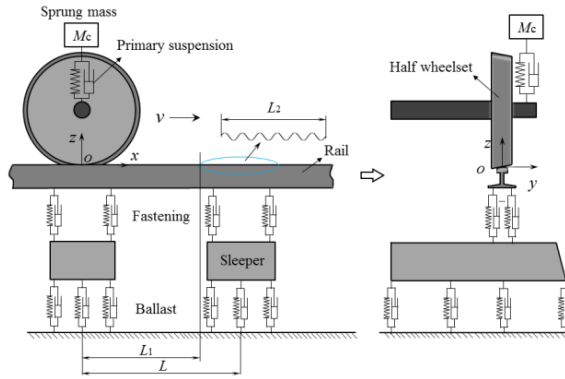
### 2.2.1 FE model

A schematic diagram of the 3D FE vehicle-track model is shown in Fig. 2.2. The model is based on a symmetrical vehicle-track system assuming a straight track in which lateral movement is negligible. The wheel, rail and sleepers are modelled with solid elements. The nominal radius of the wheel is 0.46 m, and the tread coning is 1/40. The rail is a standard UIC 54 profile with an inclination of 1/40. The contact surface of the wheel is smooth, whereas a length of corrugation is prescribed along the rail surface. The sprung mass (the weight of the car body and the bogie) is lumped into a mass element  $M_c$  supported by the primary suspension, which is represented by spring-damper elements. The sprung mass above a half wheelset is 1/8 of the sprung dynamic load of a whole vehicle, which is approximately a quarter of the sprung mass carried by a bogie. The fastening system and the ballast are also modelled as spring-damper elements. The track parameters are taken from [29] as shown in Table 2.1 and represent the typical Dutch railway system. In the FE model, the wheel and rail are meshed with 8-node solid elements. To achieve a solution of sufficient accuracy and an acceptable computation time, only the size of the elements in the solution zone is refined (0.8 mm  $\times$  0.8 mm in the longitudinal and lateral directions). The elements far from the solution zone are meshed at an element size up to 7.5 cm. These choices are based on [24], which concluded that the contact mechanics solution with an element size of 1.3 mm  $\times$  1.3 mm is sufficiently accurate when the FE approach used here is implemented for engineering applications. The total number of elements in the model is 1135384, the number of nodes is 1297900, and the model length is 18 m. In [30], a track length of 10 m was sufficient for problems of similar frequency and wavelength. The damage mechanism studied in this paper is wear; thus, the wheel and rail materials are assumed to be elastic. A Coulomb friction law is employed with a friction coefficient  $f_c$  of 0.6 as in [31]. In the literature, the friction coefficient of dry wheel-rail contact is reported to be between 0.4 and 0.65 [32].

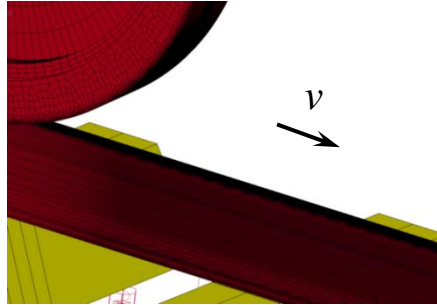
The solution process of the simulation includes two steps: an implicit analysis (using Ansys) and an explicit analysis (using Ls-dyna). The implicit analysis is performed to identify the initial deformation in the equilibrium position of the vehicle-track system. Then, the wheel is set to roll along the rail with a constant speed  $v = 38.9$  m/s (corresponding to the typical

## 2 New insights into the short pitch corrugation enigma

Dutch passenger train speed of 140 km/h). An explicit integration scheme with a central difference method is then implemented to solve the wheel-rail frictional rolling contact problems. The displacements obtained from the implicit process are used as the initial state of the explicit integration process. If the time step ( $4.67 \times 10^{-8}$  s in this model) is smaller than the critical time step ( $5 \times 10^{-8}$  s) determined by the Courant criterion [33], convergence is guaranteed. By keeping the time step sufficiently small, the model can include all necessary vibration modes. In the explicit analysis, the frictional rolling is modelled using a surface-to-surface algorithm with the penalty method described in [34]. Because of the nature of explicit integration, the effect of transient rolling and the high-frequency dynamic behavior of the vehicle-track system excited by the moving wheel are automatically included in the solution.



(a) Schematic diagram of the model



(b) FE model in 3D

**Fig. 2.2.** Vehicle-track frictional rolling model in 3D.

As shown in Fig. 2.2a, a distance  $L_1$  is used during the explicit process to diminish the effect of vibration excited by imperfect initial equilibrium because of numerical errors from the implicit solution. A total of 10 waves of corrugation with length  $L_2$  are introduced after  $L_1$ . The traction coefficient  $\mu$  is defined as follows

## 2 New insights into the short pitch corrugation enigma

$$\mu = F_L/F_N \leq f_c \quad (2.1)$$

where  $F_N$  is the normal contact force and  $F_L$  is the resultant tangential (creep) force in the longitudinal direction caused by an applied torque. Different traction coefficients produce different adhesion-slip states as well as damages. In the subsequent analysis, a traction load corresponding to 40% of the static normal contact force is applied via a torque about the axis of the wheel. This produces a  $\mu$  of 0.4, which is usually the maximal traction coefficient of rolling stock [35, 36]. Because of the dynamic nature of vehicle-track interactions, especially in the presence of corrugation, the actual contact forces are not constant. Therefore, the instantaneous traction coefficient varies with time and space along the track, and the actual value of the traction coefficient deviates from the static value. Regarding creepage, the approach of [7] and [24] is used in this paper, where a constant driving torque is specified. The resulting creepage fluctuates with the corrugation [27].

**Table 2.1.** Vehicle parameters and track parameters [29]

Parameters			Values		
Wheel load	Primary suspension	Stiffness	116.8 kN	Wheel and rail material	Young's modulus
		Damping	1.15 MN/m		Poisson's ratio
			2.5 kNs/m		Density
Rail pad		Stiffness	1,300 MN/m	Sleeper	Young's modulus
		Damping	45 kNs/m		Poisson's ratio
Ballast		Stiffness	45 MN/m		Mass density
		Damping	32 kNs/m		Spacing (L)
					0.6 m

A few additional remarks on the model are warranted. Note that high friction and traction coefficients are used. In [37, 38], high traction was reported to facilitate corrugation development. Additionally, regarding the traction coefficient, we assume that the damage mechanism is wear. Hence, a large value is chosen to ensure a high longitudinal contact force and thus obtain high wear. A large traction coefficient indicates a large slip zone. A large slip zone aids in the visualization of changes in the contact patch caused by corrugation; thus, it is easier to visualize and compare the contact solutions [24]. Finally, the model does not include brake disks or gears and will not represent torsional vibrations. Torsional wheelset vibrations have been considered as a cause of corrugation at curves [1, 39, 40]; however, recent research [41] has shown that torsional wheelset vibrations are not correlated with corrugation development at curves. Torsional vibration is also considered in [42] for corrugation related to vibration up to about 100 Hz. In this paper, the frequencies considered are in the order of 1000 Hz.

### 2.2.2 Corrugation model

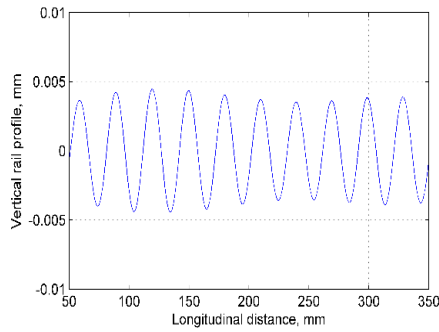
In this paper, corrugation with a sinusoidal profile is used as a test case. This choice is based on field observations, such as those shown in Fig. 2.1a. Moreover, our work is a continuation of previous research in which corrugation was assumed to have a sinusoidal profile [3, 9, 43-46]. A sinusoidal corrugation with a constant wavelength is applied to the rail surface expressed by the equation:

$$z(x) = A \cos\left(\frac{2\pi x}{\lambda} + \theta\right) - A \quad (2.2)$$

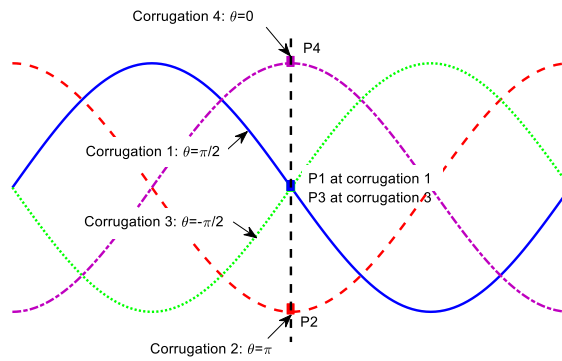
where  $A$  is the amplitude of the corrugation,  $\lambda$  is the wavelength, and  $\theta$  is the phase. The second term  $-A$  guarantees that the peak of the corrugation is not higher than the initial profile of the rail surface.

The wavelength is 30 mm, which is approximately equal to one of the recorded corrugation wavelengths on the Dutch railway network shown in Figs. 2.1a and 2.1c (see the measurement in Fig. 2.3a). For the analysis, 10 waves are considered; thus,  $L_2$  equals 300 mm. The corrugation considered is located above a sleeper support (as shown in Fig. 2.1b), which has been reported as a position where corrugation is more likely to develop [22]. To examine the wheel-rail contact during the growth process of the corrugation, the amplitudes of  $A = 0 \mu\text{m}$  for smooth rail and  $A = 2.5 \mu\text{m}$ ,  $5 \mu\text{m}$ ,  $10 \mu\text{m}$ , and  $20 \mu\text{m}$  for corrugated rail are modelled (the peak-to-trough distance is twice the amplitude). By maintaining  $\theta$  between  $-\pi/2$  and  $\pi$ , contact solutions can be studied at different locations within one complete corrugation wavelength, i.e., the falling edge (P1), the trough (P2), the rising edge (P3) and the peak (P4), as shown in Fig. 2.3b. Fig. 2.3c shows a magnified 3D configuration of the corrugation in the rail surface.

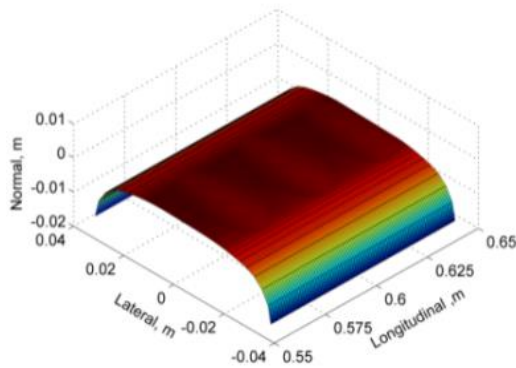
## 2 New insights into the short pitch corrugation enigma



(a)



(b)



(c)

**Fig. 2.3.** Modelled corrugation: (a) field measurement of corrugation (27-33 mm bandpass filtering); (b) schematic diagram of the corrugation and 4 positions; and (c) illustration of the applied corrugation (corrugation 2 with P2 at 0.6 m) in the rail surface with 5 $\times$  magnification (only 3 complete waves are plotted).

### 2.2.3 Validity of the model

To characterize the dynamics in the frequency range of interest as discussed in the introduction, corrugation modelling should consider the following issues: static and dynamic contact problems should be validated, structural dynamics should be considered, and coupling between the contact problem and structural dynamics should be validated.

- 1) With respect to the contact problems, a method similar to that of [24] is used herein. This method is suitable for resolving dynamic contact problems, and its validity has been demonstrated by the close reproduction of the evolution of squats [7, 49]. Moreover, this method has been verified as suitable for resolving static contact problems based on the established solutions of Hertz, Spence, Cataneo, Mindlin and Kalker [24, 48].
- 2) To validate the structural dynamics, a) the approach used in this paper can reproduce the hammer test [50]; thus, the model can simulate measured track receptance based on identified track parameters. b) Furthermore, the model can simulate axle-box acceleration (ABA) measurements [30]. Consequently, the model can capture the dynamics of wheels and tracks and the interaction between the vehicle and the track in the relevant frequency range.
- 3) With respect to assessing the validity of the model for a vehicle-track system with direct coupling between the contact problem and structural dynamics, the model exhibits a good representation of the dynamic response (spatial and frequency) of corrugation induced by squats. As noted in [21], “the model provides a good explanation for the development of corrugation initiated from isolated railhead irregularities”. Thus, in this paper, the challenge is to extend the model to the study of the more general type of corrugation that does not present clear local irregularities as the source of corrugation initiation.

As will be discussed in greater detail in Section 4.2 on the prediction of major field observations, the simulated wear in Fig. 2.8a is in agreement with the field observations shown in Fig. 2.1b and Fig. 2.1c. Here, the irregular distribution of wear along one sleeper span is clear, and the observation and simulation are in agreement. In the paper, other agreements between the model results and field observations are discussed in greater detail later in the text. For example, the contact solutions that indicate that wear is the more probable damage mechanism at the corrugation trough [1, 11, and 67] will be described in Section 3 and the occurrence of squats in agreement with the observation in Fig. 2.1c will



## 2 New insights into the short pitch corrugation enigma

be explained in Section 4.2. These summaries comprehensively describe and analyze how the model in this paper was validated.

For other the track and vehicle field data, typical parameters of the Dutch railway are used [29]. For modelling corrugation, a sinusoidal profile is employed based on field measurements (Fig. 2.3a) and observations (Fig. 2.1a).

## 2.3 Contact solutions at corrugation

### 2.3.1 Normal contact

The FE approach defines whether a node is within the contact patch through the node force. A node is in contact if

$$|F_{n_N}| > 0 \quad (2.2)$$

where  $F_{n_N}$  is the nodal force in the direction normal to the local surface. Because of the presence of corrugation, the stress and slip distributions will vary along a corrugation wavelength. Those differential distributions of the normal pressure, shear stress and slip are the direct factors in corrugation development.

Fig. 2.4a shows the changes in the contact patch size at P1, P2, P3 and P4 with increasing amplitude  $A$ . Compared with  $A = 0 \mu\text{m}$ , an increase in size of up to 16% at P2 is observed in the case of  $A = 20 \mu\text{m}$ , and the increase is approximately 4% at P3. At the other two positions, the changes are minor. The maximum contact patch size is approximately  $200 \text{ mm}^2$  ( $A = 20 \mu\text{m}$ ) at P2, i.e., the corrugation trough, whereas it is approximately  $170 \text{ mm}^2$  when the rail is smooth. Fig. 2.4b displays the maximum contact pressure along the longitudinal axis ( $y = 0 \text{ mm}$ ) for different corrugation amplitudes  $A$ . As the corrugation amplitude increases from  $0 \mu\text{m}$  to  $20 \mu\text{m}$ , the contact pressure at P2 drops significantly to 56% of the original level, i.e., from  $1320 \text{ MPa}$  to  $745 \text{ MPa}$ . This decrease is partly because of the 15% increase in the contact patch size (see Fig. 2.4a). At P1 and P3, the maximum pressure declines slightly to 78% of the original level. An increase in pressure of 6% is observed at P4 for the case of  $A = 20 \mu\text{m}$ .

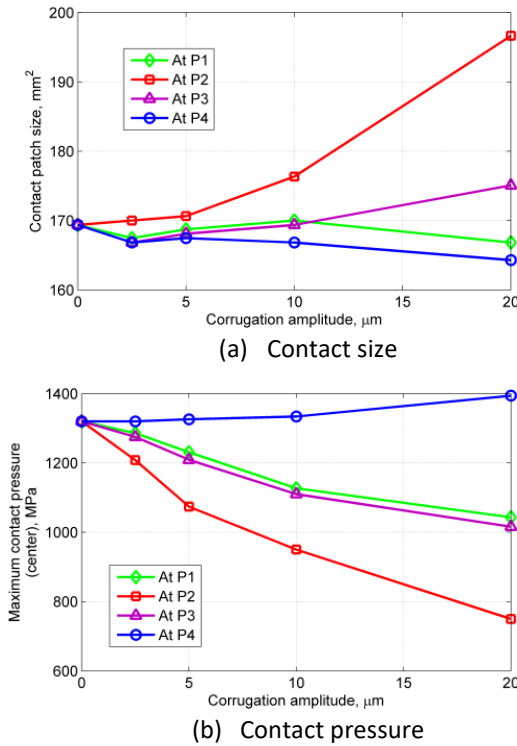
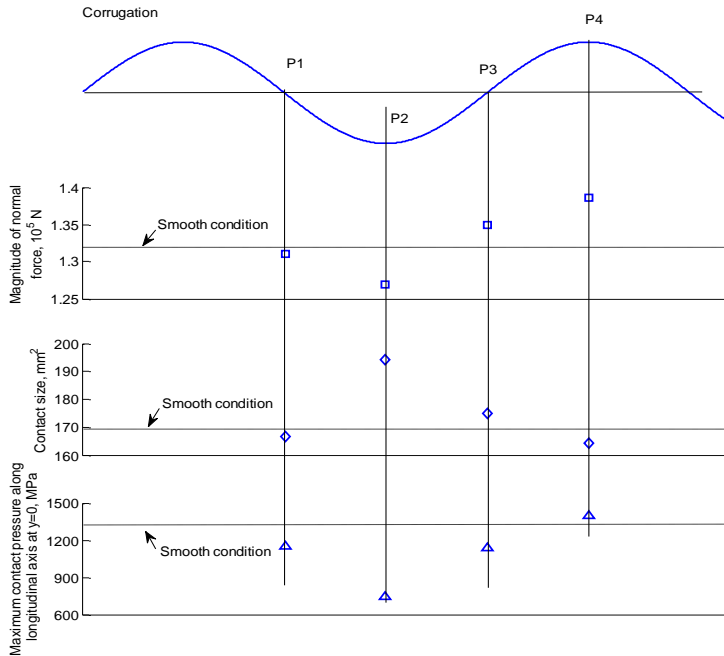


**Fig. 2.4.** Influence of corrugation amplitude on the size of the contact patch and the maximum contact pressure along the longitudinal axis  $y = 0$  mm.

Fig. 2.5 shows a typical profile of the variation of the magnitude of normal force, contact size and maximum contact pressure along the longitudinal axis. In the figure, the typical normal force is the lowest at trough P2 and the highest at peak P4, with intermediate values at points P1 and P3.

As the corrugation amplitude increases, the normal contact force at P2 decreases and the area of the contact patch increases; thus, the pressure decreases. At P4, the normal contact force increases, and the area of the contact patch decreases; thus, the pressure increases. At P1 and P3, the normal contact force and the area of the contact patch are intermediate between cases P2 and P4. These patterns are further evident in Fig. 2.4b, where the maximum contact pressure of P1 and P3 for the different corrugation amplitudes decreases, although it does not decrease as strongly as in the case of P2.

## 2 New insights into the short pitch corrugation enigma



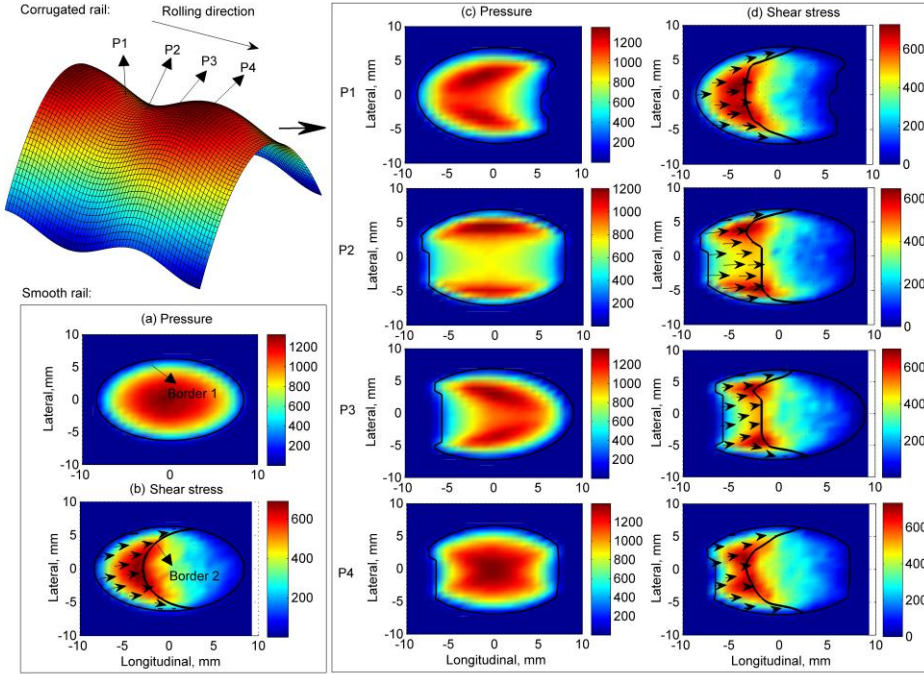
**Fig. 2.5.** Magnitude of the normal force, contact size, and maximum pressure along the longitudinal axis at ( $y = 0$  mm) at the four analyzed positions P1, P2, P3 and P4 ( $A = 20 \mu\text{m}$ ).

Fig. 2.6 shows the projections of contact pressure and shear stress onto the  $xOy$  plane, the shape of the contact patch under the smooth condition, and the evolution within one corrugation wavelength from P1 to P4 when  $A = 20 \mu\text{m}$ . Most shapes are not elliptic and thus differ from the Hertzian solution. Because of the downhill slope of the corrugation at P1, a large drop in pressure is observed at the leading edge of the contact patch and vice versa at P3. Thus, the pressure distributions at P1 and P3 take the shapes of a “waning crescent moon” and “waxing crescent moon”, respectively. At P2, the maximal pressure shifts to the field and gauge sides, thereby decreasing the contact pressure in the contact patch center to 600–800 MPa. The pressure distribution at P4 is close to the solution under the smooth rail except for a slight shrink of the contact patch at the leading and trailing edge centers. The maximum pressure is slightly higher than that at the other locations as shown in the pressure scaling color bar.

As shown in Fig. 2.5, the pressure variation within a corrugation wavelength along the longitudinal axis  $y = 0$  mm is approximately in phase with the corrugation. Furthermore, the shapes of the contact patch differ from that under the smooth rail condition. Part of the contact patch is not present in the leading area at P1, in the trailing area at P3 and in both

## 2 New insights into the short pitch corrugation enigma

the leading and trailing areas at P2 and P4. Thus, the deviation from a Hertzian solution is large and further exacerbated by increases in the corrugation amplitude.



**Fig. 2.6.** Contact pressure, shear stress, contact patch, adhesion-slip distributions and vector graphs of micro-slips (vectors in Figs. 2.6b and 2.6d) when  $A = 20 \mu\text{m}$  along one corrugation wavelength (P1~P4) (projection onto the  $xOy$  plane; Border 1: contact patch border; Border 2: adhesion-slip distribution border).

### 2.3.2 Tangential contact

Figs. 2.6b and 2.6d show the surface shear stress distributions when the rail is smooth and corrugated, respectively. In the presence of corrugation, especially when the amplitude is large, e.g.,  $A = 20 \mu\text{m}$ , the distributions of the shear stress differ from those of the smooth rail case. Similar to the pressure distributions, the maximum shear stress, which occurs in the central part and at the adhesion-slip boundary within the contact patch, is cut in the middle and protrudes on the gauge and field sides, especially at P2 and P3. The development of the surface shear stress with the increase in corrugation amplitude follows a trend similar to that of the normal pressure in the slip zone of the contact patch, where the surface shear stress equals the product of the normal pressure and the frictional coefficient.

## 2 New insights into the short pitch corrugation enigma

When a tangential force is applied, slip arises in the contact area. In the adhesion zone, there should not be relative slip between the contacting particles of the wheel and rail where the wheel and rail surfaces stick together. There should, however, be relative slip between the contacting particles of the wheel and rail surfaces in the slip zone. The tangential contact force  $F_{n,T}$  at a node in the slip zone equals the bound of the tangential nodal force, which is the product of the nodal force  $F_{n,N}$  in the normal direction and the friction coefficient  $f_c$  according to Coulomb's law. In the adhesion zone, the tangential nodal contact force is lower than the bound. Therefore, a node is in a slip zone if

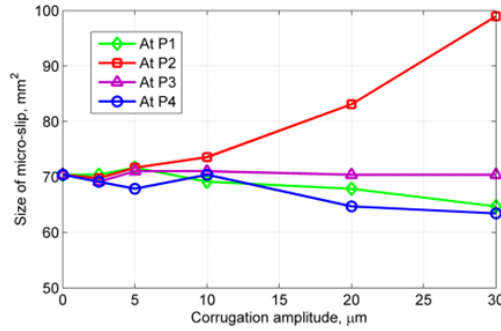
$$f_c |F_{n,N}| - |F_{n,T}| < \varepsilon_T \quad (2.3)$$

where  $\varepsilon_T$  is the tolerance. In this paper,  $\varepsilon_T$  is 5% of the maximal tangential nodal force in the contact patch.

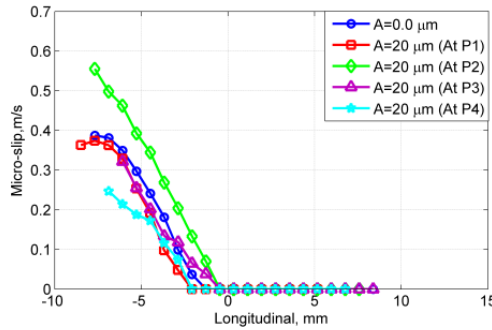
The adhesion-slip distribution in the presence of corrugation is shown in Fig. 2.6d. The boundary between the adhesion and the slip zones at P2 and P3 is far from elliptic [14]. As assumed, differential wear proportional to the frictional work [9, 18, 22] causes the development of corrugation. Frictional work only occurs in the slip zone. Therefore, the size of the slip zone in the contact patch as well as the magnitude of the slip might be indicators of corrugation development.

In Fig. 2.7a, changes in the size of the slip zone with increases in corrugation amplitude at P1, P2, P3 and P4 are shown. The size fluctuates slightly at  $A = 0 \sim 10 \mu\text{m}$ . To study the trend of change, the corrugation amplitude is further extended to  $30 \mu\text{m}$ . When the rail is smooth, the size of the slip zone is approximately  $69 \text{ mm}^2$ , which is 40% of the whole contact patch ( $170 \text{ mm}^2$ ). After the initial fluctuations at  $A = 2.5 \mu\text{m}$  and  $5 \mu\text{m}$ , the value at P2 presents the largest change and increases up to  $98 \text{ mm}^2$  at  $A = 30 \mu\text{m}$ , which is 57% of the total smooth contact zone. At the other three positions, the change in the slip zone size is small. Specifically, at P3, this value remains almost at the same level, whereas at P1 and P4, a 10% decrease is observed compared with that of the smooth rail ( $A = 30 \mu\text{m}$ ).

Fig. 2.7b shows the change in the slip distribution along the longitudinal axis  $y = 0 \text{ mm}$ . The maximum slip at P2 is much larger than that of the other cases, which is in agreement with the trend shown in Fig. 2.7a. At P3 and P4, the magnitudes of the slip decrease compared with that of the smooth rail. The increase in the size of the slip zone and the maximum magnitude of the slip at P2 may indicate that large micro-slips in the trough could be a major driver of corrugation development. The distribution of the slip within the contact patch is shown in Figs. 2.6b and 2.6d.



(a) Size of slip zone



(b) Slip along the longitudinal axis y = 0 mm

**Fig. 2.7.** Size of the slip zone as a function of the corrugation amplitude and slip distribution along the longitudinal axis y = 0 mm at the 4 positions.

## 2.4 Wear and corrugation simulation

### 2.4.1 Wear model

The contact solutions in the presence of corrugation (as previously discussed) are used to calculate the frictional work, which is considered proportional to wear [9, 18, and 22]. This section examines whether corrugation will grow under the given conditions by comparing the phases of wear and corrugation. To consider a whole sleeper, the applied corrugation of length  $L_2$  in Fig. 2.2a is extended along the rail to start at  $x = 0.87$  m to cover both the middle sleeper span and sleeper support. The frictional work is calculated in the contact patch for each element for a whole wheel passage, i.e., from element entry until leaving contact. The wear of an element is as follows:

## 2 New insights into the short pitch corrugation enigma

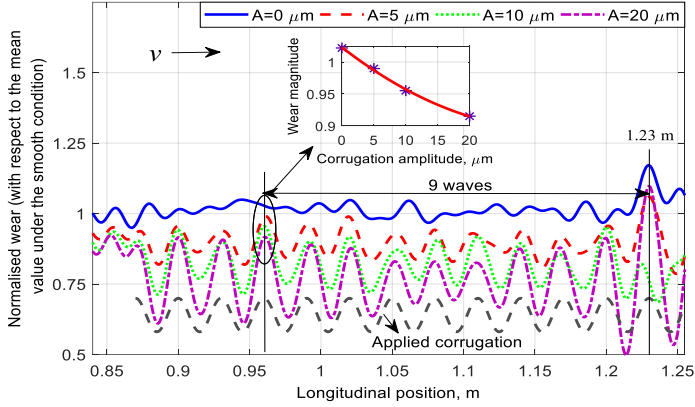
$$w(x, y) = kW_f(x, y) = k \sum_{i=1}^N \tau_i(x, y) v_i(x, y) \Delta t \quad (2.4)$$

where  $k$  is the wear coefficient,  $W_f(x, y)$  is the frictional work,  $\tau_i(x, y)$  and  $v_i(x, y)$  are the local tangential stress and slip, respectively, and  $N$  is the number of time steps  $\Delta t$  during which the element passes through the contact patch. The wear coefficient  $k$  is a constant that depends on the material, lubrication, and temperature among other factors [8, 9, 51–53]. In this work, the calculated wear is normalized with respect to the average value of the wear under the smooth rail condition. This normalization is performed because the phase angle between wear and corrugation determines whether the corrugation will grow, which represents our main concern in this paper and is not directly affected by the wear coefficients. Further research will include measurements of the wear coefficients to guide maintenance.

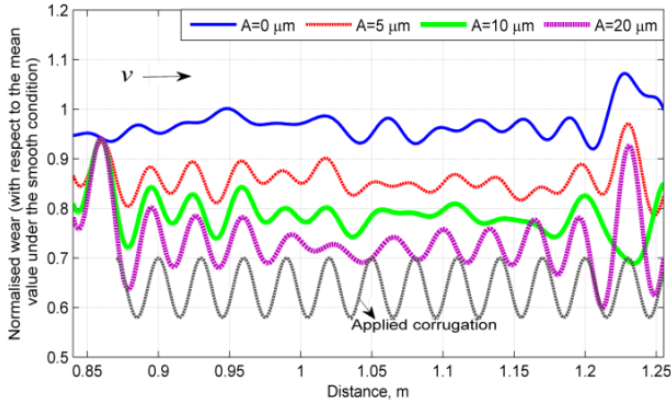
### 2.4.2 Prediction of major field observations

As in reality, the rolling of the wheel along the rail excites a range of vibrations of the structure and continua in the system. However, only a few of the vibration components are directly related to the corrugation. The corrugation wavelength observed in the field and introduced in the model is 30 mm and the wavelength of short pitch corrugation is typically 20–80 mm, and the calculated wear is high-pass filtered to remove wear patterns shorter than 20 mm.

The wear along the longitudinal axis  $y = 0$  mm is studied. Fig. 2.8a shows the distribution of the simulated wear along the rail with different corrugation amplitudes for the P4 corrugation position of  $\theta = 0$ , with 1.2 m as the corrugation peak. The results for the other corrugation positions show similar trends and are not presented. The wear is not uniform along the rail; thus, corrugation development will not be uniform under the evaluated conditions. Comparing the field observations in Fig. 2.1 with the wear simulation results in Fig. 2.8a reveals that the model closely reproduces the conditions in Fig. 2.1b and Fig. 2.1c in terms of predicting the periodicity of the wear and the number of corrugation waves in a periodicity. The periodicity in Fig. 2.1c is 9 and 11 waves. The periodicity in Fig. 2.8a is 9 waves between the largest peak-to-trough wear magnitudes at 0.96 m and 1.23 m. In Fig. 2.1c, the periodicity is counted between the squats because the squats should have been caused by the most severe corrugation, i.e., the largest wear.



(a) High-pass filtered at  $\lambda = 20$  mm



(b) High-pass filtered at  $\lambda = 30$  mm

**Fig. 2.8.** Distribution of wear at different corrugation amplitudes obtained for the corrugation in Fig. 2.3b with  $\theta = 0$  and P4 at 1.2 m. The middle of a sleeper is at 1.2 m, and the midpoint between two sleepers is at 0.9 m.

Furthermore, the results agree well with the field observations (Fig. 2.1). Specifically, the model predicts that the largest wear occurs at 1.23 m above a sleeper centered at 1.2 m (see Fig. 2.8a). This is in agreement with Fig. 2.1c, in which one of the squats was above a sleeper, and with those in Fig. 2.1b, where the corrugation was always the most severe above the sleepers. Rails above sleepers have been reported to be more prone to corrugation [22]. The inset in Fig. 2.8a shows that the magnitude of wear decreases as the corrugation amplitude increases. This pattern can be understood in relation to Figs. 2.6 and 2.7b because the wear is proportional to the product of the shear stress and the slip. The slip at  $A = 20 \mu\text{m}$  in Fig. 2.7b is generally equal to or less than that at  $A = 0 \mu\text{m}$  except at P2.



## 2 New insights into the short pitch corrugation enigma

The shear stress at  $A = 20 \mu\text{m}$  in Fig. 2.6 is always less than that at  $A = 0 \mu\text{m}$ , and the difference is large for P2 and P3.

The wear in Fig. 2.8a is of the same wavelength and phase as the modelled corrugation. Thus, the existing corrugation will be erased by wear and will not grow, and if the rail is smooth, no corrugation will initiate. This finding is reasonable because the simulation is based on nominal track parameters; in reality, many tracks are indeed free of corrugation. Thus, the results indicate that corrugation is sensitive to the system parameters, e.g., rail fastening [41].

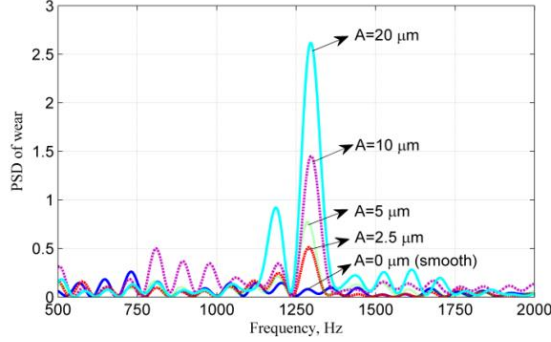
### 2.4.3 Analysis of longitudinal and vertical rail modes

Fig. 2.9 shows the power spectra of the calculated wear under different corrugation amplitudes. A major frequency component is observed at approximately 1296 Hz when  $A = 20 \mu\text{m}$ . This component corresponds to the frequency of 1297 Hz excited by a wheel passing at 38.9 m/s over the corrugation with a wavelength of 30 mm. When  $A$  is reduced, this major frequency also decreases. At  $A = 2.5 \mu\text{m}$ , the frequency is 1290 Hz, which is 7 Hz lower. Thus, the frequency of the wear is initially (i.e., when  $A$  is small) lower than that of the modelled corrugation, and it is influenced by the corrugation. Thus, the initial frequency of the wear should have been determined by the natural modes of the system, and when the corrugation amplitude is large it becomes a strong excitation that dominates the vibration. Therefore, the wavelength of the wear changes with increases in corrugation amplitude if the natural frequency and the corrugation passing frequency are different.

When  $A$  is increased to  $20 \mu\text{m}$ , there is a sudden PSD increase at 1185 Hz, see the second major peak in Fig. 2.9. Modal analysis in Fig. 2.10a and 2.10b shows that these two major frequencies of 1185 and 1296 Hz correspond to two natural frequencies of the system (1185 Hz of a vertical rail mode and 1291 Hz of a longitudinal rail mode), i.e. the two natural frequencies that are closest to and/or lower than the corrugation passing frequency of 1297 Hz (see in Fig. 2.10 the characteristic modal shapes). The closest pin-pin resonance is at approximately 1110 Hz (see Fig. 2.10c), and it thus does not seem to have influence on the wear development in this case. Based on Fig. 2.9, it is reasonable to assume that the initiation of the observed corrugation with a wavelength of 30 mm is mainly related to these two modes. When the corrugation amplitude is close to 0, e.g.,  $A = 2.5 \mu\text{m}$  or less, the major frequency of the wear is approximately 1290 Hz, which is 6 Hz lower than the 1296 Hz of the wear at  $A = 20 \mu\text{m}$ , 1 Hz lower than the longitudinal modes, but 105 Hz higher than the vertical mode. In this case, the track parameters are a stronger determinant of the corresponding wavelength of the calculated wear than is the modelled corrugation because the track parameters determine the longitudinal and vertical modes, which in turn suggests

## 2 New insights into the short pitch corrugation enigma

that for the initiation of corrugation, the longitudinal mode, which is very close to the frequency of the observed corrugation, should have played a major role compared with the vertical mode.



**Fig. 2.9.** Power spectral density (PSD) of wear  $\lambda = 30$  mm, with a major peak at 1296 Hz and a secondary peak at 1185 Hz, when  $A = 20$   $\mu\text{m}$ .

With the growth of corrugation, the vertical mode plays an increasingly important role in corrugation development because corrugation mainly excites vertical modes. This behavior is confirmed by Fig. 2.9: when  $A$  is larger than 10  $\mu\text{m}$ , the PSD peak of the secondary frequency at 1185 Hz begins to make a significant contribution to the wear. This frequency corresponds to the vertical mode and is excited when the corrugation amplitude is sufficiently large. When the corrugation amplitude is further increased, it will incur wear that is of the same frequency as the corrugation. This pattern is observed in the major frequency in Fig. 2.9: when  $A$  is increased from 2.5 to 20  $\mu\text{m}$ , the frequency of the major wear component increases from 1290 to 1296 Hz, thus approaching the passing frequency of 1297 Hz of the prescribed corrugation. Therefore, for the initiation of corrugation, the longitudinal modes are more important, whereas when the corrugation amplitude is significant, the vertical modes will be dominant. For intermediate situations, the longitudinal and vertical modes together determine whether corrugation will grow or be suppressed by wear based on whether the wear is of the same frequency and correct phase. Thus, both longitudinal and vertical modes are decisive for the initiation and growth of corrugation. This finding represents a novel contribution to the literature, which has thus far only considered the effects of the vertical, lateral and torsional modes [1, 3, 39, 40, 55, 56]. In [42] the relative longitudinal vibration of the two rails of a track is considered for corrugation initiation, for which each half track is modelled as an inertia and longitudinal vibration modes of rail as flexible body are not considered.

### 2.4.4 Additional comments

Minor frequency components may also be relevant. According to the previous analysis, the wavelength of the wear changes with the corrugation amplitude  $A$ ; however, Fig. 2.8a shows a constant wear wavelength because Fig. 2.8a was high-pass filtered at  $\lambda = 20$  mm. When the same signals are high-pass filtered at  $\lambda = 30$  mm, i.e., when the frequencies of 1185 Hz and 1291 Hz are given a more dominant role, the wavelength also varies (see Fig. 2.8b), and the phase of the wear changes with  $A$ . This behavior indicates that certain minor frequency components of wear shown in Fig. 2.9 also play a relevant role in determining the wavelength and phase of the wear and thus the development of corrugation.

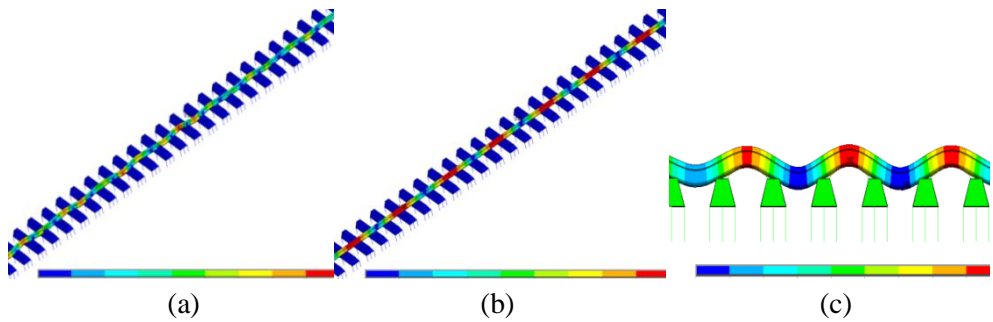


**Fig. 2.10.** Modal analysis of the two major frequencies (1185 and 1296 Hz) shown in Fig. 2.9: (a) rail vertical mode at 1185 Hz. (b) rail longitudinal mode at 1291 Hz, in comparison with the closest vertical pin-pin mode at 1100 Hz shown in (c).

Studying corrugation by pre-selecting certain modes may lead to different and possibly non-physical results, thereby highlighting the subtleness of the corrugation problem. However, this also reveals one of the advantages of the proposed modelling approach, which can contain all necessary modes of the structure and continua in the system by modelling the relevant components and interfaces with realistic geometry and material properties. Several questions for further research could focus on the cut-off wavelength for filtering: what is the shortest cut-off wavelength for filtering? Could it be related to the shortest observed corrugation wavelength of 20 mm? Is the optimal cut-off frequency equal to 20 mm or should it be shorter? Is this frequency related to the concept of contact filter [57]?

According to the above discussion, instead of increasing to 1296 Hz, the major frequency in Fig. 2.9 should decrease from 1290 Hz at  $A = 2.5$   $\mu\text{m}$  toward the frequency of the vertical mode of 1185 Hz when the corrugation amplitude grows and the vertical mode becomes dominant. This mismatch is caused by the inconsistency between the modelled corrugation wavelength of 30 mm and the natural modes of the track, which are determined by the nominal track parameters used in the modelling. The prescribed wavelength is a field

observation related to deviation from the nominal track. The nominal track parameters do not necessarily cause corrugation; otherwise, corrugation would be observed everywhere. Because of this mismatch, the calculated wear tends to erase the corrugation.

### 2.5 Relationship between contact forces and wear as well as new insights

Based on the discussion in Section 4, it may be inferred that equal longitudinal and vertical natural frequencies may represent a condition for corrugation to consistently initiate and grow; this may be achieved by properly constraining the rail by the fastening system [58]. The next question is whether corrugation occurs at certain preferred frequencies. Because the natural modes should be excited by contact forces and dynamic contact forces are caused by corrugation, the effects of the prescribed corrugation on the normal and longitudinal forces are examined below. Note that for corrugation, the difference between the vertical and normal directions of wheel-rail contact is negligible.

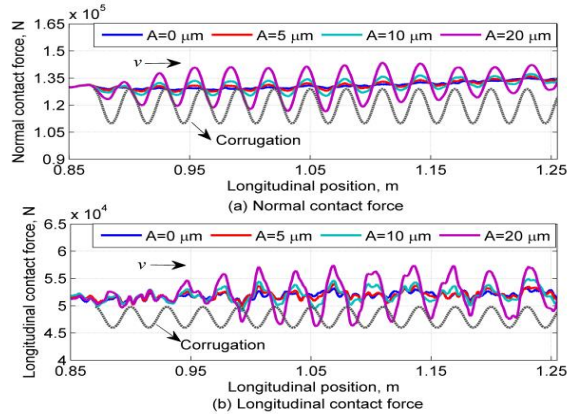
#### 2.5.1 Normal and longitudinal forces do not exactly follow corrugation in wavelength and phase

Fig. 2.11 shows the normal contact force ( $F_N$ ) and longitudinal contact force ( $F_L$ ) when the rail is smooth and when corrugation is present. Although the wavelength of the modelled corrugation is constant (30 mm), the wavelengths of the resulting dynamic wheel-rail contact forces vary along the rail (see Fig. 2.11a). Specifically,  $F_N$  initially lags behind the corrugation, i.e., the peak of  $F_N$  appears to the left side of the corresponding corrugation peak. When approaching the sleeper, which has a width of 140 mm and is centered at 1.20 m, the force catches up and becomes in phase with the corrugation at approximately 1.1 m, i.e., near the edge of the sleeper. The force subsequently tends to lead the corrugation. A similar situation applies to  $F_L$  (see Fig. 2.11b). However,  $F_N$  leads  $F_L$  initially, and the two forces later tend to be in phase at approximately 1.23 m, with subsequent lagging of  $F_N$ . Note that the wear is also strongest at approximately 1.23 m (according to Section 4.2).

The PSD analysis in Fig. 2.12a reveals that the main frequency components of  $F_N$  and  $F_L$  are 1257 Hz and 1226 Hz, respectively. The corresponding vertical and longitudinal rail vibration modes closest to the corrugation passing frequency of 1297 Hz are 1185 and 1291 Hz, which means that the normal and longitudinal contact forces do not exactly follow the excitation and have frequencies that are different from the natural vibration modes. Previous studies have either explicitly or implicitly assumed that the frequencies of the longitudinal contact

## 2 New insights into the short pitch corrugation enigma

force, the normal contact force and the vertical natural mode are the same as the corrugation passing frequency; however, the longitudinal mode has not been previously considered.



**Fig. 2.11.** Dynamic wheel-rail contact forces obtained for the corrugation in Fig. 2.3 with  $\theta = 0$  and P4 at 1.2 m (1.2 m is in the middle of a sleeper and 0.9 m is at the midpoint between two sleepers.).

### 2.5.2 Preferred frequency of contact forces

The dynamic normal and longitudinal contact forces are determined by the combined effects of the parameters of the structure, the excitation by the corrugation and the transient rolling contact. To investigate the contact force sensitivity to different corrugation wavelengths, the wavelength is varied at 28, 30, 31, 32 and 35 mm. Fig. 2.12 shows the relationships between the PSD and frequencies of the contact forces and the corrugation wavelength. The following observations can be made.

- 1) The frequencies of the normal and longitudinal forces are different. The frequencies of the contact forces are different from that of the excitation, i.e., the passing frequency of the corrugation, and they are sensitive to and change with the corrugation wavelengths. The dynamic forces are stronger at certain wavelengths than others. With the current track parameters, both the longitudinal and vertical contact forces are strongest at  $\lambda = 30$  mm. This again is in agreement with the observed corrugation wavelength of 30 mm.
- 2) The bandwidth of the frequency change of the longitudinal force is between 1116 Hz and 1288 Hz (Fig. 2.12a), which is narrower than that of the normal force

## 2 New insights into the short pitch corrugation enigma

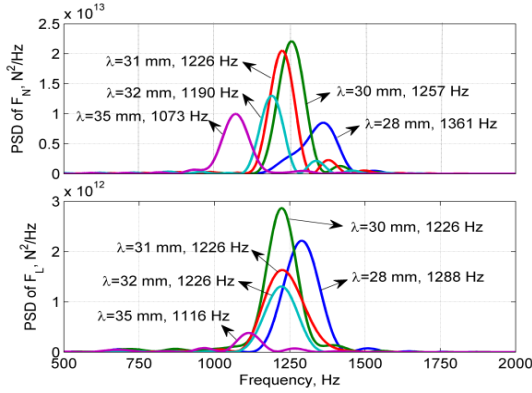
(between 1073 and 1361 Hz). The frequency band of the vertical force is broader because it follows the change in the corrugation wavelength as shown in Fig. 2.12b for the relatively constant ratio of the corrugation passing frequency to the contact force frequency. The frequency of the longitudinal contact force is lower than that of the normal contact force when the corrugation wavelength is short, i.e., between  $\lambda = 28$  mm and 31 mm (see Fig. 2.12b), and vice versa when the corrugation wavelength is longer than 31 mm.

- 3) The frequency of the normal contact force is always lower than that of the excitation (Fig. 2.12b). The presence of corrugation is an excitation mainly in the normal direction; thus, the response always follows the excitation. However, the frequency of the longitudinal contact force can be lower or higher than that of the excitation, which likely depends on the nearest natural frequency as well as the complex relationship between the tangential and normal contact forces. This pattern reveals a strong dependence of the normal contact force on the excitation and a relatively weaker dependence of the longitudinal contact force on the excitation. These dependencies are in line with the narrower band of the frequency change of the longitudinal force compared with the normal force.
- 4) In Fig. 2.12b, the frequency of the longitudinal contact force has the largest deviation from the corrugation passing frequency when the wavelength is shorter, i.e., at  $\lambda = 28$  mm. With increasing  $\lambda$ , the deviation decreases. At approximately  $\lambda = 31.5$  mm, the frequency of the longitudinal contact force equals the passing frequency. The longitudinal contact force subsequently follows the excitation closely.
- 5) The frequency curves (Fig. 2.12b) of the normal and longitudinal contact forces cross each other at a wavelength of 31 mm, where the frequencies of the normal and longitudinal forces are equal. Is an equal frequency of the two forces a condition for the corrugation to initiate, grow and become a wavelength fixing mechanism? As shown in Sections 4.2 and 5.1, the wear is strongest when the normal and longitudinal forces  $F_N$  and  $F_L$  are in phase at 1.23 m. Because an equal frequency is a necessary condition for  $F_N$  and  $F_L$  to be in phase over many wavelengths, it is indeed a favorable condition for corrugation development.

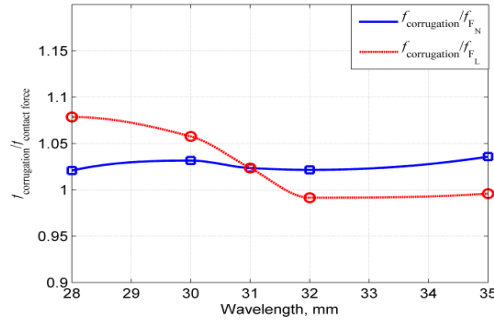
These observations indicate that the system appears to have a preference for certain frequencies, which is further confirmed by Fig. 2.12a, in which the frequency of the longitudinal contact force is 1226 Hz for  $\lambda = 30$  mm, 31 mm and 32 mm. This apparent preference is also in agreement with the results of [3], which show that most models in the

## 2 New insights into the short pitch corrugation enigma

literature suggest a fixed frequency related to *vertical* resonances in the system. However, this preference appears contrary to the hypothesis of fixed wavelength [1] and is part of the enigma of the corrugation problem: is the mechanism underlying corrugation a wavelength-fixing or frequency-fixing mechanism [3]?



(a) PSD of  $F_N$  (upper) and  $F_L$  (lower)



(b) Ratio of corrugation over contact force frequency

**Fig. 2.12.** Relationships between the PSD and frequencies of the contact forces and corrugation wavelength obtained for the corrugation in Fig. 2.3b with  $\theta = 0$ , P4 at 1.2 m and  $A = 20 \mu\text{m}$ . Note that in (b),  $f_{\text{corrugation}}$  is not constant but changes with the corrugation wavelength. Thus, although the PSD of  $F_L$  varies in a narrower band than  $F_N$  in (a), the opposite pattern is observed in (b).

### 2.5.3 Frequencies converge to develop uniform corrugation

Equal longitudinal and vertical natural frequencies have been shown to represent preferred conditions under which corrugation can initiate and grow; thus, it is reasonable to infer that the frequencies of the related contact forces and the resulting wear are also equal, such that the five different frequencies converge to one frequency: the corrugation passing

frequency. Therefore, the frequency appears to be fixed at a preferred resonance, whereas the wavelength is “fixed” in the sense that it can vary only in a small range. This supposition explains the observations in Section 5.2, in which the frequency converges to 1226 Hz while the preferred wavelength varies because of the mismatch between the given corrugation wavelength and the nominal track parameters. The strongest contact forces are at  $\lambda = 30$  mm, the frequencies of the longitudinal and normal forces are equal at  $\lambda = 31$  mm, and the frequency of the longitudinal force and the corrugation passing frequency are equal at  $\lambda = 31.5$  mm.

It is also reasonable to infer that when the track parameters that caused the observed corrugation are known and the mismatch between the model input and the prescribed corrugation is eliminated, all of the different wavelengths will converge to the observed wavelength of 30 mm if the traffic speed is 140 km/h, which implies that varying traffic speed can suppress corrugation by changing the wavelength as was shown in [59]. The problem for further research now becomes modelling degraded track to identify the track parameters at which the system converges to the preferred frequencies and wavelengths with a phase angle of wear that promotes corrugation growth at every wheel passage.

### 2.5.4 Importance of the proposed modelling approach and track parameters

Since the foundational work of Grassie [62-64], modelling corrugation has generally been based on wheel and rail sub-models that consist of beams and plates, and the wheel-rail contact is solved separately via statics and then coupled to the wheel-rail system. These calculations were limited by the state of the art. As far as contact mechanics, “the mechanics of steady or slowly varying creep forces has been very thoroughly studied, but the behavior under transient or rapidly oscillating conditions is virtually unexplored” [64]. The longitudinal dynamics of the wheel-rail interaction were investigated *experimentally* in [63], and *longitudinal* resonances higher than 900 Hz were observed. Such resonances were not considered important and thus were ignored in further investigations, and the focus for corrugation has been on vertical, lateral and wheelset torsional dynamics [1, 3, 39, 40, 55, 56]. In this paper, by analyzing the frictional rolling in the vehicle-track system under transient and rapidly oscillating conditions, the influence of both the vertical and the longitudinal vibration modes on corrugation initiation and growth was captured. However, further research should be performed that includes the influence of the track structure, especially the fastening, which plays a major role in constraining the rail and affecting its modes [58]. Studies have modelled fastenings and sleepers and identified their parameters [19, 50, 65, and 66], and these works have revealed that the alignment of the fastening



## 2 New insights into the short pitch corrugation enigma

system influences the frequency of normal and longitudinal dynamics and the natural frequencies are determined by the system parameters.

Fig. 2.1 shows different cases of corrugations under different track types, i.e., mono-block sleeper versus duo-block sleeper and W-shaped tension clamp versus Deenik clips. Comparing the three photos reveals that the characteristics of the corrugation differ from track to track. Certain corrugations are more or less uniformly distributed along the track (Fig. 2.1a), whereas others are more severe near the sleeper support (Figs. 2.1b and 2.1c). The difference between Fig. 2.1a and Figs. 2.1b and 2.1c is the types of sleepers and fastenings. According to Fig. 2.1b, the wavelength of the corrugation may vary significantly within a sleeper span. Moreover, Figs. 2.1b and 2.1c are from the same track and thus have the same traffic and same types of sleeper and fastening; however, large differences in the corrugations are apparent. These observations all indicate that corrugation is sensitive to track conditions, thus highlighting directions for future work.

### 2.5.5 Additional discussions

In this section, 2D and 3D analysis results are briefly compared. In [16], a 2D non-Hertzian contact model is developed in which the stress distribution is not symmetric at the falling and rising edges of the corrugation. The same phenomenon is observed in the present 3D numerical analysis. A clear difference between the 2D and 3D approaches is that in the 2D analysis, the contact patches at the falling and rising edges are symmetric in the longitudinal direction about the contact patch center. In the case of the 3D analysis, the contact patches are not symmetric about the contact patch center.

Wavelength fixing is also observed. In the Dutch railway network, the wavelength of the short pitch corrugation is 25–50 mm at a corresponding speed of 30–140 km/h. If the corrugation is purely determined by frequency fixing, then the wavelength should have varied in a broader range. Therefore, the numerical analyses and the field observations indicate that frequency fixing and wavelength fixing may have occurred simultaneously. One such possibility is that for a certain traffic speed, if the preferred frequency is  $nf_0$ , with  $f_0$  representing the fundamental frequency, the frequency will jump to harmonics of a higher frequency  $(n+i)f_0$ ,  $i \geq 1$  when the speed is increased so that the wavelength remains at the fixed wavelength.

As shown in Fig. 2.11a, approximately 2 wavelengths are required for the normal contact force to transit from the steady state before the corrugation, which starts at 0.87 m, to the new steady state controlled by the corrugation. For the tangential force, approximately 3.5 wavelengths are required. Thus, the longitudinal force lags approximately 1.5 wavelengths

## 2 New insights into the short pitch corrugation enigma

behind the normal force, i.e., approximately 45 mm. Because the length of the contact patch is approximately 15 mm (see Fig. 2.6), the lag is approximately three times the length of a contact patch. In [14], the lag for static rolling contact is 1 length of a contact patch, which reveals another difference between static and dynamic rolling contact. Moreover, Fig. 2.11 shows that the tangential contact force contains considerably more harmonics than the normal force.

Metallurgical investigations on corrugated rail material show that the corrugation crest experiences high dynamic contact forces, high deformation, work hardening, and, consequently, high wear resistance. The corrugation trough, instead, is reported to be developed from wear [11, 66]. This is in agreement with the numerical results in the present paper, i.e., high contact pressure is found at the corrugation crest and lower pressure and high micro-slip at the corrugation trough.

Although more research using more sophisticated models for the longitudinal support is needed, the findings of this paper have relevance for the numerical modelling of longitudinal modes. The inclusion of longitudinal support stiffness, such as in [63], results in a longitudinal mode at approximately 1298 Hz, which represents a difference of 7 Hz with respect to the model without longitudinal rail support. Hence, the more complex model does not result in a significant difference in the longitudinal dynamics. This situation should be further explored by investigating the actual parameters experimentally under Dutch conditions and verifying the dynamics.

## 2.6 Conclusions and future work

In this paper, the enigma of rail short pitch corrugation is examined using a novel modelling approach. Although the enigma remains unsolved, new insights on the phenomenon are described. The approach consists of simulating the vehicle-track dynamic interactions, which are directly and instantaneous coupled through frictional rolling contact. Wear is assumed to be the damage mechanism. The wheel, track and contact are treated in three dimensions so that the structural, geometric and material properties of the system and its components can be modelled sufficiently. The analysis concentrates on the transient rolling at the corrugation and the behavior of the vehicle-track system under the rapid oscillating loading of Dutch railway track and traffic in an effort to identify the preferred conditions under which corrugation can consistently initiate and grow. The findings and insights are summarized as follows.

## 2 New insights into the short pitch corrugation enigma

---

- Along the longitudinal centerline of the contact patch, increases in the contact area, maximum pressure, shear stress and micro-slip zone at the corrugation crest are small, and some of them even decrease with increases in the corrugation amplitude. For example, the increases of them at  $A = 20 \mu\text{m}$  in comparison to those at  $A = 0 \mu\text{m}$  (smooth rail) accordingly are  $3.8 \text{ mm}^2$  (contact area),  $74 \text{ MPa}$  (maximum pressure),  $-6.3 \text{ MPa}$  (maximum shear stress, “-” means decrease) and  $-5 \text{ mm}^2$  (micro-slip zone). However, changes at the corrugation trough are large. Likewise, they are  $27.9 \text{ mm}^2$  (contact area),  $-575 \text{ MPa}$  (maximum pressure),  $-295 \text{ MPa}$  (maximum shear stress) and  $14 \text{ mm}^2$  (micro-slip zone). The micro-slip increases from  $0.38 \text{ m/s}$  when  $A = 0 \mu\text{m}$  to  $0.55 \text{ m/s}$  at the corrugation trough while decreasing to  $0.24 \text{ m/s}$  at the corrugation crest when  $A = 20 \mu\text{m}$ . The large micro-slip and the significantly reduced contact pressure at the trough are the major contributions to the differential wear, which causes corrugation initiation and growth. The dependence of the normal contact force on corrugation excitation is strong, and the dependence of the longitudinal contact force on excitation is relatively weak.
- In addition to the commonly accepted hypothesis for corrugation studies, i.e., the vertical vibration modes of the vehicle-track system determine the development of corrugation, it is found that the longitudinal vibration modes are also important. Longitudinal modes are more important for the initiation of corrugation, and when the corrugation amplitude is sufficiently large, the vertical modes will be dominant. For intermediate situations, the longitudinal and vertical modes together determine whether the corrugation will grow or be suppressed by wear depending on whether the wear is of the necessary consistent frequency and phase.
- The frequencies of the vertical and longitudinal vibration modes and contact forces as well as the resulting wear are different, which is inconsistent with the literature, in which these frequencies are assumed to be equal; longitudinal vibration modes have not been previously considered. Consequently, a condition (that might not be unique) for corrugation to consistently initiate and grow is that the longitudinal and vertical natural frequencies are equal. This equivalence may be achieved by properly constraining the rail by fastening.

The modelling and findings agree with field observations (Fig. 2.1) of the distribution of corrugation with different severities. The proposed modelling is promising for corrugation analyses. Future work may include identifying the track parameters required for the system to converge to the preferred frequencies and wavelengths and investigating the phase-fixing mechanism of wear that promotes corrugation growth at every wheel passage. To

this end, the first focus should be on rail fastening. Previous work has shown that the fastening system, including the rail pads, has a strong influence on the vertical and longitudinal dynamics.

## References

- [1] Grassie SL. Rail corrugation: characteristics, causes, and treatments. *P I Mech Eng F-J Rai* 223 (2009) 581–596.
- [2] Sato Y, Matsumoto A, Knothe K. Review on rail corrugation studies. *Wear* 253 (2002) 130–139.
- [3] Afferrante L, Ciavarella M. Short pitch corrugation of railway tracks with wooden or concrete sleepers: An enigma solved? *Tribol Int* 43 (2010) 610–622.
- [4] Meehan PA, Bellette PA, Horwood RJ. “Does god play dice with corrugations?”: Environmental effects on growth. *Wear* 314 (2014) 254–260.
- [5] Giannakos K. Modelling the influence of short wavelength defects in a railway track on the dynamic behavior of the non-suspended masses. *Mech Syst Signal Pr* 68-69 (2016) 68–83.
- [6] Rodrigo Tavares de Freitas and Sakdirat Kaewunruen. Life Cycle Cost Evaluation of Noise and Vibration Control Methods at Urban Railway Turnouts. *Environments* 2016, 3(4), 34; doi:10.3390/environments3040034.
- [7] Li Z, Zhao X, Esveld C, Dollevoet R, Molodova M. An investigation into the causes of squats—correlation analysis and numerical modelling. *Wear* 265 (2008) 1349–1355.
- [8] Nielsen JCO. Numerical prediction of rail roughness growth on tangent railway tracks. *J Sound Vib* 267 (2003) 537–548.
- [9] Xie G, Iwnicki SD. Calculation of wear on a corrugated rail using a three-dimensional contact model. *Wear* 265 (2008) 1238–1248.
- [10] Böhmer A, Klimpel T. Plastic deformation of corrugated rails—a numerical approach using material data of rail steel. *Wear* 253 (2002) 150–161.
- [11] Baumann G, Fecht HJ, Liebelt S. Formation of white-etching layers on rail treads. *Wear* 191 (1996) 133–140.
- [12] Li Z, Zhao X, Dollevoet R, Molodova M. Differential wear and plastic deformation as causes of squat at track local stiffness change combined with other track short defects. *Vehicle Syst Dyn* 46 (2008) 237–246.
- [13] Saulot A, Descartes S, Berthier Y. Sharp curved track corrugation: From corrugation observed on-site, to corrugation reproduced on simulators. *Tribol Int* 42 (2009) 1691–1705.
- [14] Kalker JJ. Three-dimensional elastic bodies in rolling contact. *Kluwer*, Dordrecht, 1990.

## 2 New insights into the short pitch corrugation enigma

---

- [15] Li Z. Wheel-rail rolling contact and its application to wear simulation. *PhD dissertation*, Delft University of Technology, The Netherlands, 2002.
- [16] Nielsen JB. Evolution of rail corrugation predicted with a nonlinear wear model. *J Sound Vib* 227 (1999) 915–933.
- [17] Shen Z, Li Z. A fast non-steady state creep force model based on the simplified theory. *Wear* 191 (1996) 242–244.
- [18] Knothe K, Groß-Thebing A. Short wavelength rail corrugation and non-steady-state contact mechanics. *Vehicle Syst Dyn* 46(1–2) (2008) 49–66.
- [19] Ilias H. The influence of railpad stiffness on wheelset/track interaction and corrugation growth. *J Sound Vib* 227 (5) (1999) 935–948.
- [20] Jin X, Wen Z. Effect of discrete track support by sleepers on rail corrugation at a curved track. *J Sound Vib* 315 (2008) 279–300.
- [21] Grassie SL. Squats and squat-type defects in rails: the understanding to date. *P I Mech Eng F-J Rai* 226 (2012) 235–242.
- [22] Hempelmann K, Knothe K. An extended linear model for the prediction of short pitch corrugation. *Wear* 191 (1996) 161–169.
- [23] Saulot A, Baillet L. Dynamic finite element simulations for understanding wheel–rail contact oscillatory states occurring under sliding conditions. *J Tribol ASME* 128 (2006) 761–770.
- [24] Zhao X, Li Z. The solution of frictional wheel-rail rolling contact with a 3D transient finite element model: Validation and error analysis. *Wear* 271 (2011) 444–452.
- [25] Nishiura D, Sakaguchi H and Aikawa A. Development of Viscoelastic Multi-Body Simulation and Impact Response Analysis of a Ballasted Railway Track under Cyclic Loading. *Materials* 2017, 10(6), 615; doi:10.3390/ma10060615.
- [26] Li S, Li Z, Dollevoet R. Wear study of short pitch corrugation using an integrated 3D FE train-track interaction model. *The 9th international conference on contact mechanics and wear of rail/wheel systems*, Chengdu, China (2012) 216–222.
- [27] Zhao X, Wen Z, Wang H, Jin X and Zhu M. Modelling of high-speed wheel-rail rolling contact on a corrugated rail and corrugation development. *J Zhejiang Univ-Sc A* 15 (12) (2014) 946–963.
- [28] Zhao X, Li Z. A three-dimensional finite element solution of frictional wheel–rail rolling contact in elasto-plasticity. *P I Mech Eng J-J Eng* 229(1) (2015) 86–100.
- [29] Hiensch M, Nielson JCO, Verherjen E. Rail corrugation in The Netherlands – measurements and simulations. *Wear* 253 (2002) 140–149.
- [30] Molodova M, Li Z, Núñez A, Dollevoet R. Validation of a finite element model for axle box acceleration at squats in the high frequency range. *Comput Struct* 141 (2014) 84–93.
- [31] Arias-Cuevas O, Li Z, Lewis R. Investigating the lubricity and electrical insulation caused by sanding in dry wheel–rail contacts. *Tribol Lett* 37 (2010) 623–635.

- [32] Cann PM. The “leaves on the line” problem—a study of leaf residue film formation and lubricity under laboratory test conditions. *Tribol Lett* 24 (2006) 151-158.
- [33] Courant R, Friedrichs KO, Lewy H. On the partial difference equations of mathematical physics. *IBM J* 11 (1967) 215–234.
- [34] Benson DJ, Hallquist JO. A single surface contact algorithm for the post buckling analysis of shell structures. *Comput Method Appl M* 78 (1990) 141–163.
- [35] Popovici R. Friction in Wheel - Rail Contacts. *PhD dissertation*, University of Twente, The Netherlands, 2010.
- [36] Bhushan B. Modern Tribology Handbook: Principles of Tribology. vol. 34, *CRC Press*, Boca Raton, Florida, 2001.
- [37] Oostermeijer KH. Review on short pitch rail corrugation studies. *Wear* 265 (2008) 1231–1237.
- [38] Liu Q, Zhang B, Zhou Z. An experimental study of rail corrugation. *Wear* 255 (2003) 1121–1126.
- [39] Collette C, Horodincu M and Preumont A. Rotational vibration absorber for the mitigation of rail rutting corrugation. *Vehicle Syst Dyn* 47 (2009) 641–659.
- [40] Tassilly E and Vincent N, A linear model for the corrugation of rails. *J Sound Vib* 150 (1991) 25–45.
- [41] Li W, Wang H, Wen Z, Du X, Wu L, Li X and Jin X. An investigation into the mechanism of metro rail corrugation using experimental and theoretical methods. *P I Mech Eng F-J Rai* 230 (2016) 1025–1039.
- [42] Hayes WF, Tucker HG. Wheelset-track resonance as a possible source of corrugation wear. *Wear* 144 (1991) 211-226.
- [43] Suda Y, Komine H, Iwasa T, Terumichi Y. Experimental study on mechanism of rail corrugation using corrugation simulator. *Wear* 253 (2002) 162–171.
- [44] Jin X, Xiao X, Wen Z, Zhou Z. Effect of sleeper pitch on rail corrugation at a tangent track in vehicle hunting. *Wear* 265 (2008) 1163–1175.
- [45] Grassie SL and Johnson KL. Periodic microslip between a rolling wheel and a corrugated rail. *Wear* 101 (1985) 291 – 309.
- [46] Bellette PA, Meehan PA and Daniel WJT. Effects of variable pass speed on wear-type corrugation growth, *J Sound Vib* 314 (2008) 616–634.
- [47] Knothe KL, Grassie SL. Modelling of railway track and vehicle/track interaction at high frequencies. *Vehicle Syst Dyn* 22 (1993) 209–262.
- [48] Wei Z, Li Z, Qian Z, Chen R, Dollevoet R. 3D FE modelling and validation of frictional contact with partial slip in compression–shift–rolling evolution. *Int J Rail Transportation* 4(1) (2015) 20–36.
- [49] Li Z, Dollevoet R, Molodova M, Zhao X. Squat growth — some observations and the validation of numerical predictions. *Wear* 271 (1–2) (2011) 148–157.

## 2 New insights into the short pitch corrugation enigma

---

- [50] Oregui M, Li Z, Dollevoet R. An investigation into the vertical dynamics of tracks with monoblock sleepers with a 3D finite-element model. *P I Mech Eng F-J Rai* 230(3) 891–908.
- [51] Jin X, Wen Z, Wang K, Zhang W. Effect of a scratch on curved rail on initiation and evolution of rail corrugation. *Tribol Int* 37 (2004) 385–394.
- [52] Igeland A. Railhead corrugation growth explained by dynamic interaction between track and bogie wheelsets. *P I Mech Eng F-J Rai* 210 (1996) 11–20.
- [53] Archard JF. Contact and rubbing of at surfaces. *J Appl Phys* 24 (8) (1953) 981–988.
- [54] Molodova M. Detection of early squats by axle box acceleration. *PhD dissertation*, Delft University of Technology, The Netherlands, 2013.
- [55] Tassilly E, Vincent N. Rail corrugation: analytical model and field tests. *Wear* 144 (1991) 163–178.
- [56] Ahlbeck DR, Daniels LE. Investigation of rail corrugations on the Baltimore metro. *Wear* 144 (1991) 197–210.
- [57] Remington PJ. Wheel/rail noise-part IV: Rolling noise. *J Sound Vib* 46(3) (1976) 419–436.
- [58] Zhao X, Li Z. Dollevoet R. Influence of the fastening modelling on the vehicle-track interaction at singular rail surface defects. *J Comput Nonlin Dyn* 2014 9(3).
- [59] Meehan PA, Batten RD, Bellette PA. The effect of non-uniform train speed distribution on rail corrugation growth in curves/corners. *Wear* 366-367 (2016) 27–37.
- [60] Wu T, Thompson DJ. On the rolling noise generation due to wheel/track parametric excitation. *J Sound Vib* 293 (2006) 566–574.
- [61] Egana JI, Vinolas J, Gil-Negrete N. Effect of liquid high positive friction (HPF) modifier on wheel-rail contact and rail corrugation. *Tribol Int* 38 (2005) 769–774.
- [62] Grassie SL, Gregory RW, Harrison D, Johnson KL. The dynamic response of railway track to high frequency vertical excitation. *P I Mech Eng C-J Mec* 24 (1982) 77–90.
- [63] Grassie SL, Gregory RW, Johnson KL. The dynamic response of railway track to high frequency longitudinal excitation. *P I Mech Eng C-J Mec* 24 (1982) 97–102.
- [64] Grassie SL, Gregory RW, Johnson KL. The behaviour of railway wheelsets and track at high frequencies of excitation. *P I Mech Eng C-J Mec* 24 (1982) 103–111.
- [65] Egana JI, Vinolas J, Seco M. Investigation of the influence of rail pad stiffness on rail corrugation on a transit system. *Wear* 261 (2006) 216–224.
- [66] Oregui M, Núñez A, Dollevoet R, Li Z. Sensitivity analysis of railpad parameters on vertical railway track dynamics. *Accepted J Eng Mech-ASCE* (2016).
- [67] Feller HG, Waif K. Surface analysis of corrugated rail treads. *Wear* 144 (1991) 153–161.

# 3

## MECHANISM OF SHORT PITCH CORRUGATION: INITIAL EXCITATION AND CONSISTENCY CONDITION FOR INITIATION AND GROWTH

*This paper studies the short pitch corrugation initiation and growth mechanism by employing a three-dimension finite element vehicle-track interaction model including a detailed treatment of dynamic wheel-rail frictional rolling contact. The model considers the coupling between the structural dynamics and the contact mechanics, and assumes that the damage mechanism is differential wear. Firstly, a hypothesis for a consistent corrugation initiation and growth process is proposed. Secondly, the dominance of the longitudinal rail vibration modes in the corrugation initiation proposed in [18] is further investigated. In addition, the assumption in [18] that the consistency of the wavelength and phase angle in the vertical and longitudinal dynamic contact forces, resulting differential wear and corrugation determines the corrugation's continuous initiation and growth is further elaborated. To reproduce the corrugation initiation from smooth rail, an "initial excitation" in the system's structural dynamics determined by railpad models is identified and considered. Under the initial excitation, an initial differential wear is obtained and identified to be dominated by rail longitudinal compression modes. The corrugation explained by the differential wear can consistently initiate and grow up to 80  $\mu\text{m}$  with the typical parameters used of the Dutch railway. The consistency in the vertical and longitudinal contact forces, the differential wear and corrugation are shown during the corrugation growth. Besides, a corrugation wavelength selection phenomenon can also be explained by the consistency. To the best knowledge of the authors, this is the first work in the literature that reproduces the consistent initiation and growth of short pitch corrugation.*

---

This chapter is based on the paper below:

Li Z, Li S, Zhang P, Nunez A, Dollevoet R. Mechanism of short pitch corrugation: initial excitation and consistency condition for initiation and growth. Submitted to a journal.



### 3.1 Introduction

#### 3.1.1 Problem statement and literature review

Rail corrugation has been known and investigated for more than one century [1]. There have been extensive experimental investigations [2–5], metallurgical characterization of the rail surface material microstructural changes [6–9], and analytical and numerical studies [10–21]. Some other research publications can be found in the review papers [1, 22–24]. Grassie and Kalousek [1] classified the corrugation into six different groups based on the damage mechanisms (wear or plastic deformation) and wavelength-fixing mechanisms (system resonances), i.e., corrugation of heavy haul, light rail, booted sleeper, contact fatigue, rutting and short pitch corrugation. Short pitch corrugation, or in its other name of “roaring rail” due to the noise radiation, has the following characteristics [1]: 1) the wavelength falls in the range of 20 – 80 mm and the amplitude can be up to 100  $\mu\text{m}$ ; 2) it predominantly occurs on straight tracks or at gentle curves; 3) field data show that the wavelength is insensitive to train speed [1, 12, 17, 25]. While most groups of the corrugation have been well understood, the formation mechanism of short pitch corrugation remains not completely clear [17, 19, 26]. In the rest of this paper, the term “corrugation” will refer to short pitch corrugation.

The corrugation development is to-date explained with the structural dynamics and a damage mechanism [19, 24, 27]. The dynamical process determines the corrugation wavelength. The main damage mechanism is considered to be differential wear [1, 16, 17, 28, 29].

The corrugation is a complex problem principally due to the wavelength-fixing mechanism not being explained from field data. In the literature, different explanations have been proposed for this mechanism. They consider either the instability of wheel-rail systems or structural dynamics. The instability of the wheel-rail system explanation relates the corrugation to stick-slip vibrations [28, 30]. The stick-slip vibrations are induced by the negative friction under saturated creep conditions [30], and do not apply to the corrugation on straight tracks or at gentle curves with relatively low tractions. The structural dynamics explanation includes factors like the P2 resonance (the unsprung mass vibrating on the track stiffness) at about 50~100 Hz [17, 31], the sleeper passing frequency [1, 32, 33], the wheelset second torsional resonances at 250~400 Hz [24, 34, 35], the “pinned-pinned” resonance at 400~1200 Hz where the wavelength equals twice the sleeper span [11, 36].

### 3 Initial excitation and consistency condition for initiation and growth

For the interested frequency range of the corrugation at high speed, the “pinned-pinned” resonance is most widely considered as the wavelength-fixing mechanism. Because of that, the corrugation is also named as “pinned-pinned resonance” corrugation [24]. The explanation built upon the “pinned-pinned” resonance is frequency-fixing instead of wavelength-fixing [37]. According to the frequency-fixing mechanism, the corrugation wavelength should increase linearly with train speed. However, field data show that corrugation was insensitive to the train speed variation [1, 12, 17, 25]. This disagreement was explained in [37], by proposing that the corrugation was formed by different wavelength-fixing mechanisms, i.e., pinned-pinned resonance is not the only wavelength-fixing mechanism. In addition, the “pinned-pinned” resonance is not sufficient to explain the corrugation due to the following reasons: 1) corrugation can also form on continuously supported tracks where pinned-pinned resonance does not exist [12, 23]; 2) the corrugation formed on Vancouver “Skytrain” shows no influence by different sleeper supports [12, 25]; 3) field data from British Rail Research and Cambridge University cannot be explained [12, 17].

In order to understand the wavelength-fixing mechanism, the significance of the contact mechanics was also addressed. To explain why the corrugations are observed only in the range of 20–80 mm, a contact filtering effect was proposed [13, 14, 38]. The contact filter guarantees that only corrugations falling in the short pitch range can grow. Then the wavelength-fixing mechanism is explained as certain structural dynamics causing the differential wear with their corresponding wavelengths falling into the amplification zone determined by the contact filter [14].

Many models have been developed to understand the corrugation formation mechanisms [10-19]. Besides linear contact mechanics models, the more complex non-Hertzian [13] and non-steady [16, 27] treatments of the wheel-rail contact were included. Models with those more complex features are expected to be more accurate; however, they have reported no corrugation growth [15, 16, 19]. Therefore, the formation mechanism of the corrugation remains elusive [17, 19, 26].

#### 3.1.2 Gap to bridge: Identify an initial excitation for corrugation initiation and a condition for consistent growth

To solve the enigma, we introduce assumptions of two necessary conditions for corrugation continuous initiation and growth motivated from the vast previous research and the corrugation-like waves often observed after rail squats [39]. In [19], the first necessary condition was proposed that rail longitudinal vibration modes are probably dominant for the corrugation initiation, and that for continuous corrugation initiation and growth, there

### 3 Initial excitation and consistency condition for initiation and growth

---

should be a consistency between the vertical and longitudinal contact forces, dynamical responses and the resulting wear.

In this paper, we propose the second necessary condition for corrugation initiation – the initial excitation – and then show that with a proper initial excitation the corrugation can indeed initiate and grow consistently.

Generally speaking, for dynamics-induced rail rolling contact failures to initiate, there should be an initial energy input to give an excitation to the system. This input is called the “initial excitation” in this paper. With this initial excitation, dynamic wheel-rail contact forces are generated in certain wavelength ranges and the dynamic contact forces result in differential wear and differential plastic deformation. After multiple wheel passages, defects form due to the accumulation of wear and plastic deformation. In the case of the corrugation, the initial excitation can be local geometrical irregularities (e.g., squats [39]), local material irregularities (inhomogeneity) and the associated geometrical irregularities (e.g., poor welds [40]), and anomalies that are often invisible in the track system. An important feature of the corrugation induced by local irregularities is that the local irregularities are often visible and the induced corrugation (-like) waves usually decay out over a finite number of wavelengths. In contrast, the corrugation with invisible initial excitation appears over a much longer distance.

The results in [15, 16, 19] give a reasonable explanation about why track systems with nominal parameters can be corrugation-free, consistent with field observations that corrugation appears on some types of track forms in some circumstances and not in others [37]. There have been some studies on the corrugation problem from the viewpoint of railpad [41-44]. Field data shows that fastening systems are influential in corrugation development [4, 19]. However, a gap needs to be filled about what track parameters induce the initial excitations that produce the fluctuation of wheel-rail contact forces and finally cause the differential wear and deformation, leading to consistent corrugation initiation and growth. Therefore, a hypothesis is proposed in this paper based on the two conditions discussed above to investigate whether the initial excitation and the necessary consistency can be achieved by controlling certain track parameters. For this, a 3D transient finite element (FE) vehicle-track frictional rolling contact model [19, 39, 45, 46] is employed to study the corrugation initiation and growth under different conditions.

#### 3.1.3 Structure of this paper

The structure of the paper is as follows. A hypothesis for a consistent corrugation initiation and growth process is proposed in Section 3.2. Section 3.3 introduces the FE vehicle-track

### 3 Initial excitation and consistency condition for initiation and growth

interaction model employed to verify the hypothesis of Section 3.2. In Section 3.4, the corrugation initiation from an initial excitation determined by the railpad modelling is shown. Section 3.5 studies the consistent corrugation growth from the corrugation initiated in Section 3.4. The consistency condition for continuous corrugation initiation and continuous growth is discussed and summarised, and wavelength selection and fixing is shown. Section 3.6 explains that the corrugation initiation is caused by the rail longitudinal compression modes. Finally, in Section 3.7 conclusions are drawn.

## 3.2 Hypothesis for a consistent corrugation initiation and growth process

Based on [19], the process of consistent corrugation initiation and growth is hypothesized and shown in Fig. 3.1a. It contains four steps.

**Step (a):** Smooth rail with initial excitation: The rail is smooth in the beginning. When the wheel rolls over the track with an initial excitation, dynamic responses of the track are induced, dynamic vertical and tangential contact forces arise and the resulting initial differential wear of certain wavelengths and phases are obtained through FE simulation. This wear causes the very initial corrugation whose severity is quantified with a maximal peak to trough distance  $(2A_{\max})_0$ . The initial excitation will be discussed in Section 3.4.1.

**Step (b):** Corrugated rail: After the first wheel passage, the obtained initial corrugation of  $(2A_{\max})_0$  is applied to the rail surface. It is proportional to and in antiphase with the initial differential wear. Antiphase means a wear peak causes a corrugation trough. Similarly, additional wear from Step (d) is added to the corrugation in the subsequent wheel passages.

**Step (c):** Differential wear by the joint excitation of the initial excitation and the corrugated rail: The rail is now with corrugation, which can be in its initial form of  $(2A_{\max})_0$  as from Step (a) or in a more advanced form of  $(2A_{\max})_i$  ( $i = 1, 2, 3, \dots$ ) as from Step (d). The corrugation is an additional excitation, besides the initial excitation. Both excitations can cause differential wear of their respective wavelengths and phases.

**Step (d):** Consistency of the differential wear: The growth of the corrugation will be determined jointly by the wear caused by the two excitations. For consistent initiation and growth, the wear should add up to each other so that  $(2A_{\max})_i > (2A_{\max})_{i-1}$ . This is the consistency condition. Now let the wheel roll over the corrugated rail, calculate the differential wear and check if the consistency condition is satisfied: If the condition is

### 3 Initial excitation and consistency condition for initiation and growth

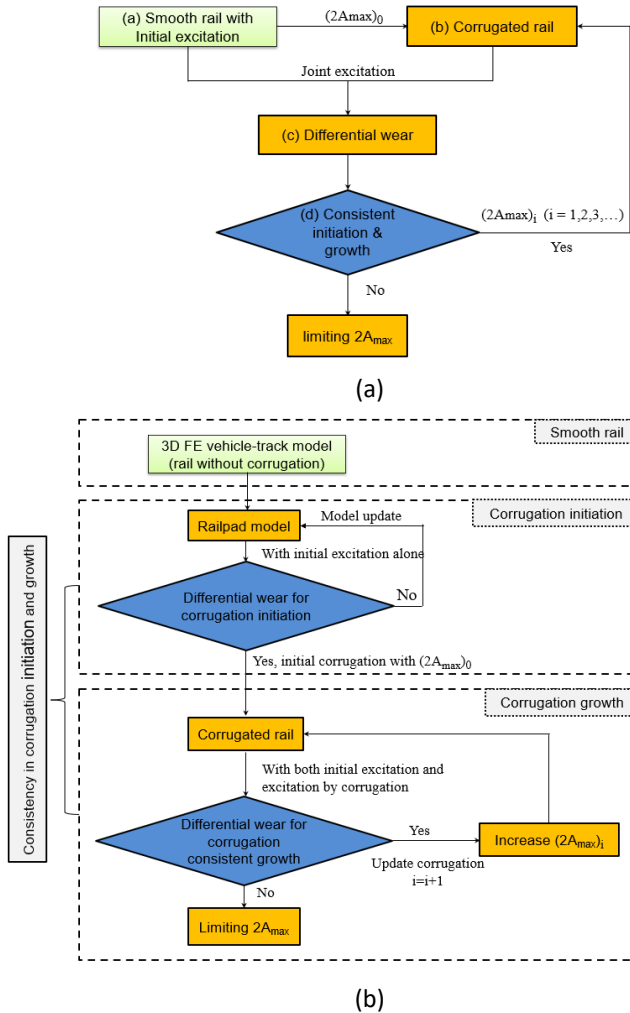


**Fig. 3.1.** The hypothesis for consistent initiation and growth of the corrugation. (a) The flowchart of the hypothesis; (b) the flowchart of the computer simulation that examines the hypothesis. Step (a) is examined in Section 3.4 and the rest in Section 3.5.

satisfied, repeat Steps (b), (c) and (d) with increased  $(2A_{\max})_i$  until a limiting  $2A_{\max}$ , with which the condition is not satisfied anymore, see Fig. 3.1b. It will be shown later in this paper that with a certain given set of parameters (e.g., RPM3, see Table 3.2 below), the corrugation initiates and grows consistently from smooth rail to corrugated rail of amplitude up to  $80\ \mu\text{m}$ , i.e., limiting  $2A_{\max} \geq 80\ \mu\text{m}$ . If the condition is not satisfied, it either means that the given set of parameters is not suitable for consistent initiation and growth of the corrugation (e.g., RPM1) and a suitable set of parameters should be sought. Alternatively,

### 3 Initial excitation and consistency condition for initiation and growth

it can mean that the damage mechanism is not differential wear (anymore), but, e.g., (differential) plastic deformation. The search for a suitable parameter set and the consideration of a different damage mechanism like plastic deformation are beyond the scope of this paper.

## 3.3 Model and methods

### 3.3.1 FE model

A 3D FE vehicle-track model is developed with Ansys/LS-Dyna [19]. Fig. 3.2 shows a schematic diagram of the model. The model is based on a symmetrical vehicle-track system of a straight track. Thus, a half-track and a half wheelset are considered. As the relevant frequency range of the corrugation is far higher than the vehicle vibration which is usually not higher than 10 Hz [47], car body and bogie structures above the primary suspension are lumped into a mass. Spring-damper elements represent the primary suspension. The wheelset, rail and sleepers are modelled with 3D finite elements. The radius of the wheel is 460 mm, with a conicity of 1/40. The rail is UIC 54 with a 1/40 inclination. Fastenings (mainly railpads are considered) and ballast are also modelled as spring-damper elements. Track parameters representing the typical Dutch railway system are referenced from [19, 48], as shown in Table 3.1. The solution zone with the meshing size of 0.8 mm starts at 0.3 m from the initial wheel location. The wheel-rail interaction is treated as surface-to-surface contact with a penalty method [49]. Coulomb's frictional law is applied, with the friction coefficient being 0.4. The longitudinal load is defined with a traction coefficient of  $\mu = 0.15$ .

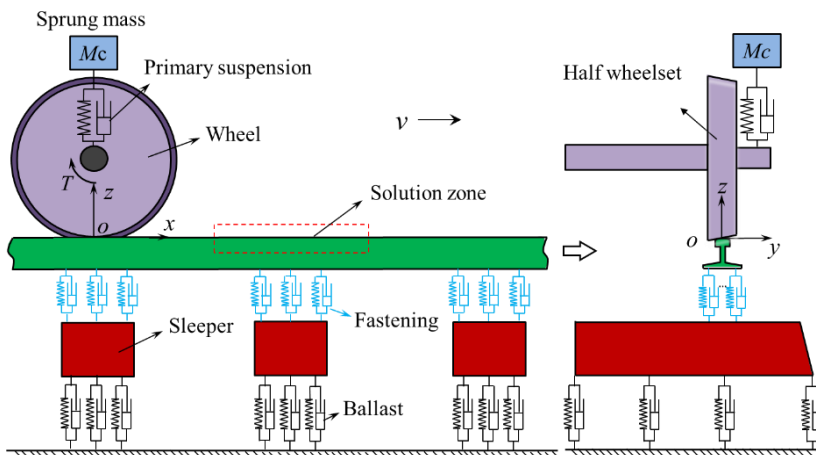


Fig. 3.2. Schematic diagram of the model

### 3 Initial excitation and consistency condition for initiation and growth

In the simulations, an implicit-explicit sequential approach is employed [45]. Firstly in the implicit analysis, the wheelset is placed into its initial location on the rail through a static equilibrium process; the corresponding initial stresses, strains, and displacement fields are determined. With these known fields as the initial state, the wheelset is set to roll with a speed of 140 km/h (the typical Dutch train speed) towards the solution zone. The explicit integration scheme is employed during this process to solve the wheel-rail frictional rolling contact problems. The time step is  $4.67 \times 10^{-8}$  s, small enough to meet the Courant stability condition [50]. Because of the nature of the explicit integration, the transient rolling contact and high-frequency dynamics of the vehicle-track system are automatically included in the solution.

**Table 3.1.** Vehicle parameters and Track parameters

Parameters			Parameters		
Values			Values		
Primary suspension	Sprung mass	7200 kg	Wheel and rail material	Young's modulus	210 GPa
	Stiffness	1.15 MN/m		Poisson's ratio	0.3
	Damping	2.5 kNs/m		Density	7,800 kg/m <sup>3</sup>
Railpad	Stiffness	1,300 MN/m	Sleeper	Young's modulus	38.4 GPa
	Damping	45 kNs/m		Poisson's ratio	0.2
Ballast	Stiffness	45 MN/m		Mass density	2520 kg/m <sup>3</sup>
	Damping	32 kNs/m		Spacing (L)	0.6 m

The model thus includes the vehicle and track structures. The dynamic interaction between them is through wheel-rail frictional rolling. The wheel-rail contact model has been verified by comparison with the established Hertz, Spence, Cataneo, Mindlin and Kalker solutions [45, 51]. Its ability to represent the vehicle-track structural dynamics has been shown with hammer tests [52] and axle-box acceleration measurements [53]. The model includes direct coupling between the contact mechanics and the structural dynamics; this renders it being able to explain problems arising from dynamic vehicle-track interaction such as rail squats development and the corrugation induced by squats [39, 48]. As noted in [54], the model “provides a very good explanation for the development of corrugation initiated from isolated railhead irregularities”. Further, the model has been used in [19] to study the corrugation with new insights gained about the conditions for corrugation initiation and growth, although the corrugation growth was not numerically reproduced there. Then, making use of the results in [19], this present paper further investigates the mechanism for consistent initiation and growth of the corrugation.

#### 3.3.2 Railpad models

Fig. 3.3 shows the modelling of a railpad (and fastening) in the FE model, representing the nominal track situation. The railpad is represented with  $m \times n$  spring-damper elements ( $m = 3, n = 4$ ) and constrains the rail in the longitudinal (x), lateral (y) and vertical (z) directions. Due to the degradation of railpads, e.g., by wear, the rail may not necessarily be in uniform contact with the railpads and hence not be uniformly constrained. Thus, the constraining conditions in the model should take this into account. Different configurations of the spring-dampers with various constraining conditions can be defined with different railpad models. The influences of the railpad modelling on the vertical and longitudinal contact forces excited by rail squats have been studied by Zhao et al. [55]. It was identified that railpad modelling plays an important role in high-frequency vehicle-track interactions. Since there is a certain relationship between squats and corrugation [39], the effects of railpad models are also studied in this paper.

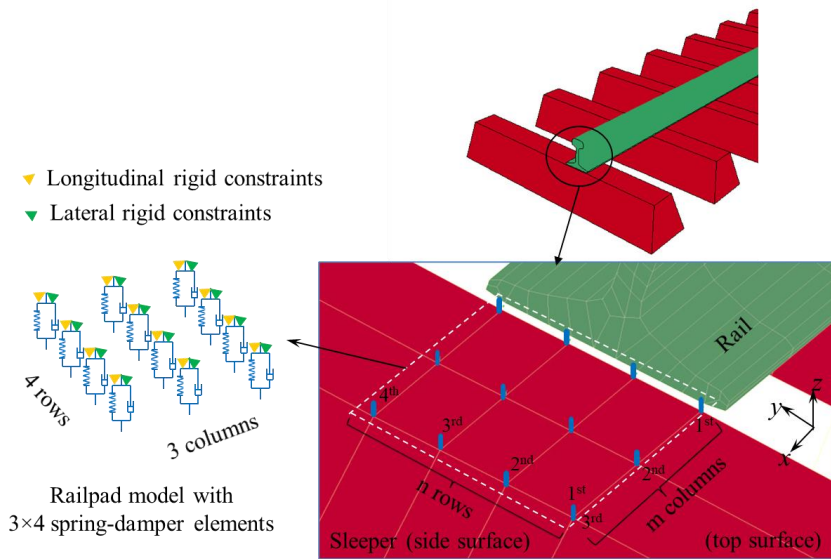


**Fig. 3.3.** Railpad model (RPM1)

In order to investigate the effects of railpads on corrugation initiation, five railpad models (RPM) are designed as shown in Table 3.2. RPM1 is employed in Section 3.3 to show a railpad model that does not give rise to corrugation as in [19]. RPM3 is used in Sections 3.3, 3.4 and 3.5 to investigate the consistent initiation and growth of the corrugation. RPM2, RPM4 and RPM5 are introduced in Section 3.6 to show, in comparison with RPM3, which structural dynamics are dominant for the corrugation initiation.



### 3 Initial excitation and consistency condition for initiation and growth

**Table 3.2.** Five railpad models to understand the corrugation initiation

Railpad model (RPM)	Description of rail foot constraints	Purpose
1	Corresponding to Fig. 3.4a. <b>Vertical:</b> railpad stiffness <sup>1</sup> . <b>Longitudinal:</b> discretely & rigidly constrained at $m = 1 - 3$ . <b>Lateral:</b> discretely & rigidly constrained <sup>2</sup> at $n = 1 - 4$ .	1. To model a nominal track situation. 2. Relating to [19] and as a reference to show a railpad model which does not cause corrugation.
2	<b>Vertical:</b> as RPM1. <b>Longitudinal:</b> continuously <sup>3</sup> & rigidly constrained at all the nodes of the rail foot. <b>Lateral:</b> as RPM1.	To restrict the rail longitudinal compression modes to show that no longitudinal compression modes, no corrugation.
3	Corresponding to Fig. 3.4b. <b>Vertical:</b> as RPM1. <b>Longitudinal:</b> discretely & rigidly constrained <sup>4</sup> at $m = 2$ . <b>Lateral:</b> as RPM1.	To show a railpad model that gives initial excitation and causes consistent initiation and growth of the corrugation.
4	<b>Vertical:</b> continuously & rigidly constrained at all the nodes of the rail foot. <b>Longitudinal:</b> as RPM3 <b>Lateral:</b> as RPM1.	To show that rail bending does not cause the corrugation.
5	<b>Vertical:</b> as RPM4. <b>Longitudinal:</b> as RPM2. <b>Lateral:</b> as RPM1.	To restrict both the rail vertical bending and longitudinal compression modes. To show that rail longitudinal sheared vibration does not cause the corrugation.

<sup>1</sup>: the constraint has the vertical stiffness of a railpad.

<sup>2</sup>: as shown in Figs. 3.4a and 3.4b.

<sup>3</sup>: being continuously constrained means all the nodes at the rail bottom are constrained to the coordinate system.

<sup>4</sup>: as shown in Fig. 3.4b.

#### 3.3.3 Wear model

The damage mechanism is considered to be differential wear, which is assumed to be proportional to the accumulated frictional work done during wheel passages [11, 16, 53].

### 3 Initial excitation and consistency condition for initiation and growth

The frictional work at an element within the contact patch for a wheel passage is calculated as follows:

$$w(x, y) = kW_f(x, y) = k \sum_{i=1}^N \tau_i(x, y) v_i(x, y) \Delta t \quad (3.1)$$

where  $k$  is the wear coefficient,  $W_f(x, y)$  is the frictional work,  $\tau_i(x, y)$  and  $v_i(x, y)$  are the local tangential stress and slip, respectively,  $N$  is the number of time steps  $\Delta t$  during which the wheel passes through the element.

## 3.4 Corrugation initiation

In this section the corrugation initiation due to differential wear caused by initial excitation, i.e., the Step (a) of the hypothesized process of Section 3.2, is discussed.

### 3.4.1 The initial excitation

First, the initial excitation is identified. In the literature, the differential wear is found to be sensitive to railpads from both field observations and numerical modelling [4, 19, 55]. In [19], a railpad boundary condition corresponding to RPM1 is used, as shown in Fig. 3.4a, and it is concluded that the corrugation will not grow because of the inconsistency between the differential wear and the existing corrugation. Through parametric variation studies, it was observed that under some situations, the differential wear has higher power intensity in the corrugation wavelength range of 20 – 80 mm. One of such situations, RPM3 (Fig. 3.4b), is that, in comparison to RPM1 the railpad longitudinal rigid constraints are released in the first and third columns and maintained only in the second column. In such a case, a high amplitude of differential wear with wavelength components in the corrugation wavelength range is observed, see Fig. 3.5a. This railpad model could represent a situation where (more) wear occurs at the leading and trailing sides of railpads, changing the flexibility and constraining condition of the rail in the longitudinal direction. This railpad condition, i.e., RPM3, is considered as an initial excitation in the present study.

### 3.4.2 Initial differential wear

With this initial excitation, the spatial domain and wavelength domain distributions of the differential wear of RPM3 were obtained with the FE model of Section 3.3 and shown along with those of RPM1 in Figs. 3.5a and 3.5b. There are, with RPM3, four main wavelength components after a band-pass filtering in the range of the 20 – 80 mm, namely 39.4 mm (corresponding to 987 Hz with the speed of 140 km/h), 33.3 mm (1168 Hz), 28.6 mm (1360

### 3 Initial excitation and consistency condition for initiation and growth

Hz) and 24.9 mm (1562 Hz). The wavelength of 28.6 mm has the highest PSD magnitude and is thus dominant. The differential wear of RPM1 has much lower power intensity magnitudes in this wavelength range.

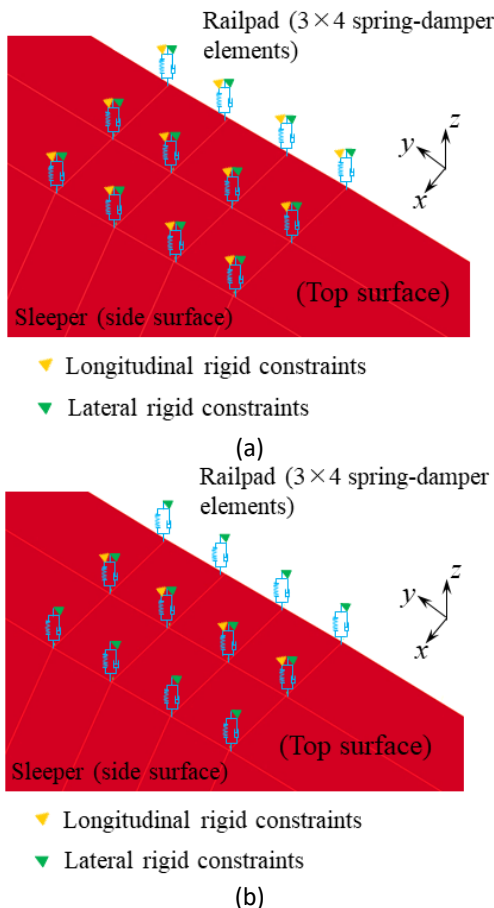


**Fig. 3.4.** Variation of railpad models: (a) RPM1 does not give rise to corrugation in [19] and (b) RPM3 gives rise to corrugation in this paper. RPM1 – 5 have the same lateral constraint.

Figs. 3.5c and 3.5d show a filed measurement of corrugation on the Dutch railway network. Looking at the spatial distribution of the simulated differential wear of RPM3 in Fig. 3.5a, it has a pattern similar to the field corrugation in Fig. 3.5c: they both have a periodicity of about 9 wavelengths [19]. Additionally, the main wavelength component of 28.6 mm in Fig. 3.5d from the measurement agrees well with that from the simulation with RPM3. The agreement between the simulation and measurement is due to the fact that the model uses

### 3 Initial excitation and consistency condition for initiation and growth

parameters of typical Dutch railway and the model has been validated in previous research for the Dutch situation [19, 39, 48].

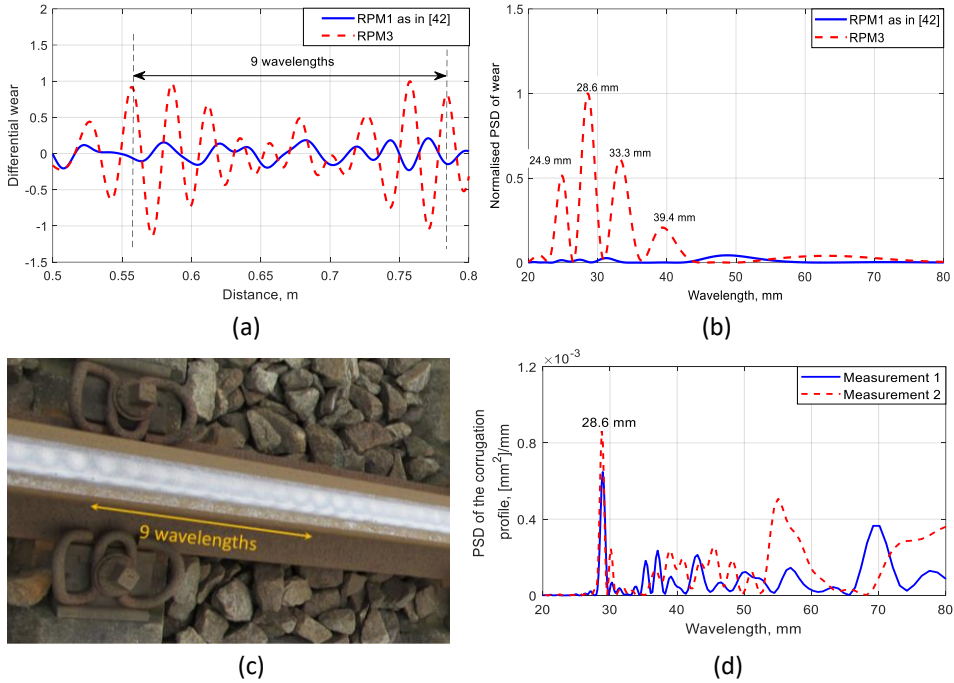


**Fig. 3.5.** Initial differential wear calculated with RPM1 and RPM3, 20–80 mm band-pass filtered, (a) in spatial domain (the differential wear is normalised with the maximum amplitude of the differential wear of RPM3); (b) in wavelength domain (the PSD is normalised with the magnitude of the dominant wavelength component of RPM3); (c) corrugation on a ballasted track with mono-block sleepers and fastenings with a W-shaped tension clamp. It was on a straight track near Assen, the Netherlands. The corrugation amplitude was non-uniform; (d) PSD of the field corrugation. The corrugation was measured with RAILPROF over 1 meter with a 5 mm sampling interval in the middle of the rail top surface.

#### 3.4.3 Longitudinal force dominates the corrugation initiation

The initial differential wear reflects the dynamic behavior of the wheel-rail interactions, which fixes the initial wavelength and phase of the corrugation. The contact forces, due to the wheel-rail dynamic interaction, act as the input to the damage mechanism. The relationship between the initial differential wear and the dynamic contact forces is studied in this section.

### 3 Initial excitation and consistency condition for initiation and growth

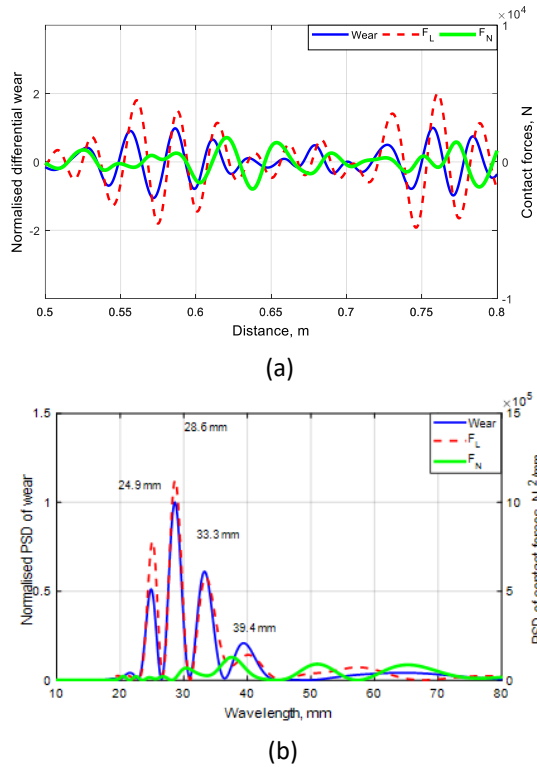


**Fig. 3.6.** Comparison between the initial differential wear and the contact forces (band-pass filter 20-80 mm) with RPM3 in spatial and wavelength domains. (a) Comparison in the spatial domain; (b) comparison in the wavelength domain.

Fig. 3.6 shows the differential wear and the corresponding longitudinal ( $F_L$ ) and vertical ( $F_N$ ) contact forces in spatial and wavelength domains. In the spatial domain, as shown in Fig. 3.6a, the differential wear and  $F_L$  are highly correlated, with approximately the same phase and with the same trend of amplitude variation, e.g., larger amplitudes near 0.575 m and 0.75 m. The slight phase difference between them is inherently due to the fact that  $F_L$  is the sum of longitudinal shear stress over the entire contact patch while the wear only appears at the rear part of the contact patch where micro-slip exists [45]. Further PSD analysis in Fig. 3.6b confirms that all the four main wavelength components of the wear can find their respective counterparts in the PSD of  $F_L$ , with corresponding wavelength and magnitude. The vertical contact force shows almost no apparent correlation with the wear in neither the spatial domain nor the wavelength domain. Therefore, we can conclude that  $F_L$  dominates the initial differential wear and, thus, corrugation initiation.

## 3.5 Corrugation consistent growth

This section discusses the consistent growth of the corrugation that is initiated by the differential wear calculated in Section 3.4, by following the Steps (b), (c) and (d) of Section 2.2. To this end, trial corrugations that are linearly proportional to and in anti-phase with the calculated initial differential wear of Section 3.4 is applied to the rail to see if the hypothesis holds.

### 3.5.1 Consistency between $2A_{\max} = 0$ and $10 \mu\text{m}$

An initial trial corrugation that is proportional to and in anti-phase with the initial differential wear under RPM3 in Fig. 3.6a (the blue line) and that is of amplitude  $(2A_{\max})_0 = 10 \mu\text{m}$  is applied to the rail of the FE model; this corresponds to Step (b). To form corrugation of  $10 \mu\text{m}$  amplitude requires many wheel passages in reality, but here the actual number of wheel passages is immaterial, as will be evident in the course of the discussion below. The wheel is then let roll over the corrugated rail and the resulting differential wear due to the joint excitation of the initial excitation and the initial corrugation is calculated, corresponding to Step (c), and compared in Fig. 3.7 with the differential wear under smooth rail that is shown in Fig. 3.6a. It can be seen that the differential wear of the smooth rail ( $2A_{\max} = 0$ ) and of the initially corrugated rail ( $2A_{\max} = 10 \mu\text{m}$ ) is in phase with each other (Fig. 3.7a) and has the same 4 main wavelength components (24.9 mm, 28.6 mm, 33.3 mm, 39.4 mm, Fig. 3.7b). Thus the differential wear caused by the joint excitation is consistent with the initial wear that is caused by the initial excitation alone so that the initial corrugation will grow, i.e., the condition for consistent initiation and growth is satisfied (Step (d)). By this, the hypothesis is verified to hold for corrugation amplitude up to  $10 \mu\text{m}$ .

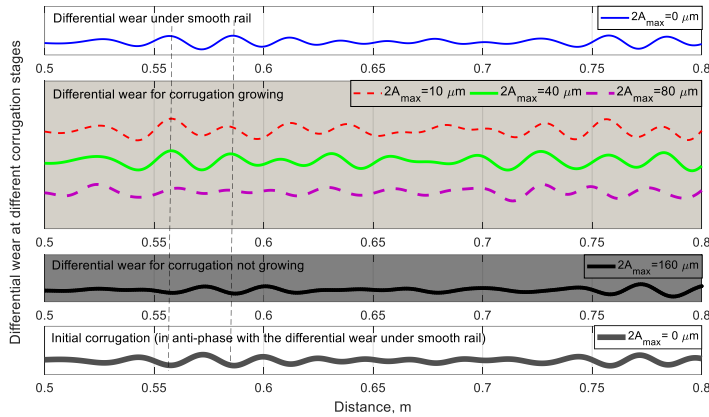
### 3.5.2 Consistency when $2A_{\max} > 10 \mu\text{m}$

The next question is: Until what  $2A_{\max}$  value the corrugation will consistently grow? Since the differential wear of the smooth rail and of the initially corrugated rail of  $(2A_{\max})_0 = 10 \mu\text{m}$  is in phase with each other and has the same 4 dominant wavelength components, we further scale the initial corrugation up to larger trial amplitudes  $(2A_{\max})_i = 40, 80, \text{ and } 160 \mu\text{m}$  to see if the hypothesis still holds. The calculated differential wear is compared in Fig. 3.7. Fig. 3.8 shows the corresponding vertical and longitudinal contact forces  $F_N$  and  $F_L$ , respectively, in both spatial and wavelength domains.

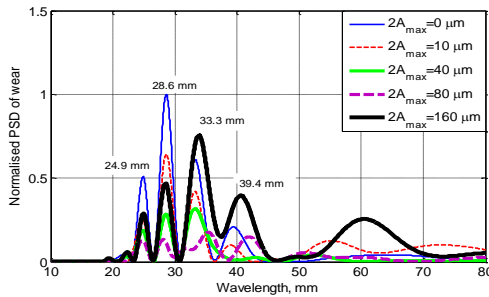
For better quantitative analysis, the wavelengths  $\lambda$  and the corresponding frequency  $f$  of the components of the differential wear, the corresponding longitudinal and vertical contact forces of Figs. 3.7 and 3.8 are shown in Table 3.3 along with the corresponding

### 3 Initial excitation and consistency condition for initiation and growth

wavelengths of the trial corrugations. Note that the trial corrugations are linearly scaled up from the initial differential wear, thus their wavelength compositions are identical for all the  $2A_{\max} = 0, 10, \dots, 160 \mu\text{m}$ , and are identical to those of the initial differential wear.  $f$  is calculated according to  $f = v/\lambda$ , where  $v = 140 \text{ km/h}$ . The first focus of the following analysis is on the wavelengths; the frequencies will then be examined in Section 3.5.4 against the relevant eigen frequencies of the system.



(a)



(b)

**Fig. 3.7.** Differential wear in spatial and wavelength domains with RPM3. (a) Differential wear in the spatial domain with increasing corrugation amplitude; (b) differential wear in the wavelength domain. The peak wavelengths at 24.9 mm, 28.6 mm, 33.3 mm and 39.4 mm correspond to  $2A_{\max} = 0$ .

### 3 Initial excitation and consistency condition for initiation and growth

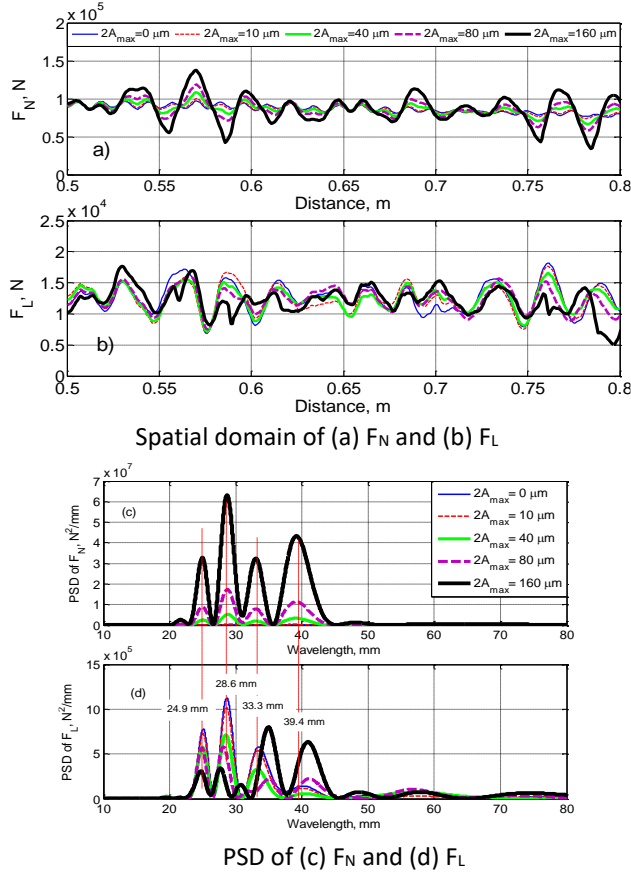


**Fig. 3.8.** Distributions of the contact forces in spatial and wavelength domains under RPM3. (a)  $F_N$  in the spatial domain; (b)  $F_L$  in the spatial domain; (c)  $F_N$  in the wavelength domain; (d)  $F_L$  in the wavelength domain.

To check the consistency, the relative deviations of the wavelengths of the components of the 3 quantities, i.e., the differential wear, longitudinal and vertical contact forces, are calculated and shown between the brackets in Table 3.3 after the corresponding wavelengths. A relative deviation is the absolute value of the difference between a wavelength and its reference wavelength divided by the reference wavelength. Here the reference wavelengths are those of the trial corrugation; they are in boldface in Table 3.3. As an example, the wavelength component 42.8 mm (of the differential wear at  $2A_{\max} = 40 \mu\text{m}$ ) corresponds to reference wavelength 39.4 mm, thus its relative deviation is 8.6%. Relative deviations are calculated for the frequencies in a similar way in Table 3.3b, in which the reference values are indicated with w.r.t., where necessary. A larger deviation means less consistency.



### 3 Initial excitation and consistency condition for initiation and growth

The consistency trend is shown in Table 3.3 with different colour contrasts: black, light green and green. The colour is determined for  $2A_{\max} > 0$  by simultaneously satisfying the following 3 conditions: (1) a number is set to green or light green if the relative deviations of *all the 3* (Table 3.3a) or *any 2* (Table 3.3b) of the corresponding components are not larger than 3.0%; (2) with condition (1) being satisfied, a number is set to light green if its relative deviation is larger than 1.0%; otherwise it is green. (3) Otherwise, a number is set to black. Taking  $2A_{\max} = 40 \mu\text{m}$  for example: the wavelength components corresponding to reference wavelength 39.4 mm are 42.8, 39.9 and 39.0 mm for the differential wear, longitudinal and vertical forces, respectively. They are in black in Table 3.3a for all the 3 quantities because one of them has a deviation of 8.6%, whereas in Table 3.3b, their colour is black, light green and green, because the respective deviations are 8.6%, 1.3% and 1.0%.

For  $2A_{\max} = 0$  and for the eigen frequencies of the compression and bending modes in Table 3.3b, a number is set to green, light green or black if the deviation is  $\leq 1.0\%$ , between  $1.0 \sim 3.0\%$  and  $> 3.0\%$ , respectively.

Overall, being in black in Table 3.3 could be considered as inconsistency.

**Table 3.3:** Development trend of consistency between the wavelength components of the 3 quantities (differential wear, longitudinal and vertical contact forces) with increasing trial corrugation amplitude  $2A_{\max}$  by looking at their relative deviations (between brackets) w.r.t. the corresponding wavelengths of the trial corrugation (in bold face).  $\lambda$ : wavelength;  $f$ : frequency;  $f = v/\lambda$ , where  $v = 140 \text{ km/h}$ . The numbers are coloured, depending on their relative deviation. In general: green is related to small relative deviation, thus strong consistency; light green is related to intermediate relative deviation, thus relatively weaker consistency; black is related to large relative deviation, thus no consistency. The colour is determined as follows:

For  $2A_{\max} > 0$ : The following 3 conditions are simultaneously satisfied: (i) a number is set to green or light green if the relative deviations of *all the 3* of (Table 3.3a) or of *any 2* (Table 3.3b) of the corresponding components are not larger than 3.0%; (ii) with condition (i) being satisfied, a number is set to light green if its relative deviation is larger than 1.0%; otherwise it is green. (iii) Otherwise, a number is set to black

For  $2A_{\max} = 0$ : a number is set to green, light green or black if its relative deviation is  $\leq 1.0\%$ , between  $1.0 \sim 3.0\%$  or  $> 3.0\%$ , respectively.

**Table 3.3a.** Trend shown by the green and light green colour indicates that (1) there is a consistency between all the 3 quantities and (2) the consistency reduces with increasing corrugation amplitude.

Dynamic quantities	2A <sub>max</sub> = 0 µm (Smooth rail)		2A <sub>max</sub> = 10 µm		2A <sub>max</sub> = 40 µm		2A <sub>max</sub> = 80 µm		2A <sub>max</sub> = 160 µm	
	λ (mm)	f (Hz)	λ (mm)	f (Hz)	λ (mm)	f (Hz)	λ (mm)	f (Hz)	λ (mm)	f (Hz)
Trial corrugation	39.4 33.3 28.6 24.9	987 1168 1360 1562	λ and f are the same as for smooth rail							
Differential wear	39.4 33.3 28.6 24.9	987 1168 1360 1562	39.4 (0.0%) 33.3 (0.0%) 28.6 (0.0%) 24.9 (0.0%)	987 1168 1360 1562	42.8 (8.6%) 33.2 (0.3%) 28.6 (0.0%) 24.9 (0.0%)	909 1172 1360 1562	41.9 (6.3%) 35.3 (6.0%) 28.1 (1.7%) 24.9 (0.0%)	929 1102 1386 1562	40.6 (3.0%) 33.8 (1.5%) 28.5 (0.3%) 24.9 (0.0%)	959 1151 1367 1562
Longitudinal contact force	39.8 (1.0%) 33.5 (0.6%) 28.6 (0.0%) 25.0 (0.4%)	977 1161 1360 1556	39.8 (1.0%) 33.4 (0.3%) 28.6 (0.0%) 25.0 (0.4%)	977 1165 1360 1556	39.9 (1.3%) 33.2 (0.3%) 28.5 (0.3%) 24.9 (0.0%)	975 1172 1365 1562	41.0 (4.1%) 35.0 (5.1%) 31.9 (4.2%) 28.1 (1.7%) 24.8 (0.4%)	949 1111 1219 1384 1569	40.9 (3.8%) 34.9 (4.8%) 30.7 (7.3%) 27.7 (3.1%) 24.7 (0.8%)	951 1115 1267 1404 1575
Vertical contact force	37.6 (4.6%) 30.4 (8.7%) 26.7 (6.6%) 24.6 (1.2%)	1035 1280 1457 1581	38.6 (2.0%) 33.1 (0.6%) 29.0 (1.4%) 25.1 (0.8%)	1008 1175 1341 1550	39.0 (1.0%) 33.0 (0.9%) 28.8 (0.7%) 24.9 (0.0%)	997 1179 1351 1562	39.1 (0.8%) 33.0 (0.9%) 28.7 (0.3%) 24.9 (0.0%)	995 1179 1355 1562	39.1 (0.8%) 33.0 (0.9%) 28.7 (0.3%) 24.9 (0.0%)	995 11791 35515 62

**Table 3.3b.** Trend shown by the colour indicates that with increasing corrugation amplitude (1) the consistency between the longitudinal force and the other 2 quantities reduces; (2) The relative deviations of the vertical force continuously reduce.

Dynamic quantities	2A <sub>max</sub> = 0 µm (Smooth rail)		2A <sub>max</sub> = 10 µm		2A <sub>max</sub> = 40 µm		2A <sub>max</sub> = 80 µm		2A <sub>max</sub> = 160 µm	
	λ (mm)	f (Hz)	λ (mm)	f (Hz)	λ (mm)	f (Hz)	λ (mm)	f (Hz)	λ (mm)	f (Hz)
Trial corrugation	39.4 33.3 28.6 24.9	987 1168 1360 1562	λ and f are the same as for smooth rail							
Differential wear	39.4 33.3 28.6 24.9	987 1168 1360 1562	39.4 (0.0%) 33.3 (0.0%) 28.6 (0.0%) 24.9 (0.0%)	987 1168 1360 1562	42.8 (8.6%) 33.2 (0.3%) 28.6 (0.0%) 24.9 (0.0%)	909 1172 1360 1562	41.9 (6.3%) 35.3 (6.0%) 28.1 (1.7%) 24.9 (0.0%)	929 1102 1386 1562	40.6 (3.0%) 33.8 (1.5%) 28.5 (0.3%) 24.9 (0.0%)	959 1151 1367 1562
Longitudinal contact force	39.8 (1.0%) 33.5 (0.6%) 28.6 (0.0%) 25.0 (0.4%)	977 1161 1360 1556	39.8 (1.0%) 33.4 (0.3%) 28.6 (0.0%) 25.0 (0.4%)	977 1165 1360 1556	39.9 (1.3%) 33.2 (0.3%) 28.5 (0.3%) 24.9 (0.0%)	975 1172 1365 1562	41.0 (4.1%) 35.0 (5.1%) 31.9 (4.2%) 28.1 (1.7%) 24.8 (0.4%)	949 1111 1219 1384 1569	40.9 (3.8%) 34.9 (4.8%) 30.7 (7.3%) 27.7 (3.1%) 24.7 (0.8%)	951 1115 1267 1404 1575
Vertical contact force	37.6 (4.6%) 30.4 (8.7%) 26.7 (6.6%) 24.6 (1.2%)	1035 1280 1457 1581	38.6 (2.0%) 33.1 (0.6%) 29.0 (1.4%) 25.1 (0.8%)	1008 1175 1341 1550	39.0 (1.0%) 33.0 (0.9%) 28.8 (0.7%) 24.9 (0.0%)	997 1179 1351 1562	39.1 (0.8%) 33.0 (0.9%) 28.7 (0.3%) 24.9 (0.0%)	995 1179 1355 1562	39.1 (0.8%) 33.0 (0.9%) 28.7 (0.3%) 24.9 (0.0%)	995 1179 1355 1562
Frequency of longitudinal compression mode, Hz	1025 (3.9% w.r.t. 987), 1187 (1.6% w.r.t. 1168), 1360 (0.0% w.r.t. 1360), 1546 (1.0% w.r.t. 1562) of RPM3, corresponding to Figure 3.11b, obtained by looking at nodal displacement, because in RPM3 the longitudinal motion is rigidly constrained so that a modal analysis is not possible.									
Frequency of vertical bending mode, Hz	1 987 (0.0%), 1003 (1.6%), 1012 (2.5%), 1024 (3.7%), 1033 (4.7%), 1035 (4.9%), 1045 (5.9%), 1073 (8.7%), w.r.t. 987 2 1088 (6.8%), 1117 (pin-pin resonance) (4.4%), w.r.t. 1168 3 1553 (0.6%), 1585 (1.5%), 1615 (3.4%), 1624 (4.0%) w.r.t. 1562 of RPM3.									

### 3 Initial excitation and consistency condition for initiation and growth

#### 3.5.2.1 Differential wear

##### 3.5.2.1.1 There is an overall limiting $2A_{\max}$

Fig. 3.7a shows in the spatial domain the differential wear with increasing corrugation amplitude. When  $(2A_{\max})_i$  is up to  $40\text{ }\mu\text{m}$ , the differential wear is overall in-phase with the initial differential wear and in anti-phase with the existing corrugation, with decreasing amplitudes. This guarantees that the existing corrugation from the differential wear can consistently grow.

When  $(2A_{\max})_i$  is  $160\text{ }\mu\text{m}$ , the differential wear is almost in antiphase with the initial differential wear (see for instance at  $0.60\text{ m}$ ), i.e., in-phase with the existing corrugation; Step (d) does not hold. In this case, the existing corrugation will be levelled out. By applying the corrugation with the trial amplitude  $2A_{\max} = 160\text{ }\mu\text{m}$ , we do not mean that the corrugation will necessarily grow until such a severe stage; instead, an intermediate limiting  $2A_{\max}$  should exist, with which the corrugation development reaches a saturation state, i.e., without further accumulation of differential wear. The power spectral densities of the differential wear are shown in Fig. 3.7b. For  $(2A_{\max})_i = 0, 10, 40$  and  $80\text{ }\mu\text{m}$ , there is an overall decreasing trend of the PSDs with increasing  $2A_{\max}$ , in-line with the observation from Fig. 3.7a, where the amplitude of the differential wear decreases with increasing corrugation amplitude. The PSD of  $2A_{\max} = 160\text{ }\mu\text{m}$  breaks the trend; it is not only the strongest for the 2 longer wavelengths ( $39.4$  and  $33.3\text{ mm}$ ), but also strong for the 2 shorter wavelengths. This break of the trend leads to the change of the wear from anti-phase to in-phase with the corrugation, causing the corrugation to stop growing.

##### 3.5.2.1.2 Tendency towards the smallest wavelength

The colour contrasts in Table 3.3 show the trends of the consistency development with increasing  $2A_{\max}$ . From Table 3.3a, it is clear that the consistency between the 3 quantities reduces with increasing  $2A_{\max}$ . Only at  $24.9\text{ mm}$ , the 3 quantities remain in green with all the trial  $2A_{\max}$ . This means a tendency for the corrugation to develop towards the smallest wavelength ( $24.9\text{ mm}$ ).

##### 5.2.1.3 Longer wavelength tends to stop growing at smaller $2A_{\max}$

It can further be observed from Table 3.3a that with longer wavelength the inconsistency takes place at smaller  $2A_{\max}$  with larger relative deviation. Specifically, the wavelengths of  $24.9\text{ mm}$  and  $28.6\text{ mm}$  components remain approximately constant for  $(2A_{\max})_i = 0, 10, 40$  and  $80\text{ }\mu\text{m}$ , with the largest relative deviation being  $1.7\%$  (Table 3.3); On the other hand, the largest relative deviations of the 2 longer wavelength components are much larger, and

### 3 Initial excitation and consistency condition for initiation and growth

take place at smaller  $2A_{\max}$ : For wavelength 39.4 mm, the largest deviation (8.6%) occurs with  $2A_{\max} = 40 \mu\text{m}$ ; for wavelength 33.3 mm, it (6.0%) occurs at  $2A_{\max} = 80 \mu\text{m}$ . Since a large deviation means higher inconsistency, this also shows that the limiting  $2A_{\max}$  is not the same for corrugation components of different wavelengths. Longer wavelength corrugation thus tends to have a smaller limiting amplitude  $2A_{\max}$ . In other words, longer wavelength seems to tend to stop growing earlier.

#### 3.5.2.1.4 Tendency for dominant component to jump to large wavelength

It is also observed in Fig. 3.7b that the dominant wavelength component tends to jump to its larger neighbouring one, according to the PSD, from 28.6 mm to 33.3 mm, when the amplitude increases from  $10 \mu\text{m}$  to  $40 \mu\text{m}$ .

The two tendencies of Sections 3.5.2.1.2 and 3.5.2.1.4 are conflicting. It is reasonable to infer that they will cause the overall corrugation wavelength to converge to an intermediate wavelength and that the inconsistency between the conflicting tendencies will cause the corrugation to stop at an overall limiting  $2A_{\max}$  as observed in Section 3.5.2.1.1. The effects of the tendency discussed in Section 3.5.2.1.3 would depend on the PSD of the longer wavelength components relative to that of the shorter wavelength components.

#### 3.5.2.2 Contact forces

Referring to Fig. 3.8a, the fluctuation of  $F_N$  increases with increasing corrugation amplitude, as the vertical force is a response to the excitation by the corrugation. On the other hand the amplitude of the  $F_L$  shows no such a trend but varies depending on the position along the track, indicating a weaker correlation between the longitudinal force and the excitation. Further, two new components, similar to sidebands, start to appear in  $F_L$  with wavelength 31.9 mm and 35.0 mm at  $2A_{\max} = 80 \mu\text{m}$ , corresponding to 1219 Hz and 1111 Hz respectively, in comparison to 33.2 mm at  $2A_{\max} = 40 \mu\text{m}$ , corresponding to 1172 Hz. It is not rare for new vibration frequencies to appear during the evolution of non-linear dynamic systems [58].

The trend shown by the colour in Table 3.3b indicates that (A) when  $2A_{\max} = 0 \sim 10 \mu\text{m}$ , the consistency between the differential wear and longitudinal force is higher than that between the wear and the vertical force, meaning that the corrugation initiation is dominated by the longitudinal force. It also indicates that (B) with increasing corrugation amplitude, (B1) the consistency between the longitudinal force and the other 2 quantities reduces; (B2) The relative deviations of the vertical force continuously reduce, i.e. the consistency between the vertical force and the differential wear increases; these means that the growth of the corrugation is gradually dominated by the vertical force.

### 3.5.3 Wavelength selection and fixing

From the above discussion it becomes clear that the overall corrugation wavelength would converge to an intermediate wavelength of the corrugation components, and the corrugation would not grow infinitely, but will stop at a limiting amplitude.

Looking at Figs. 3.7b, 3.8c and 3.8d, 28.6 mm is an intermediate wavelength and has for most of the cases the highest PSD and with high consistency; it thus could develop into the dominant corrugation components as observed in the field shown in Fig. 3.5d.

### 3.5.4 Relation with eigen frequencies

The frequencies of the longitudinal compression and vertical bending modes close to the frequencies of the differential wear, longitudinal and vertical forces are shown in Table 3.3b for RPM3. All the 4 longitudinal force components can find their counterpart longitudinal eigen modes at 1025, 1187, 1360 and 1546 Hz, with relative deviations 3.9%, 1.6%, 0.0% and 1.0%, respectively. This can explain why the 4 corresponding wavelengths appear in the initial differential wear and thus in the corrugation. The deviations are due to the prescribed track parameters that determine the eigen frequencies. No efforts were made to tune the deviations to zero. It should also be possible to tune the parameters so that there is only one dominant wavelength like what is shown in Fig. 3.5d.

No nearby eigen frequency can be found for the vertical force component at 1457 Hz. This shows that the vertical modes are not important for the corrugation initiation. Note that there is a vertical mode at 987 Hz. But this 987 Hz is not relevant to the 987 Hz of the differential wear, as will be shown in Section 3.6. Although one of the vertical force components does not have its eigen frequency counterpart, all the 4 force components become, with increasing  $2A_{\max}$ , more consistent to their respective corresponding components of differential wear; this indicates that it is the positive forced-vibration feedback loop between the trial corrugation and the resulting vertical contact force that gradually dominates the corrugation growth. Here it is assumed that the track parameters do not change, while in reality they change due to degradation under the dynamic interaction.

### 3.5.5 Summary

Summarizing, the simulation shows that (1) The hypothesis for the consistent initiation and growth of the corrugation is valid; (2) Multiple wavelength components can co-exist for the hypothesis to hold; (3) The corresponding wavelengths of the differential wear, the resulting corrugation, longitudinal and vertical contact forces are consistent when the

### 3 Initial excitation and consistency condition for initiation and growth

---

corrugation is below certain limiting amplitude and such a consistency reduces with increasing corrugation magnitude; (4) The limiting corrugation amplitudes differ for different wavelength components; (5) Components of longer wavelength seem to have a lower limiting corrugation amplitude, i.e. with longer wavelength the inconsistency takes place at smaller  $2A_{\max}$  with larger relative deviation; (6) The decreasing consistency tends to cause the corrugation to converge to the smallest wavelength; (7) The dominant corrugation component seems to tend to jump to the next longer wavelength component when the corrugation amplitude increases; (8) The conflicting tendency of converging to the smallest wavelength and of jumping to a longer wavelength should select and fix the wavelength at an intermediate wavelength; (9) The inconsistency between the conflicting tendencies will cause the corrugation to stop at an overall limiting  $2A_{\max}$ ; (10) Amplitude of differential wear per wheel passage decreases with increasing corrugation amplitude when the corrugation is below limiting amplitude; (11) The fluctuation of  $F_N$  increases with increasing corrugation amplitude; this is not the case with the longitudinal contact force.

## 3.6 The corrugation-initiating wear is caused by rail longitudinal compression modes

In this section, we examine what happens in the rail concerning the wheel-rail contact and show as proposed in [19] that it is the rail longitudinal vibration modes, instead of the rail vertical bending or longitudinal shear, that are dominant for corrugation initiation. To this end, the RPM1–5 in Table 3.2 are designed to identify the vibration mode that is responsible for the initial differential wear of the corrugation.

### 3.6.1 Vertical rail bending is not responsible for the corrugation initiation

Fig. 3.9 shows the  $F_L$  under the different support conditions RPM1 - 4. The following observations can be made: (1) The difference between RPM3 and RPM4 is that in RPM4 the vertical degree of freedom of all the nodes at the rail bottom is rigidly constrained, so that rail vertical bending is not possible. Although the  $F_L$  under these two boundary conditions of RPM3 and RPM4 is different in spatial and wavelength domains, the magnitudes are comparable, in contrast to those of RPM1 and RPM2, whose PSD is negligible. This indicates that the vertical rail bending is not the decisive factor for  $F_L$ . (2) The  $F_L$  of RPM3 and RPM4 with and without rail vertical bending both show large fluctuations, in contrast to those of RPM1 and RPM2, because RPM3 and RPM4 are longitudinally constrained only at  $m = 2$ ,

### 3 Initial excitation and consistency condition for initiation and growth

whereas RPM1 and RPM2 are more rigidly constrained in the longitudinal direction. This indicates that the longitudinal vibrational modes are much more important for the fluctuation of  $F_L$ . (3) Comparing the  $F_L$  of RPM1 and RPM2 in Fig. 3.9a tells that RPM2 has almost no fluctuation, whereas RPM1 still has some. This is because that RPM2 is rigidly constrained in the longitudinal direction at all the nodes of the rail foot bottom, in contrast to the longitudinal rigid constraint for RPM1 that is only applied at  $m = 1, 2$  and  $3$ .

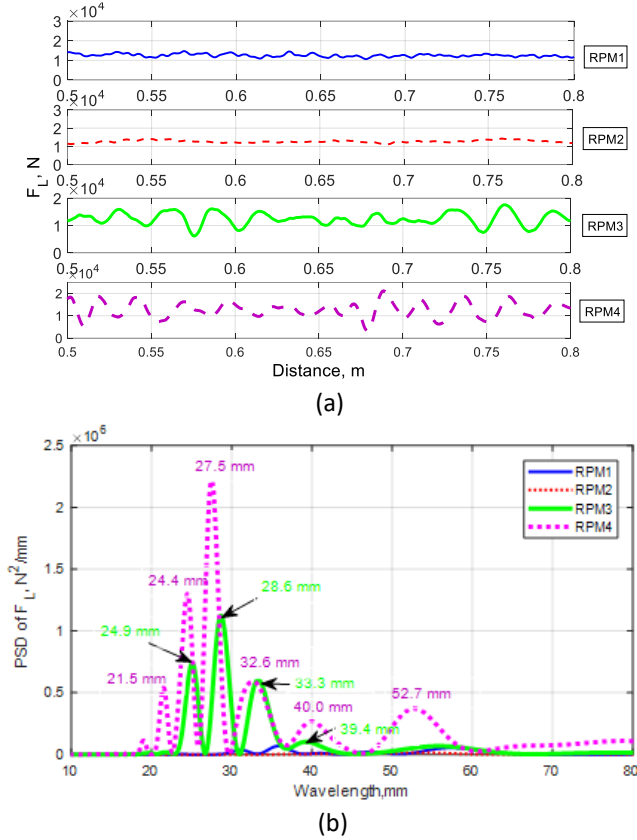


**Fig. 3.9.** Longitudinal contact forces  $F_L$  under RPM1 – 4. (a)  $F_L$  in the spatial domain; (b)  $F_L$  in the wavelength domain. The results were obtained with  $2A_{\max} = 0$  (smooth rail).

The differential wear under RPM4 is shown in Fig. 3.10. There is a close correlation between the wear and the  $F_L$  in both spatial and wavelength domains, and there exists a phase difference between the differential wear and  $F_L$ . These results agree with those in Sections 3.4 and 3.5 and confirm that  $F_L$  dominates the initial differential wear and, thus, corrugation initiation.



### 3 Initial excitation and consistency condition for initiation and growth

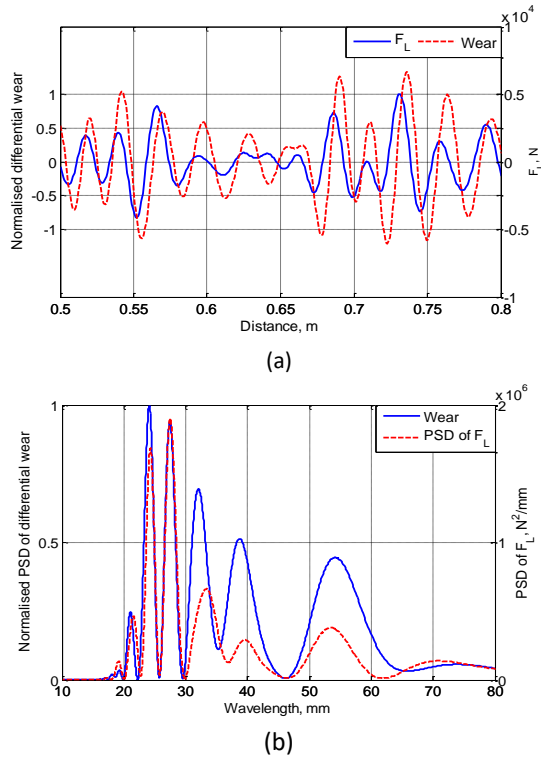


**Fig. 3.10.** Comparison of differential wear and  $F_L$  under RPM4 (band-pass filter 20-80 mm). (a) Comparison in the spatial domain; (b) comparison in the wavelength domain. The results were obtained with  $2A_{\max} = 0$  (smooth rail).

The displacement of a node in the middle of the rail contact surface is shown in Fig. 3.11. This node is at position 0.6 m inside the solution zone and it is above a sleeper. When rail vertical bending is allowed, as is the case by RPM1 – 3, the node displacement follows an overall rising trajectory when the wheel rolls over it from left to right (Fig. 3.11a). The PSD of the node displacement (Fig. 3.11b) shows a general agreement with the PSD of  $F_L$  (Fig. 3.9b), except for the relative magnitude of the corresponding wavelength components. When the bending motion of the rail is not allowed as by RPM4, the displacement of the node is generally horizontal, fluctuating around  $-40 \mu\text{m}$ , i.e., without the overall rising trend (Fig. 3.11a). Its overall negative value is due to the backward shear deformation caused by the longitudinal tangential force. This analysis confirms that the overall rising longitudinal displacement in Fig. 3.11a with RPM1 – 3 is due to the vertical bending of the rail. The exclusion of rail vertical bending vibration suppresses the overall rising longitudinal displacement but cannot prevent the fluctuations of  $F_L$ , initial differential wear and the longitudinal displacement.

### 3 Initial excitation and consistency condition for initiation and growth

In summary, these observations show that the vertical bending vibration is not responsible for the corrugation initiation.

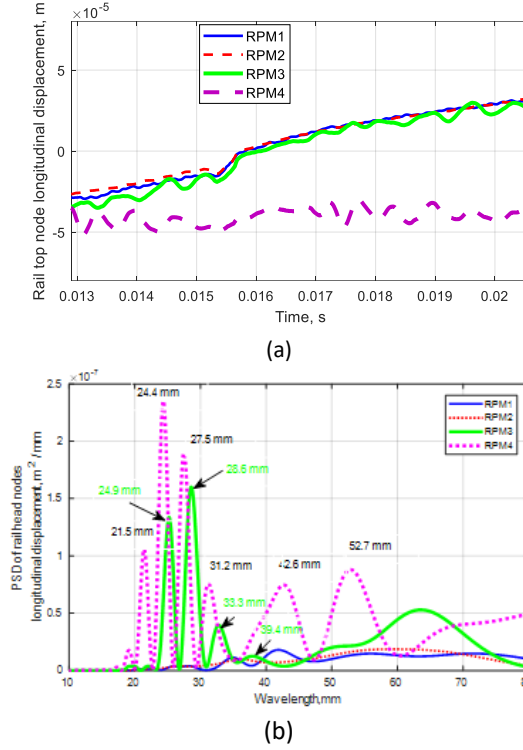


**Fig. 3.11.** Longitudinal displacement of a node in the middle of the rail top surface at  $x = 0.6$  m when the wheel rolls from the left side at  $x = 0.5$  m over the node to the right till  $x = 0.8$  m (nodes are from a cross-section next to 0.6 m to avoid the influence from the railpad constrained boundary). (a) Node displacement in the time domain; (b) node displacement in the wavelength domain. The results were obtained with  $2A_{max} = 0$  (smooth rail).

#### 3.6.2 Longitudinal rail shear is not responsible for the corrugation initiation

After excluding the vertical bending vibrations, we will investigate in this section whether rail longitudinal sheared vibration and/or longitudinal compression/rarefaction vibration are responsible for the corrugation initiation. To this end, RPM4 and RPM5 are designed and compared. With RPM4, the rail foot bottom is continuously and rigidly constrained in the vertical direction, but in the longitudinal direction only the motion of the central column

### 3 Initial excitation and consistency condition for initiation and growth

spring-damper elements is rigidly constrained. With RPM5, the rail foot bottom is constrained continuously and rigidly in both the vertical and longitudinal directions.

Fig. 3.12 shows the longitudinal contact force with RPM4 and RPM5. Only the model with RPM4 can develop corrugation. It can be observed that the responses with RPM5 are rather flat with minor fluctuations. With such a longitudinal contact force, the initial differential wear is not sufficient to develop corrugation; then, with RPM5, corrugation will not initiate nor grow.

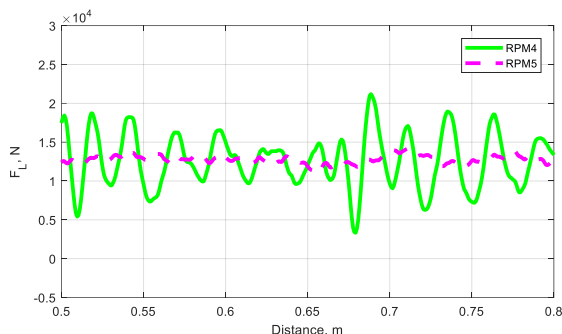


**Fig. 3.12.** Longitudinal contact force  $F_L$  in the spatial domain with RPM4 and RPM5. The results were obtained with  $2A_{\max} = 0$  (smooth rail).

Figs. 3.13a and 3.13c show the longitudinal displacements of three nodes located in the middle of the rail top surface (Node 1), at rail web (Node 2), and rail foot (Node 3) using RPM4 and RPM5, respectively. Fig. 3.13b and 3.13d show the displacements of the cross-section (in magenta) relative to the original rail cross-section without loading (in green) for RPM4 and RPM5 at three moments: before contact, during contact and after contact with the wheel. The rolling direction of the wheel is from left to right in the figure, see the vector of velocity  $v$ .

In Fig. 3.13a, with RPM4, longitudinal displacements of the three nodes are characterized by a constant component and a fluctuation component varying over time. The constant components are approximate  $-4 \times 10^{-5}$  m for rail top, 0 m for rail web and  $2.5 \times 10^{-5}$  m for rail foot. The three constant components in Fig. 3.13a can be explained by the longitudinal sheared motion, which appears consistently at the three moments in Fig. 3.13b (before, during and after contact with the wheel). The rail cross-section at the three moments is sheared in the direction opposite to the wheel rolling direction due to the applied traction, with the rail top moving backward (to the left of the figure), and rail foot moving forward (to the right of the figure), both relative to the original rail cross-section. Further, the fluctuation components of the longitudinal displacement of the three nodes are in phase. This means, the fluctuation component that causes corrugation (as explained in Fig. 3.10)

### 3 Initial excitation and consistency condition for initiation and growth

corresponds to an in-phase vibration over the whole rail cross-section, which should be the rail longitudinal compression vibration (modes). The results in Figs. 3.13a and 3.13b indicate that with RPM4, the rail in the longitudinal direction can experience both longitudinal sheared and longitudinal compression/rarefaction vibrations.

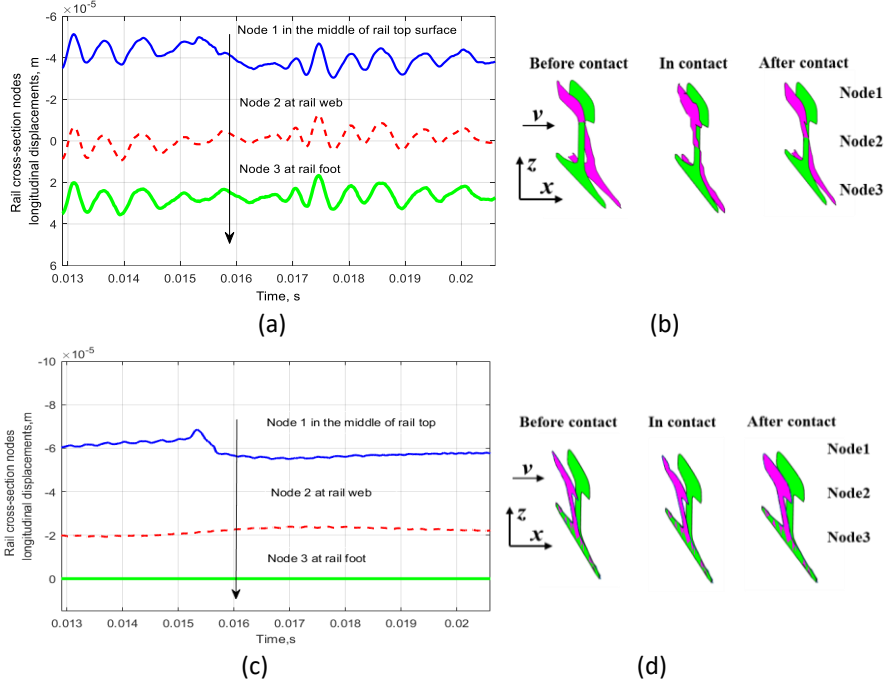


**Fig. 3.13.** Longitudinal displacement of three nodes (node 1 is in the middle of rail top surface; node 2 in the rail web; node 3 in the rail foot) in a rail cross-section at  $x = 0.6$  m when the wheel rolls from left side at  $x = 0.5$  m ( $t = 0.0129$  s) to the right till  $x = 0.8$  m ( $t = 0.0206$  s) with (a) RPM4 and (c) RPM5. The black downwards arrows in (a) and (c) indicate that the 3 curves in each of the 2 plots are in the sequence from rail top to rail foot. The displacements of the cross section relative to the original rail cross section without loading in (b) RPM4 and (d) RPM5 (Green: the original rail cross section; Magenta: the rail cross section after deformation.). The results were obtained with  $2A_{\max} = 0$  (smooth rail)

In Fig. 3.13c, with RPM5, longitudinal displacements of the three nodes are almost constant during the whole simulation due to the longitudinal constraint. The magnitudes are approximate  $-6 \times 10^{-5}$  m for the node at the rail top,  $-2 \times 10^{-5}$  m for the node at the rail web, and 0 m at the rail foot. The constant component with RPM5 at the rail head and the rail web are longitudinal sheared vibration opposite to the rolling direction due to traction. The rail foot is rigidly constrained in the longitudinal direction, and the longitudinal

### 3 Initial excitation and consistency condition for initiation and growth

displacement is shown as a flat line at 0 m (see Fig. 3.13d). The fluctuation component, which corresponds to longitudinal compression/rarefaction vibrations as explained in RPM4, does not appear in the longitudinal displacement of the three nodes with RPM5 in Fig. 3.13c. The results in Figs. 3.13c and 3.13d suggest that with RPM5, only longitudinal sheared motion of the rail is allowed in the longitudinal direction. The local peak displacement of node 1 between 0.015 – 0.016 s in Fig. 3.13c is the rail top displacement due to the wheel-rail contact that passes over node 1.

In conclusion, the rail longitudinal sheared vibration is present in both models RPM4 and RPM5, and longitudinal compression/rarefaction vibration is only present in model RPM4. As RPM4 can develop corrugation while RPM5 cannot, we conclude that longitudinal sheared vibration is not relevant for the corrugation. From Sections 3.6.1 and 3.6.2, it is concluded that the vertical bending and longitudinal sheared vibrations are not responsible for the corrugation development.

#### 3.6.3 The corrugation-initiating wear is caused by longitudinal rail modes

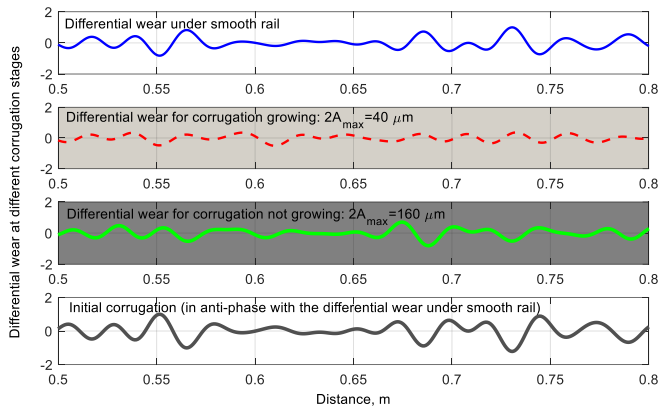
As shown in Fig. 3.13a, there is an in-phase fluctuation of the longitudinal vibrations of the cross-section nodes from the rail top surface to the rail foot. It indicates that there is an overall compression-rarefaction vibration (wave) of the rail in the longitudinal direction. From Figs. 3.9 – 3.11 with RPM4, the  $F_L$ , the longitudinal rail displacement vibrations and the initial differential wear are consistent with each other. The corrugation by the differential wear can therefore consistently initiate and grow under the rail compression-rarefaction vibrations, see Fig. 3.14. Specifically, when  $2A_{\max} = 40 \mu\text{m}$ , the differential wear is still in-phase with the initial differential wear with the smooth rail; this guarantees the corrugation to continue to grow. When  $2A_{\max} = 160 \mu\text{m}$ , the differential wear shows a trend to be antiphase with the initial differential wear, i.e., in-phase with the corrugation so that the corrugation cannot grow anymore. The consistency in the contact forces during corrugation growth is also observed, see Fig. 3.15. Similar to Fig. 3.8, inconsistency is only observed when the wavelength is longer than 40 mm. A summary of the results from the five railpad models is listed in Table 3.4. From the comparisons, as well as the observations made in Sections 3.6.1 and 3.6.2, it is concluded that longitudinal compression modes are the strongest and are decisive for the corrugation-initiating wear.

#### 3.6.4 Influence of rail inclination is negligible

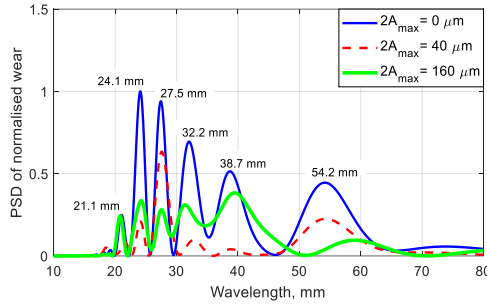
With RPM1 – 5, the rail inclination is 1/40. In the analysis so far, the influence of the inclination is not considered, as with rail inclination the lateral and torsional rail modes will

### 3 Initial excitation and consistency condition for initiation and growth

also be involved in the wheel-rail dynamic interactions. This influence is now evaluated with RPM3 by comparing the differential wear calculated with and without 1/40 inclination. Fig. 3.16 shows the distributions of the differential wear in the spatial domain. They have the same wavelength and phase angle. Note that there is a slight difference in the amplitude. However, this difference does not influence the corrugation wavelength and phase angle which determine the consistent corrugation initiation and growth. Therefore, the consistency in the initiation and growth of the corrugation is still valid. It can be concluded the rail inclination has a negligible influence on the initial differential wear and the corrugation development.



(a)



(b)

**Fig. 3.14.** Corrugation consistent initiation and growth under RPM4. (a) Differential wear in the spatial domain, (b) Differential wear in wavelength domain (band-pass filter 20-80 mm)

### 3 Initial excitation and consistency condition for initiation and growth

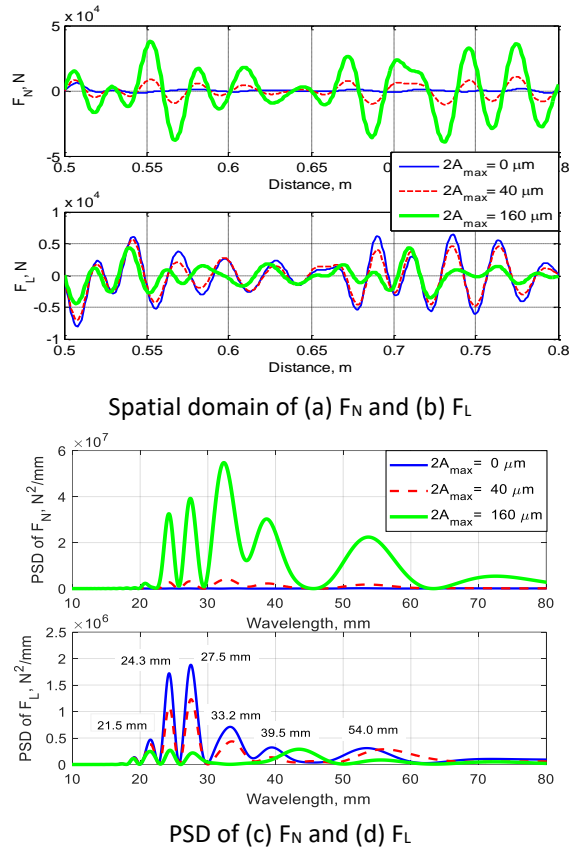


**Fig. 3.15.** Distributions of the contact forces in spatial and wavelength domains with RPM4 (band-pass filter 20-80 mm). (a)  $F_N$  in the spatial domain; (b)  $F_L$  in the spatial domain; (c)  $F_N$  in the wavelength domain; (d)  $F_L$  in the wavelength domain.

**Table 3.4.** Summary of results from RPM1–5 and rail without inclination

Railpad model	Results
RPM1:	Railpad model does not cause corrugation [19].
RPM2:	Railpad model does not cause corrugation.
RPM3:	Railpad model causes corrugation consistent initiation and growth.
RPM4:	Railpad model causes corrugation consistent initiation and growth.
RPM5:	Railpad model does not cause corrugation.
RPM3: (but without rail inclination)	Railpad model causes corrugation consistent initiation and growth

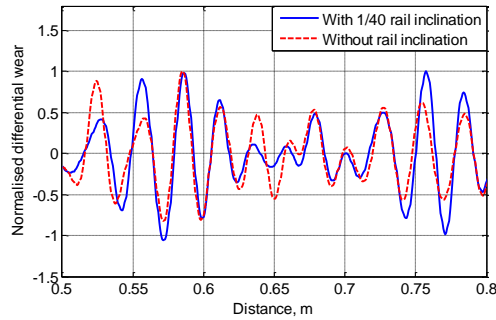


**Fig. 3.16.** Comparison of the differential wears with 1/40 and without rail inclination under RPM3 (band-pass filter 20-80 mm). The results were obtained with  $2A_{\max} = 0$  (smooth rail)

## 3.7 Conclusions

In this paper, the condition for continuous initiation and growth of short pitch corrugation is studied with a 3D vehicle-track interaction model including detailed consideration of dynamic wheel-rail frictional rolling contact. The differential wear, as the damage mechanism of the corrugation, is obtained to examine the consistency required for continuous corrugation initiation and growth. The main conclusions are as follows:

- 1) A hypothesized process for consistent corrugation initiation and growth is proposed and verified with numerical simulation.
- 2) The hypothesized process starts with an initial excitation which causes the initial corrugation by differential wear. The initial differential wear is found to be sensitive to the railpad models. Under certain conditions (e.g. RPM3), the differential wear has high amplitude with wavelength components in the wavelength range of the corrugation. Such railpad conditions are the initial excitation used in this paper.
- 3) The initial differential wear is determined by the longitudinal contact force. It has the same wavelength as the longitudinal contact force but with a slight phase difference.
- 4) The initial corrugation is caused by rail longitudinal compression modes. Contributions from rail vertical vibration, rail longitudinal sheared vibration and rail inclination are insignificant.
- 5) Once the initial corrugation due to the initial excitation occurs, the continuous growth of the corrugation depends on the consistency in the wavelength and phase of the differential wear that is caused by both the initial excitation and the existing corrugation. If the differential wear caused by both the initial excitation and the existing corrugation



### 3 Initial excitation and consistency condition for initiation and growth

---

has the same wavelength and a phase so that it adds to the existing corrugation, the corrugation can continuously and consistently grow.

- 6) Multiple wavelength components can co-exist in the differential wear, the resulting corrugation, longitudinal and vertical contact forces. They are consistent when the corrugation is below certain limiting amplitude. The limiting corrugation amplitude differs for different wavelength component.
- 7) The consistency condition also means a wavelength selection mechanism of the corrugation: (a) Only those wavelengths that satisfy the consistency can cause the corrugation; (b) Components of longer wavelength have a lower limiting corrugation amplitude.
- 8) It is observed that the amplitude of differential wear per wheel passage decreases with increasing corrugation amplitude when the corrugation is below limiting amplitude.

## References

- [1] Grassie S, Kalousek J. Rail corrugation: characteristics, cause and treatments. *P I Mech Eng F-J Rai* 207 (1993) 57–68.
- [2] Suda Y, Komine H, Iwasa T, Terumichi Y. Experimental study on mechanism of rail corrugation using corrugation simulator. *Wear* 253 (2002) 162–171.
- [3] Liu Q, Zhang B, Zhou Z. An experimental study of rail corrugation. *Wear* 255 (2003) 1121–1126.
- [4] Li W, Wang H, Wen Z, Du X, Wu L, Li X, Jin X. An investigation into the mechanism of metro rail corrugation using experimental and theoretical methods. *P I Mech Eng Part F-J Rai* 230 (2016) 1025–1039.
- [5] Vadillo EG, Tárrago J, Zubiaurre GG, Duque CA. Effect of sleeper distance on rail corrugation. *Wear* 217 (1998) 140–146.
- [6] Clayton P, Allery M. Metallurgical Aspect of Surface Damage Problems in Rails. *Canadian Metallurgical Quarterly* 21 (1982) 31–46.
- [7] Feller H, Walf K. Surface analysis of corrugated rail treads. *Wear* 144 (1991) 153–161.
- [8] Wild E, Wang L, Hasse B, Wroblewski T, Goerigk G, Pyzalla A. Microstructure alterations at the surface of a heavily corrugated rail with strong ripple formation. *Wear* 254 (2003) 876–883.
- [9] Zhang H, Ohsaki S, Mitao S, Ohnuma M, Hono K. Microstructural investigation of white etching layer on pearlite steel rail. *Mat Sci Eng A-Struct* 421 (2006) 191–199.
- [10] Grassie S, Gregory R, Harrison D, Johnson K. The dynamic response of railway track to high frequency vertical excitation. *P I Mech Eng C-J Mech* 24 (1982) 77–90.

### 3 Initial excitation and consistency condition for initiation and growth

- [11] Hempelmann K, Knothe K. An extended linear model for the prediction of short pitch corrugation. *Wear* 191 (1996) 161–169.
- [12] Bhaskar A, Johnson KL, Wood GD, Woodhouse J. Wheel-rail dynamics with closely conformal contact. Part 1. Dynamic modelling and stability analysis. *P I Mech Eng Part F-J Rai* 211 (1997) 11–26.
- [13] Nielsen J. Evolution of rail corrugation predicted with a non-linear wear model. *J Sound Vib* 227 (1999) 915–933.
- [14] Müller S. A linear wheel–rail model to investigate stability and corrugation on straight track. *Wear* 243 (2000) 122–132.
- [15] Jin X, Wen Z, Wang K. Effect of track irregularities on initiation and evolution of rail corrugation. *J Sound Vib* 285 (2005) 121–148.
- [16] Xie G, Iwnicki S. Simulation of wear on a rough rail using a time-domain wheel–track interaction model. *Wear* 265 (2008) 1572–1583.
- [17] Afferrante L, Ciavarella M. Short-pitch rail corrugation: A possible resonance-free regime as a step forward to explain the “enigma”? *Wear* 266 (2009) 934–944.
- [18] Zhao X, Wen Z, Wang H, Jin X, Zhu M. Modelling of high-speed wheel-rail rolling contact on a corrugated rail and corrugation development. *J Zhejiang Univ-Sci A (Appl Phys & Eng)* 15 (2014) 946–963.
- [19] Li S, Li Z, Núñez A, Dollevoet R. New insights into the short pitch corrugation enigma based on 3D-FE coupled dynamic vehicle-track modelling of frictional rolling contact. *Appl Sci* 7 (2017) 807.
- [20] Gómez I, Vadillo EG. A linear model to explain short pitch corrugation on rails. *Wear* 255 (2003) 1127–1142.
- [21] Oyarzabal O, Correa N, Vadillo EG, Santamaría J, Gómez J. Modelling rail corrugation with specific-track parameters focusing on ballasted track and slab track. *Veh Syst Dyn* 49 (2011) 1733–1748.
- [22] Sato Y, Matsumoto A, Knothe K. Review on rail corrugation studies. *Wear* 253 (2002) 130–139.
- [23] Oostermeijer K. Review on short pitch rail corrugation studies. *Wear* 265 (2008) 1231–1237.
- [24] Grassie S. Rail corrugation: characteristics, causes, and treatments. *P I Mech Eng F-J Rai* 223 (2009) 581–596.
- [25] Kalousek J, Johnson KL. An investigation of short pitch wheel and rail corrugations on the Vancouver mass transit system. *P I Mech Eng Part F-J Rai* 206 (1992) 127–135.
- [26] Jin X. Key problems faced in high-speed train operation. *J Zhejiang Univ-Sci A (Appl Phys & Eng)* 15 (2014) 936–945.
- [27] Knothe K, Groß-Thebing A. Short wavelength rail corrugation and non-steady state contact mechanics. *Vehicle Syst Dyn* 46 (2008) 49–66.

### 3 Initial excitation and consistency condition for initiation and growth

---

- [28] Cui X, Chen G, Zhao J, Yan W, Ouyang H, Zhu M. Field investigation and numerical study of the rail corrugation caused by frictional self-excited vibration. *Wear* 376–377 (2017) 1919–1929.
- [29] Meehan PA, Batten RD, Bellette PA. The effect of non-uniform train speed distribution on rail corrugation growth in curves/corners. *Wear* 366–367 (2016) 27–37.
- [30] Sun Y, Simson S. Wagon–track modelling and parametric study on rail corrugation initiation due to wheel stick–slip process on curved track. *Wear* 265 (2008) 1193–1201.
- [31] Hory C, Bouillaut L, Aknin P. Time–frequency characterization of rail corrugation under a combined auto-regressive and matched filter scheme. *Mech Syst Signal Pr* 29 (2012) 174–186.
- [32] Jin X, Wen Z. Effect of discrete track support by sleepers on rail corrugation at a curved track. *J Sound Vib* 315 (2008) 279–300.
- [33] Wu T. Parametric excitation of wheel/track system and its effects on rail corrugation. *Wear* 265 (2008) 1176–1182.
- [34] Tassilly E, Vincent N. Rail corrugations: analytical models and field tests. *Wear* 144 (1991) 163–178.
- [35] Fourie D, Fröhling R, Heyns S. Railhead corrugation resulting from mode-coupling instability in the presence of veering modes. *Tribol Int* 152 (2020) 106499.
- [36] Correa N, Vadillo EG, Santamaria J, Herreros J. A versatile method in the space domain to study short-wave rail undulatory wear caused by rail surface defects. *Wear* 352–353 (2016) 196–208.
- [37] Grassie S. Rail corrugation: advances in measurement, understanding and treatment. *Wear* 258 (2005) 1224–1234.
- [38] Remington P. Wheel/rail noise—Parts IV: Rolling noise. *J Sound Vib* 46 (1976) 419–436.
- [39] Li Z, Dollevoet R, Molodova M, Zhao X. Squat growth—some observations and the validation of numerical predictions. *Wear* 271 (2011) 148–157.
- [40] Deng X, Li Z, Qian Z, Zhai W, Xiao Q, Dollevoet R. Pre-cracking development of weld-induced squats due to plastic deformation. *Int J Fatigue* 127 (2019) 431–444.
- [41] Cui X, Chen G, Yang H, Zhang Q, Ouyang H, Zhu M. Study on rail corrugation of a metro tangential track with Cologne-egg type fasteners. *Vehicle Syst Dyn* 54 (2016) 353–369.
- [42] Ilias H. The influence of railpad stiffness on wheelset/track interaction and corrugation growth. *J Sound Vib* 227 (1999) 935–948.
- [43] Egana J, Vinolas J, Seco M. Investigation of the influence of rail pad stiffness on rail corrugation on a transit system. *Wear* 261 (2006) 216–224.
- [44] Xu J, Wang K, Liang X, Gao Y, Liu Z, Chen R, Wang P, Xu F, Wei K. Influence of viscoelastic mechanical properties of rail pads on wheel and corrugated rail rolling contact at high speeds. *Tribol Int* 151 (2020) 106523.

### 3 Initial excitation and consistency condition for initiation and growth

- [45] Zhao X, Li Z. The solution of frictional wheel-rail rolling contact with a 3D transient finite element model: validation and error analysis. *Wear* 271 (2011) 444–452.
- [46] Yang Z, Deng X, Li Z. Numerical modelling of dynamic frictional rolling contact with an explicit finite element method. *Tribol Int* 129 (2019) 214–231.
- [47] Knothe K, Grassie S. Modelling of railway track and vehicle/track interaction at high frequencies. *Vehicle Syst Dyn* 22 (1993) 209–262.
- [48] Li Z, Zhao X, Esveld C, Dollevoet R, Molodova M. An investigation into the causes of squats—correlation analysis and numerical modelling. *Wear* 265 (2008) 1349–1355.
- [49] Benson D, Hallquist J. A single surface contact algorithm for the post buckling analysis of shell structures. *Comput Methods in Appl Mech Eng* 78 (1990) 141–163.
- [50] Courant R, Friedrichs K, Lewy H. On the partial difference equations of mathematical physics. *Math Ann* 11 (1928) 215–34.
- [51] Wei Z, Li Z, Qian Z, Chen R, Dollevoet R. 3D FE modelling and validation of frictional contact with partial slip in compression-shift-rolling evolution. *Int J Rail Transport* 4 (2015) 20–36.
- [52] Oregui M, Li Z, Dollevoet R. An investigation into the vertical dynamics of tracks with monoblock sleepers with a 3D finite-element model. *P I Mech Eng F-J Rai* 230 (2016) 891–908.
- [53] Molodova M, Li Z, Núñez A, Dollevoet R. Validation of a finite element model for axle box acceleration at squats in the high frequency range. *Comput Struct* 141 (2014) 84–93.
- [54] Grassie SL. Squats and squat-type defects in rails: The understanding to date. *P I Mech Eng F-J Rai* 226 (2012) 235–242.
- [55] Zhao X, Li Z, Dollevoet R. Influence of the fastening modelling on the vehicle-track interaction at singular rail surface defects. *J Comput Nonlinear Dyn* 9 (2014) 031002.
- [56] Nielsen J. Numerical prediction of rail roughness growth on tangent railway tracks. *J Sound Vib* 267 (2003) 537–548.
- [57] Weaver W, Timoshenko S, Young D. *Vibration Problems in Engineering*. Wiley-Interscience, 1990.
- [58] Bian J, Gu Y, Murray MH. A dynamic wheel–rail impact analysis of railway track under wheel flat by finite element analysis. *Veh Syst Dyn* 51 (2013) 784–797.



## **“BROWN ETCHING LAYER”: A POSSIBLE NEW INSIGHT INTO THE CRACK INITIATION OF ROLLING CONTACT FATIGUE IN RAIL STEELS?**

*A field sample of rail steel was metallurgically examined to characterize its rolling contact fatigue (RCF) damage. In addition to the well-known white etching layer (WEL), a possible different type of surface modification layer was identified in parallel. The layer has some similar features as the WEL but exhibits a significantly different etching response to 3 vol% Nital etchant. After etching, the new layer exhibits a brown colour under the same light reflection. This layer was named as “brown etching layer” (BEL) to distinguish it from the WEL. Similar to the WEL, cracks are observed to be closely related to the BEL. The cracks are found to penetrate deeper than those initiated by the WEL reported in existing publications. Further, they are found to propagate downwards without branching, which may eventually cause rail fracture. Although its formation mechanism is not yet clear, WEL has been considered by some authors in the literature as a possible RCF initiation source. It is therefore of critical importance to understand the characteristics of the BEL and its formation mechanism. This may also lead to better understanding of the formation mechanism of WEL. To this end, microstructural features of the BEL were studied using micro-hardness tests, optical microscopy and scanning electron microscopy. The BEL was found to be distinctly softer than the WEL and lamella-type features are found within the BEL. The microstructural features of the BEL were compared with the WEL reported in the literature. Finally, the formation mechanism of the fatigue damage was discussed based on the comparison, observations and material characterization.*

---

This chapter is based on the publication below:

Li S, Wu J, Petrov RH, Li Z, Dollevoet R, Sietsma J. “Brown etching layer”: a possible new insight into the crack initiation of rolling contact fatigue in rail steels? Engineering Failure Analysis 66 (2016) 8–18.

### 4.1 Introduction

After multiple wheel-rail interaction cycles, a type of microstructural alteration called the white etching layer (WEL) usually forms at the surface of the rail, accompanied by severe plastic deformation and an increase in hardness and wear resistance [1–5]. The WEL is so named due to the higher etching resistance to Nital etchant (2 – 10 vol% HNO<sub>3</sub> in ethanol), therein producing a white color under unpolarized optical light reflection. The hardness of the WEL is significantly higher than that of the matrix pearlite microstructure and can be up to 1200 HV [1]. This hard and brittle surface layer has received substantial attention as it is considered by some authors as a possible cause of crack initiation of rolling contact fatigue (RCF) [1, 6, 7] and thus its influence on the service life of rail steels. Therefore, it is necessary to understand the formation mechanism of the WEL and develop corresponding methods for avoiding or mitigating WEL-based damage.

The WEL has been extensively studied by many researchers. Generally, two formation mechanisms are assumed possible for the WEL: 1) high temperature causing a martensitic phase transformation and 2) severe plastic deformation leading to strain-induced cementite dissolution and grain refinement, e.g., nanocrystalline ferrite with carbon supersaturation [8]. The first formation mechanism is generally attributed to the frictional heat generated by wheel/rail contact. When the temperature is sufficiently high to reach the austenitization temperature, followed by rapid cooling, a martensitic structure is formed together with possible retained austenite or undissolved cementite. This assumption was supported by Clayton and Allery [1], who noted that the WEL was produced by a short thermal process. By using the techniques of cross-sectional transmission electron microscopy (XTEM) and synchrotron X-ray diffraction, Österle et al. [2] characterized the WEL in rail steels under a specific loading condition, compared the microstructure and hardness with the WEL produced by laser treatment, and concluded that the WEL consisted of martensite with high dislocation density. Wild et al. [3] analysed corrugated rail materials with multiple experimental facilities, and the WEL at the corrugation crest was identified as martensite of nano-scale grain size containing cementite particles. Research by Wang et al. [4] detected retained austenite via X-ray diffraction (XRD) and further confirmed the martensitic nature of the WEL. Takahashi et al. [5] analyzed the WEL with atom probe tomography and found that lamella thinning had not occurred in the WEL near the surface; in addition, they concluded that the WEL region did not undergo severe plastic deformation. Together with the prediction of the increased temperature via frictional heat, possibly to temperatures above the austenitization temperature and the shape analysis of manganese-enriched zones, they concluded that the WEL was formed by martensitic transformation.

The second explanation for the WEL concerns severe plastic deformation. Plastic deformation can cause cementite lamella alignment to the shear plane, fragmentation, and reduction in interlamellar spacing [9]. Under severe deformation conditions, this process facilitates the dissolution of cementite and promotes grain refinement [10, 11]. The formation of the WEL is thus explained as a nanocrystalline microstructure mainly consisting of ferrite, together with not fully dissolved cementite in the form of fragmented lamellae or particles. Feller and Walf's research [12] revealed that the WEL formed in the rail is not martensite; rather, it is produced through the breaking of cementite into fine dispersed particles. The results obtained by Newcomb and Stobbs [13] using transmission electron microscopy (TEM) and transient temperature estimation indicated that the WEL is a severely deformed ferrite in which cementite is dissolved, in analogy to mechanical alloying that is well known as a low temperature process [14]. Based on investigations of the microstructure of the WEL using TEM and X-ray diffraction and on discussions of the nanostructure formation mechanism, Lojkowski et al. [10] concluded that the WEL is a nanocrystalline ferrite produced by cyclic heavy plastic deformation far below the austenitization temperature. Baumann et al. [11] investigated the WEL in corrugated rails and observed the WEL at corrugation crests, with a hardness of 1000 HV to 1200 HV. TEM analysis revealed a nanocrystalline structure with a grain size of less than 50 nm. Based on these observations, they claimed that WEL formation due to a temperature increase alone does not seem possible and indicated the possibility of the dissolution of cementite due to severe plastic deformation [11].

A recent work by Zhang et al. [15] indicated that the WEL is composed of deformed cementite lamellae as well as nanocrystalline martensite, austenite and cementite. Thus, the formation mechanisms of the WEL are complex. There is no single mechanism that can explain all WEL phenomena, i.e., under certain conditions, one mechanism might be dominant, whereas under other conditions, both mechanisms may be responsible [2]. As an alternative, a complete explanation of the WEL under a specific condition seems more feasible and realistic.

Our original intention was to investigate the damage of rail materials in the presence of corrugation. Similar to previous research [4, 12], the WEL, as a type of rail surface damage, was observed using optical microscopy (OM). In addition to the WEL, a possible new type of microstructurally altered layer was recognized in the current investigation. The new layer appears as brown (rather than white, as is the case for the WEL) or as mixed white/brown colors after exposure to the same Nital etchant (see Fig. 4.3). Because it exhibits similar features as the WEL, such as distinct interfaces with the bulk material and the isolated or continuous distribution of "islands", this new type of layer was denoted as the brown



## 4 Brown etching layer

etching layer (BEL) in analogue with the WEL. To the authors' knowledge, the BEL has yet to receive substantial attention despite having been reported in [10, 16, 17]. Note that on the one hand the observation of BELs in the aforementioned publications and in the present paper, with differences in traffic conditions, e.g. train speed and annual axle load, indicates that the occurrence of the BEL is not related to a specific traffic condition. On the other hand, there is insufficient evidence in the existing publications to correlate the BEL to a specific rail material. Compared to the previous reported BEL, the observed BEL in the present paper has shown different features that will be elaborated in subsequent sections. In addition to the microstructural morphology, the mechanical characteristics of the BEL, measured by a micro-hardness test, is also shown to be different from that of the well-known WEL. Considering that the mechanism for WEL formation is as of yet unknown, the discovery of the BEL arouses the authors' interest in determining the following: could an investigation of the BEL provide a possible better insight into the formation of the WEL? Moreover, cracks caused by the WEL usually grow with shallow angles with respect to the rail surface and eventually cause surface spalling [1, 18]. However, a crack formed in front of the BEL and near the BEL and Int-1 has been found to grow considerably deeper into the less deformed or undeformed material, and the orientation of the crack tip is downwards without branching, which may produce rail fracturing at a certain stage. Therefore, the study of the formation mechanism of the BEL is of practical concern and importance. In this research, the microstructural features of the BEL are characterized using optical microscopy, micro-hardness tests, and scanning electron microscopy. This study is expected to provide an understanding of 1) the microstructural features and mechanical properties of the BEL, 2) correlations between the WEL and the BEL, and 3) the possible formation mechanism of the BEL.

## 4.2 Sample description and experimental details

### 4.2.1 Sample

The rail in this investigation was removed from a straight track in the Dutch railway network between Meppel and Leeuwarden. The track is a mainly passenger line, with a highest operating speed of 140 km/h. The line on average carried approximately 10,000 tons of loads per day. Based on the image of the rail surface in Fig. 4.1, the period from the last grinding maintenance was estimated to have been more than 1 year. Therefore, the total tonnage is greater than 3.65 MGT. The steel is a UIC 54 standard rail. It is pearlite with a grade of R260Mn, equivalent to the German grade 900 A, which means that the tensile

strength of the rail material is approximately 900 MPa. The nominal chemical composition of the rail material is listed in Table 4.1 [19].

**Table 4.1.** Nominal chemical composition of the rail steel

Rail grade	Chemical compositions in wt.%				
	C	Si	Mn	Pmax	Smax
R260Mn	0.55–0.75	0.15–0.60	1.30–1.70	0.025	0.025

The corrugation waves are shown in Fig. 4.1. The wave patterns are identified by shiny peaks and dark valleys. The severity of the corrugation patterns changes in the traffic direction, decaying when passing over the sleeper support.

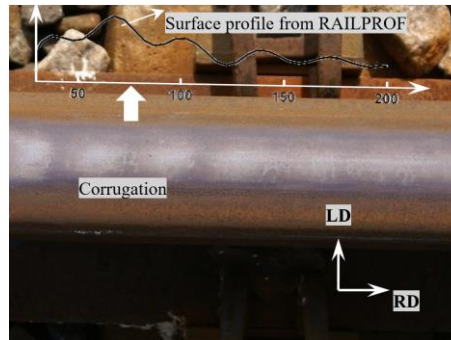


**Fig. 4.1.** Corrugation wave patterns, photo taken in June, 2007 (RD: traffic direction, LD: lateral direction to the field side)

The metallurgical investigations were performed 7 years after the material was removed from the track in June 2007. Due to the long period of exposure to air, the rail surface was corroded. The bright peaks and dark valleys of the corrugation could not be visually identified. However, using the RAILPROF measurement device, the wave patterns can be still recognized. For convenience, these wave patterns are shown on the rail as a line (see Fig. 4.1). The corresponding wave locations are indicated by the left indents from the rail clips. RAILPROF measures the longitudinal-vertical profile of the rail crown center for a UIC 54 type of rail. The subsequently analyzed rail sections (see Fig. 4.2) with the BEL are identified as being at the corrugation crest.

## 4 Brown etching layer

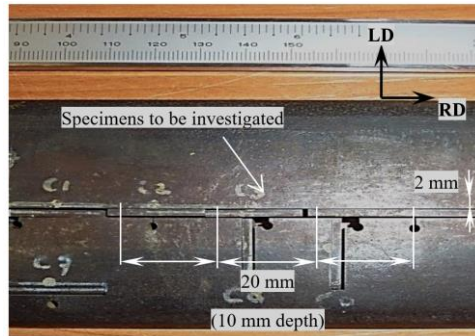


Fig. 4.2. Top view of the rail sectioning scheme

### 4.2.2 Specimen preparation and experimental tools

To investigate the influence of wheel–rail contact on the rail mechanical properties and microstructure, longitudinal-vertical rail specimens with dimensions of 20 mm × 2 mm × 10 mm in the longitudinal, lateral and vertical directions, respectively, were designed (see Fig. 4.2). The specimens were prepared with a standard metallurgical procedure, i.e., sectioned, embedded, polished and etched in 3 vol% solution of HNO<sub>3</sub> in ethanol (Nital).

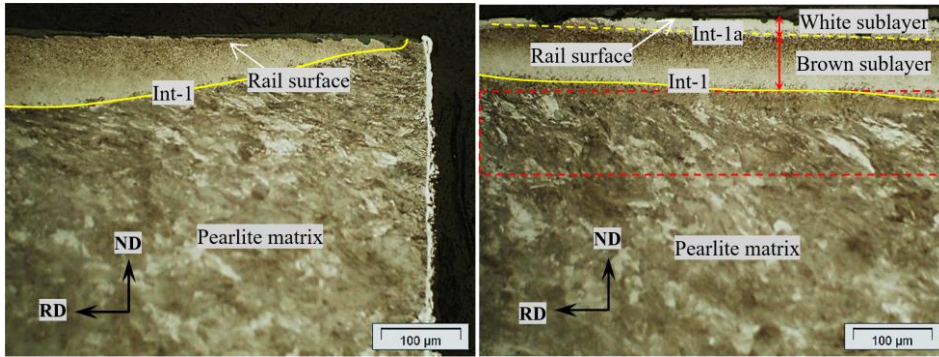
Due to the finite contact patch size, high levels of stress and frictional heat develop between the wheel and the rail, which results in temperature rise, surface shear deformation, wear, and micro cracks together with structural transformation. These features can be significant in the study of the damage process characterizing wear and RCF. To this end, the microstructure morphology of the specimens was investigated with an Olympus BH-2 optical microscope and a JSM 6500F scanning electron microscope with field emission gun (FEG-SEM). Moreover, micro-hardness tests were performed using a Durascan 70 (Struers), with a load of 1 N and a loading duration of 10 s, to quantify the mechanical properties of the BEL. The hardness distribution along the depth within the BEL was measured. At each depth, a minimum of 4 indentations was made.

## 4.3 Experimental results

### 4.3.1 Microstructural features of the BEL in OM

Figs. 4.3a and 4.3b shows two examples of BEL. They are from the same specimen and from the same BEL. Due to the fact that the studied BEL is quite long (~5 mm) they are not shown

in the same figure but separately. Fig. 4.3a is taken at the edge of the BEL, while Fig. 4.3b is in the middle of the BEL.



(a) nearly single-layer BEL

(b) mixed sublayers of the BEL

**Fig. 4.3.** Microstructural features of the BEL made visible via optical microscopy, etched by 3 vol% Nital (ND: rail normal direction; Int-1: BEL and pearlite matrix interface, Int-1a: white and brown sublayers interface)

It is noted that the BEL does not have a uniform structure. Fig. 4.3a shows a situation with a nearly single-layer BEL, whereas the BEL in Fig. 4.3b consists of white and brown colored regions.

In order to be differentiated from the well-known WEL, the whole layer shown to be either fully brown in Fig. 4.3a or a mixture of white and brown in Fig. 4.3b, is defined as the same term of the BEL throughout the paper. Similar to the WEL, the BEL is separated from the pearlite matrix by a distinct interface called “Int-1” (see the solid lines in Fig. 4.3). For the BEL consisting of mixed white and brown sub-units (see Fig. 4.3b), the region above the interface “Int-1a” (see the dash line in Fig. 4.3b) is called “white sublayer”, and the region between Int-1 and Int-1a is considered as “brown sublayer”.

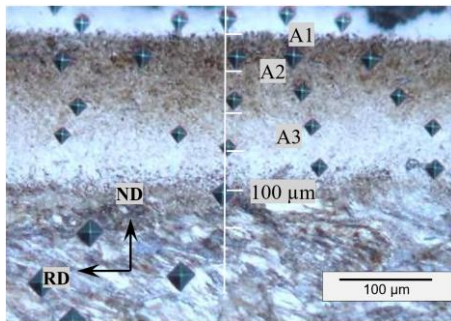
Note that the contrast within the brown sublayer in Fig. 4.3b is non-uniform and appears to vary with depth from deep brown just below Int-1a to white when it is close to Int-1. However, this brown sublayer will not be further divided into different sublayers due to: 1) The contrast in this sublayer is gradually changing without observable distinct interfaces; 2) As will be shown later, the SEM images show the similar microstructural features throughout the defined brown sublayer, which differ from the ones of the white sublayer. Consequently, it is reasonable to classify the region between Int-1a and Int-1 uniformly being “brown sublayer”.

## 4 Brown etching layer

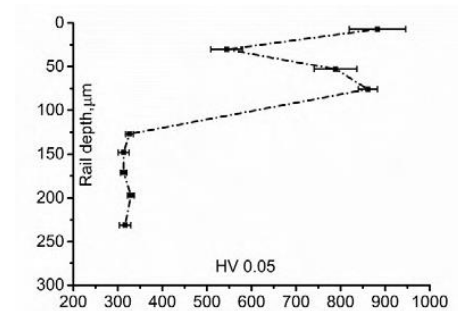
A plastic deformation influenced zone (within the rectangle area) with the observable material flow towards the traffic direction can be observed immediately beneath the BEL. Moreover, distributed break-offs at the rail surface, which can form due to spalling of the white sublayer from the surface, are noted.

### 4.3.2 Micro-hardness test

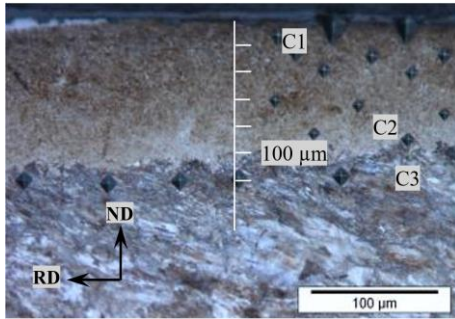
Figs. 4.4a–d shows the features of the BEL and the corresponding hardness profiles along the depth. In Figs. 4.4a and 4.4b, the topmost whitest layer is shown to have the highest hardness. The hardness of this sublayer (see Fig. 4.4b) is on average  $882.7 \pm 63.3$  HV. An abrupt decrease in the hardness to  $542.6 \pm 26.4$  HV is observed when crossing Int-1a at a depth of  $\sim 30$   $\mu\text{m}$  below the rail surface. The hardness within the etched brown sublayers increases up to  $840.6 \pm 32.9$  HV at Int-1. The low hardness of approx. 300 HV is found in the matrix.



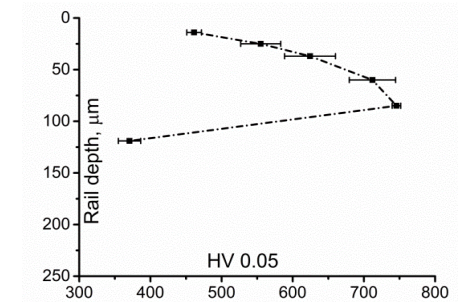
(a) BEL consisting of mixed sublayers



(b) Hardness distribution along the depth



(c) Nearly single-layer BEL



(d) Hardness distribution along the depth

**Fig. 4.4.** Optical micrographs of the specimen for the micro-hardness test and micro-hardness distributions as a function of depth

A nearly single-layer BEL is shown in Fig. 4.4c (left top corner with a minor white sublayer). The micro-hardness profile in Fig. 4.4d reveals a strongly varying hardness distribution

within the BEL. The topmost layer is the softest, with a hardness as low as 450 – 470 HV. The highest hardness within the BEL appears near Int-1, which is approximately 80  $\mu\text{m}$  from the rail surface. Hardness within this sub-region varies in the range of 740 – 752 HV, with an average hardness of 746 HV.

Further, note that the micro-hardness distributions of the brown sublayer (between 30 and 125  $\mu\text{m}$ ) in Fig. 4.4b and the near single brown layer in Fig. 4.4d are similar. A1 to A3 and C1 to C3 refer to the locations where the subsequent SEM observations were conducted.

### 4.3.3 Microstructural features of BEL in SEM

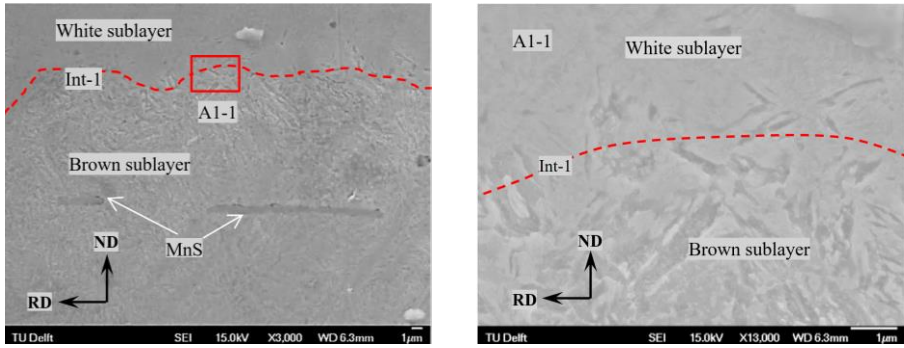
Microstructural differences of different sublayers within the BEL are further characterized in higher magnification using SEM. BELs consisting of a near single brown sublayer and mixed sublayers are both examined. The features in SEM are taken in areas close to the hardness test indents, e.g. A1–A3 in Fig. 4.4a, for the consideration of easy positioning. SEM micrographs will help to reveal the microstructural features contributing to the difference in the hardness or the mechanism of crack development.

#### 4.3.3.1 Mixed layers of white and brown sublayers

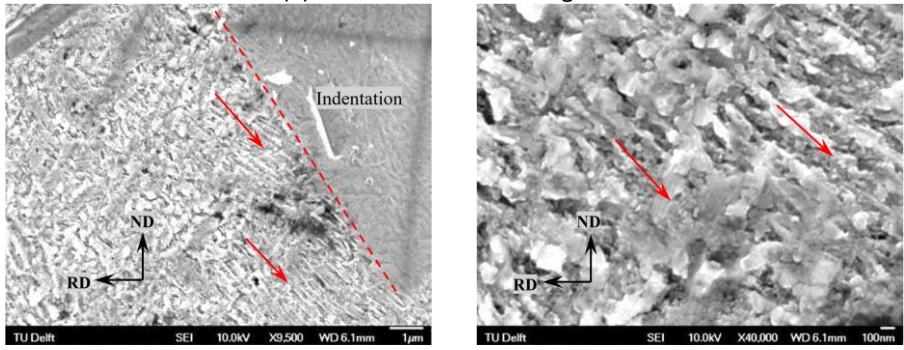
Fig. 4.5a shows the region of the BEL around Int-1a. The topmost white sublayer is less influenced by the etching, shown with a smoother morphology compared with the brown sublayer below the interface. Features of distributed “gullies” in the brown sublayer can be distinctly recognized beneath the interface. Lamella-type microstructural features can be observed within the brown zone. Two elongated MnS inclusions parallel to the traffic direction are indicated by arrows. A lamella-type structure can also be observed in the brown sublayer, as shown in Figs. 4.5b and 4.5c. The depth of zone A3 (see Fig. 4.4a) is in the range of 60–70  $\mu\text{m}$  below the surface, which is near the second micro-hardness peak in the brown sublayer (see Fig. 4.4b). The feature of this layer is the lamella-type structures parallel to the traffic direction. However, there is no definite conclusion as to whether this orientation is determined by the stress/strain state or the initial angle of the pearlite colonies.



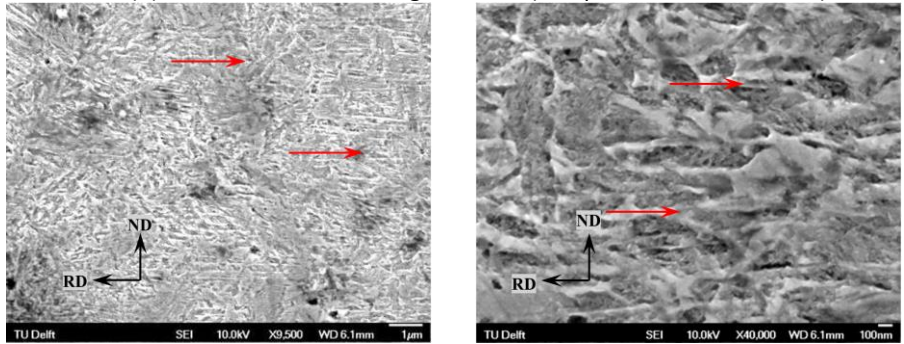
## 4 Brown etching layer



(a) Zone A1 and local magnification



(b) Zone A2 and local magnification (~30 µm below the surface)



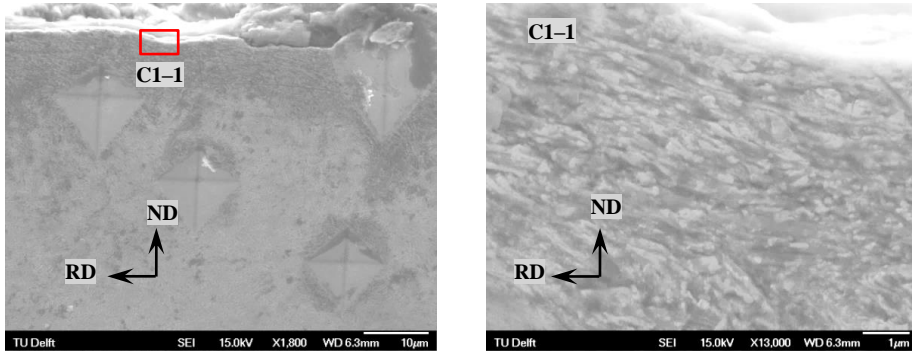
(c) Zone A3 and local magnification (~65 µm below the surface)

**Fig. 4.5.** SEM micrographs of the BEL at different depths as marked in Fig. 4.4a (red arrows indicate the orientation of the lamella-type structure)

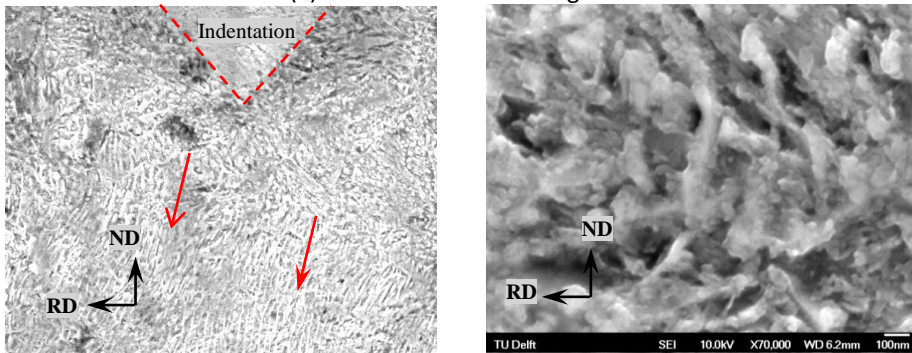
### 4.3.3.2 Nearly single-layer BEL

Figs. 4.6a–c shows the SEM micrographs of the nearly single-layer BEL. These figures correspond to the positions denoted as C1, C2, and C3 in Fig. 4.4c. Fig. 4.6a shows the microstructures near the top surface (at a depth of ~10 µm from the surface) in area C1.

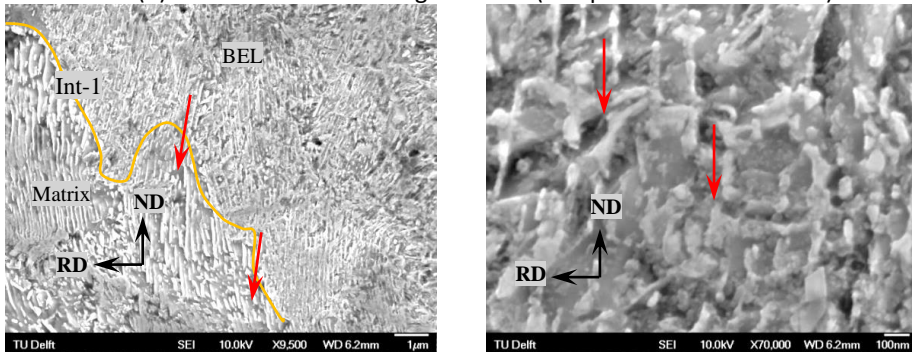
This region presents floccus features and is flattened in the traffic direction. Note that the lamella-type structure is distinct in the lower part of Fig. 4.6b. Fig. 4.6c, near zone C3, shows Int-1 (solid line in yellow) between the BEL and the pearlite matrix. Continuation of the lamellae from the matrix into the BEL can be seen, as is indicated by the arrows across the interface Int-1.



(a) Zone C1 and local magnification



(b) Zone C2 and local magnification (~60 µm below the surface)



(c) Zone C3 and local magnification (~100 µm below the surface)

**Fig. 4.6.** SEM micrographs of a nearly single-layer BEL at different depths as marked in Fig. 4.4c (red arrows indicate the orientation of the lamella-type structure)

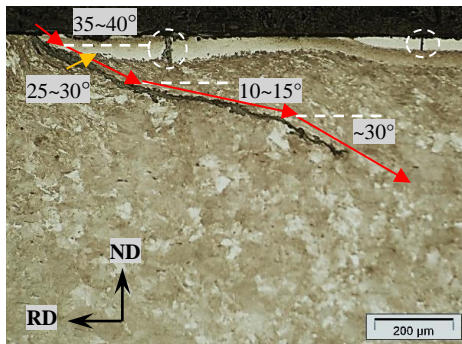


## 4 Brown etching layer

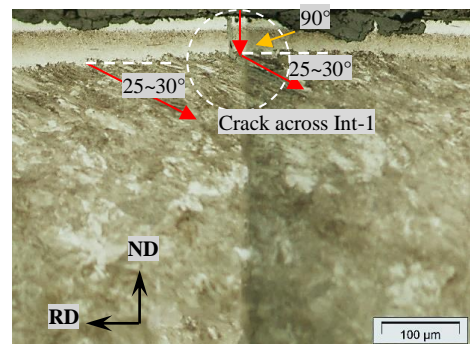
### 4.3.4 BEL and cracks

Fig. 4.7 shows different types of cracks related to the BEL. There are three obvious cracks in Fig. 4.7a, one of which forms at the leading edge of the BEL and grows to a depth of more than 300  $\mu\text{m}$  (indicated by red arrows). The crack angle is measured with respect to the traffic direction. The angles of the crack curve vary with the propagation depth. Specifically, the curve near the uppermost surface takes on an angle of  $35\text{--}40^\circ$ , decreases to  $25\text{--}30^\circ$  and further to  $10\text{--}15^\circ$ , and finally increases to  $30^\circ$ . The direction of the growth in the curve is opposite to the traffic direction. In contrast to previous findings that cracks caused by the WEL mostly propagate at a limited depth only or cause spalling, the observed crack formed as a result of the BEL propagates deeper into the bulk material and exhibits a continuous downwards growing trend. This phenomenon indicates that, compared to the cracks formed due to the WEL, the BEL seems to have a higher probability of producing rail fracturing.

Two other cracks (circled in Fig. 4.7a) were within the BEL zone and had not yet propagated into the bulk material. They are almost perpendicular to the traffic direction, indicating the brittle nature of the BEL. Fig. 4.7b presents another case of such cracks that had penetrated through Int-1 and developed into the bulk material. Similar to the one in Fig. 4.7a, the crack in the BEL is almost vertical to the traffic direction. At Int-1, it changed its course to an angle of  $25\text{--}30^\circ$  opposite to the traffic direction, therein following the direction of the material flow. This indicates a clear difference in the material properties at the sharp interface with the bulk material. Note that there is a clear border in the middle of Fig. 4.7b. This border has no physical meaning aside from the image splicing of two micrographs into one.



(a) Cracks in the BEL and near Int-1



(b) Crack penetration across Int-1

**Fig. 4.7.** Cracks at different locations with respect to the BEL (The contrast change in the center of Fig. 4.7b is due to the splicing of two micrographs)

## 4.4 Discussion

Based on the current experimental investigations, the presented BEL is found to have the following features:

- 1) The BEL consists of “white and brown” sublayers (Figs. 4.3 and 4.4), in contrast to the single uniform white layer in the WEL.
- 2) The hardness of the “white sublayer” is comparable to that of the WEL in [3,15,20], whereas the “brown” sublayer is much softer. The minimum measured hardness of the “brown” sublayer is 450 HV in Fig. 4.4d in this study, whereas the hardness of the WEL is rarely below 700 HV [3,15]. This indicates the possible different microstructures of the two types of layers.
- 3) The SEM observation of the brown sublayer reveals significant lamella-type microstructural morphology. Note that in Fig. 4.6c there is a continuation of the lamellae from the bulk material into the BEL. This continuation of the lamellae may facilitate crack propagation across Int-1 and into the bulk material due to the lower resistance [21], instead of propagation along the interface (see Fig. 4.7b).
- 4) The observation of floccus and flattened morphology towards the traffic direction in the topmost ~10  $\mu\text{m}$  thick region of the nearly single-layer BEL, indicates a considerable plastic deformation history of the rail material (see Fig. 4.6a).
- 5) The crack in the BEL specimen penetrates deeper than reported in the WEL (see Fig. 4.7a).
- 6) The crack develops downwards without branching, in comparison to cracks formed in the WEL finally lead to the spalling [10] (Fig. 4.7a).

To better understand the BEL, its microstructural features are compared to those of the WEL reported in existing publication. In [15], pearlite-like features appear in the WEL region nearby the transition zone, and were reported as deformed pearlitic lamellae with a smaller lamellar spacing of 30–40 nm. Moreover, the authors assumed that the nanocrystallization and austenitization were caused by repeated plastic deformation rather than the instantaneous temperature increase. In a martensitic microstructure from (ultra)fast heat treatment from a pearlite type microstructure [22], the traces of the original cementite remain observable, indicating the partial dissolution/transformation of cementite. Similarly, a lamella-type structure also appears in the studied brown sublayer; however, this feature seems to be absent in the white sublayer in this paper (see Fig. 4.5a).

In Fig. 4.4b, there is an abrupt decrease in the hardness below Int-1a. As shown in the previous section, the hardness of the white sublayer is comparable to that of the WEL in the literature, whereas obvious softening is observed in the brown sublayer, with the minimum

## 4 Brown etching layer

---

hardness close to Int-1a. A similar morphology and hardness pattern is reported, and the brown etching layer between the white sublayer (expressed as the WEL in the original paper) and the bulk material was explained as a transition zone [20]. The hardness in the transition zone is unlikely to be a feature caused by pure plastic deformation because the layers nearer to the white sublayer are expected to be harder than areas close to Int-1, considering the difference in work hardening and grain refinement. This is in stark contrast to the current observation.

Instead, the sudden decrease in the hardness at Int-1a and the later increase towards Int-1 can be explained by the changes in martensite due to annealing at increasing temperatures. It would be reasonable to assume that the entire BEL consists of martensite, as is the case with the martensite WEL in literature, due to the similar morphology and comparable hardness in the white sublayer of the BEL with the WEL. A significant temperature increase at the rail surface must occur for this assumed mechanism, and the temperature is expected to decrease from the rail surface downwards into the rail. The hardness difference in the white and brown sublayers can then be readily explained by the effect of softening in the martensite and the repeated martensite–austenite–martensite phase transformation cycles. According to this assumption, Int-1a can correspond to the zone that is heated to the lower critical temperature for austenite to occur, namely, the Ac1 temperature. Consequently, the martensite zones above Int-1a are reheated to form austenite during passage of a train and transform into martensite during subsequent cooling. The martensite zone below Int-1a will not transform into austenite, while it will be tempered due to the high temperature. As a result, martensite close to Int-1a will be tempered to the greatest extent and consequently become the softest. Admittedly, the potential of the nanocrystalline ferrite nature of the WEL/BEL cannot be excluded because the nanocrystalline ferrite can be expected to undergo softening due to grain growth during annealing at approximately 400 °C [23–25]. The strengthening/softening of the material may also be related to the stress state together with the generated frictional heat.

Moreover, note that indications of plastic deformation have also been recognized in the studied rail piece. The alignment of the lamella-type features towards the train traffic direction in the nearly single brown layer in Figs. 4.6a and 4.6b and the material flow in the pearlite beneath the entire BEL, e.g., Fig. 4.7b, exhibit features of plastic deformation. The BEL is thus very likely a product of combined plastic deformation and phase transformation. However, due to the limitation of the experimental methods and the absence of a reliable thermal–mechanical analysis, the nature of the BEL and its root causes could not be unambiguously identified.

From the comparison and observations, both processes, i.e., repeated plastic deformation and temperature increase, can produce the observed BEL microstructural features. Assumptions have to be made based on the mechanical properties and microstructural features of the BEL from this paper in comparison with those in existing research on WEL.

First, evidence concerning the temperature rise is required to support the assumption that the BEL and the WEL are martensite, because martensite forms from austenite, and austenite can only be produced at high temperature. Under high hydrostatic pressure, the austenitization temperature will decrease. However, the temperature will not decrease below 500 °C [26], which means that if the WEL contains the martensitic structure, the instant temperature within the contact should reach at least 500 °C. The wheel/rail contact temperature cannot be reliably measured; however, it is usually estimated via analytical or numerical calculations [27, 28]. According to [11, 27], the temperature increase at the wheel/rail contact can be expressed by

$$T_{\max} = T_0 + \frac{2}{\sqrt{\pi}} \sqrt{\frac{2\alpha\kappa}{v}} \frac{\delta\mu v_s P}{\lambda} \quad (4.1)$$

where  $T_{\max}$  is the maximum temperature;  $T_0$  is the ambient temperature, 20 °C;  $a$  is the semi-axis, i.e., half of the longitudinal axis of the elliptic contact patch;  $\kappa$  is the thermal diffusivity,  $9.1 \times 10^{-6}$  m<sup>2</sup>/s [27];  $v$  is the wheel rolling speed, 140 km/h (for Dutch passenger train);  $\delta$  is the heat partitioning factor, which represents the heat flowing into the rail,  $\delta = 0.5$  [27];  $\mu$  is the frictional coefficient, 0.05–0.6 [27];  $v_s$  is the sliding velocity, in m/s;  $P$  is the normal maximum pressure, in MPa; and  $\lambda$  is the thermal conductivity, 41 W/m·K [27].

Assuming a static axle load of 120 kN for a Dutch passenger coach in the loaded condition, the maximum pressure based on Hertzian contact theory is 1.31 GPa with  $a = 7.59$  mm. However, when considering the dynamics, the dynamic load will be much larger, assumed to be twice the static load, as shown in [29], where the dynamic load is induced by a mature squat that is smaller than 2 times the static load. Then, the maximum pressure will be 1.66 GPa with  $a = 9.56$  mm. Thus, to assure a temperature increase to 500 °C, the lowest sliding velocity between the wheel/rail with  $\mu = 0.6$  (dry friction) should be 0.524 m/s according to Eq. (1).

It should be emphasized that Hertzian contact theory is built upon the half space assumption. When addressing short track irregularities, e.g., short pitch corrugation, this theory is insufficient for providing reliable results [30]. Therefore, a new modelling approach that should be suitable for solving the non-Hertzian and non-steady-state wheel-rail frictional contact must be employed to investigate this problem. The model developed

## 4 Brown etching layer

---

by Li and his colleagues [29, 31] has been successfully used to find the root causes of squats. A comparison study with Kalker's CONTACT validates the normal and tangential solutions [31]. A further correlation study [29] indicates its reliability up to 2000 Hz. The transient tangential stresses and micro-slip are expected to be simulated using this model; moreover, frictional heat can be quantified.

Second, in addition to the assumption that a martensitic phase transformation occurs due to the high temperature, increasingly more research indicates the possibility of a nanocrystalline microstructure nature of the WEL [10, 13]. This nanostructure can be formed at temperatures far below the austenitization temperature. The assumption is built upon the theory that under cyclic high plastic deformation, the nanostructured Fe-C alloy is formed during the process of grain size refinement [10] and dissolution of cementite [32] due to the high density of dislocations and grain boundaries or grain size refinement [10], together with the temperature increase generated by frictional heat resulting from wheel–rail contact. Therefore, an appropriate numerical tool must be used to calculate the stresses/strains, and estimate the contribution under this assumption. The model of [29, 31] may represent such an option.

Further, it deserves to mention that the rail material is sheared in the traffic direction (see Fig. 4.7). This is in contrast to many other field observations that the rail material flows against traffic direction. When the rail material is sheared against traffic direction, the cracks can grow in the direction of the traffic due to liquid entrapment. This is believed to be the major development mechanism of head checks [33]. Head checks mainly occur at gage corner and gage shoulder in curved tracks due to the quasi-static contact force. In the present study the cracks are related to the dynamic contact force at corrugation. The location is in the middle of the rail crown in straight tracks. Thus the loading condition is different and the resulting rolling contact fatigue is not head checks but usually squats [33, 34]. For the development of corrugation and squats, liquid entrapment is not necessary. The same phenomenon was reported by Clayton and Allery in a metallographic study of short pitch corrugated rails from British rail network [1]. They observed that the corrugation “peaks were sheared to a maximum depth of about 0.25 mm in the direction of traffic (in the opposite direction to that observed in most rails)”. However, no correlation of the near surface plastic flow in corrugation to the traffic direction has been done. It is interesting to investigate in future research how the dynamic wheel–rail contact at corrugation results in the plastic flow in the traffic direction and how cracks subsequently initiate and grow without liquid entrapment.

Information about the nature of the BEL and its connection with the well-known WEL remains insufficient for drawing a clear conclusion from the present study. Could it be that

the BEL is a transitional state from the pearlite structure to the WEL, does it form after the WEL, or is it a different layer formed under certain thermal–mechanical conditions? A detailed understanding of the stresses, the strains and their rate of changes as well as their dependency on contact heat should be sought; thus, further research is necessary.

### 4.5 Summary

A metallurgical study was performed to analyse the rolling contact fatigue damage of a rail sample. Besides the well-known white etching layer (WEL), an extra layer with distinctly lower hardness and a different color is identified. Due to its brown color, this layer was given the name of brown etching layer (BEL) to distinguish it from WEL. Compared to WEL, the cracks formed in the BEL propagate downwards deeper without branching. As a result, the BEL is considered to be more potential to cause rolling contact fatigue. Therefore, this paper characterizes the microstructural features of the BEL and analyses its formation mechanism.

The BEL was found to consist of either mixed white/brown etched sublayers or a nearly single-layer BEL. Micro-hardness tests show that the hardness of the white sublayer is comparable with that of the WEL in the literature, whereas the brown sublayer is softer than the white zones. There is an abrupt hardness decrease in the brown sublayer near Int-1a (the white and brown sublayers' interface), and the highest hardness in the brown etched sublayer appears near Int-1 (the BEL and pearlite matrix interface). The observed lamella-type morphology over the characterized brown sublayer and the hardness distribution over the entire BEL can be interpreted based on the hypothesis of a (fast) martensite phase transformation due to the increased temperature caused by passing trains. The observation of flattened floccus feature in the nearly single-layer BEL in the topmost rail surface region and the material flow in the pearlite beneath the entire BEL indicate the possible contribution of plastic deformation to the formation of the BEL. Further, the observation that the cracks in the BEL were found to penetrate deeper than those in WEL and propagate downwards without branching can be explained by the closer hardness and more similar microstructure features between the BEL and the bulk material matrix than between the WEL and the bulk material.

The BEL is considered to be brittle due to the observation of cracks that are vertical to the traffic direction within the BEL zones. A similar observation of cracking inside the WEL indicates some possible similar natures of the BEL and the WEL.

## 4 Brown etching layer

---

It is, however, not known from the present work whether the BEL is a transitional state from the pearlite structure to the WEL, if it forms after the WEL, or if it is a different layer formed under certain thermal–mechanical conditions. To clarify the formation mechanism of the BEL and its relation with the WEL and loading conditions, further research with additional experimental examination and numerical analysis is necessary.

## References

- [1] Clayton P, Allery MBP. Metallurgical aspects of surface damage problems in rails. *Can Metall* 1982;21(1):31–46.
- [2] Österle W, Rooch H, Pyzalla A, Wang L. Investigation of white etching layers on rails by optical microscopy, electron microscopy, X-ray and synchrotron X-ray diffraction. *Mater Sci Eng A* 2001;303(1–2):150–57.
- [3] Wild E, Wang L, Hasse B, Wroblewski T, Goerigk G, Pyzalla A. Microstructure alterations at the surface of a heavily corrugated rail with strong ripple formation. *Wear* 2003;254(9):876–83.
- [4] Wang L, Pyzalla A, Stadlbauer W, Werner EA. Microstructure features on rolling surfaces of railway rails subjected to heavy loading. *Mater Sci Eng A* 2003;359(1–2):31–43.
- [5] Takahashi J, Kawakami K, Ueda M. Atom probe tomography analysis of the white etching layer in a rail track surface. *Acta Mater* 2010;58(10):3602–12.
- [6] Sarvesh P, William JTD, Mohammadali F. Early stages of rail squat formation and the role of a white etching layer. *Int J Fatigue* 2013;52:144–56.
- [7] Sarvesh P, William JTD, Carlos HGV. Andrew Wilson, Andrej Atrens, Surface damage on new AS60 rail caused by wheel slip. *Eng Fail Anal* 2012;22:152–65.
- [8] Hono K, Ohnuma M, Murayama M, Nishida S, Yoshie A, Takahashi T. Cementite decomposition in heavily drawn pearlite steel wire. *Scripta Mater* 2001;44(6):977–83.
- [9] Wetscher F, Vorhauer A, Stock R, Pippan R. Structural refinement of low alloyed steels during severe plastic deformation. *Mater Sci Eng A* 2004;387:809–16.
- [10] Lojkowski W, Djahanbakhsh M, Bürkle G, Gierlotka S, Zielinski W, Fecht H.-J. Nanostructure formation on the surface of railway tracks. *Mater Sci Eng A* 2001;303(1–2):197–208.
- [11] Baumann G, Fecht HJ, Liebelt S. Formation of white-etching layers on rail treads. *Wear* 1996;191(1–2):133–40.
- [12] Feller HG, Walf K. Surface analysis of corrugated rail treads. *Wear* 1991;144(1–2):153–61.

- [13] Newcomb SB, Stobbs WM. A transmission Electron microscopy study of the White-etching layer on a Rail Head. *Mater Sci Eng* 1984;66(2):195–204.
- [14] Murty BS, Ranganathan S. Novel materials synthesis by mechanical alloying/milling. *Int Mater Rev* 1998;43(3):101–41.
- [15] Zhang HW, Ohsaki S, Mitao S, Ohnuma M, Hono K. Microstructural investigation of white etching layer on pearlite steel rail. *Mater Sci Eng A* 2006;421(1–2):191–9.
- [16] Wang L. Microstructure and residual stress state in the contact zone of rails and wheels. MSc Thesis, Berlin: Der Technischen Universitat Berlin; 2002, p. 95.
- [17] Steenbergen M, Dollevoet R. On the mechanism of squat formation on train rails—part I: Origination. *Int J Fatigue* 2013;47:361–72.
- [18] Carroll RI, Beynon JH. Rolling contact fatigue of white etching layer: part 1 crack morphology. *Wear* 2007;262(9–10):1253–1266.
- [19] Esveld C. Modern railway track. 2nd ed. Zaltbommel: MRT-productions; 2001, Available: [www.esveld.com](http://www.esveld.com).
- [20] Seo J, Kwon S, Jun H, Lee D. Numerical stress analysis and rolling contact fatigue of White etching layer on rail steel. *Int J Fatigue* 2011;33(2):203–11.
- [21] Wetscher F, Stock R, Pippan R. Changes in the mechanical properties of a pearlitic steel due to large shear deformation. *Mater Sci Eng A* 2007;445–446:237–43.
- [22] Samuels LE. Light microscopy of carbon steels. Materials Park, OH: ASM International; 1999.
- [23] Xu Y, Liu ZG, Umemoto M, Tsuchiya K. Formation and annealing behavior of nanocrystalline ferrite in Fe-0.89C spheroidite steel produced by ball milling. *Metall Mater Transactions A* 2002;33(7):2195–203.
- [24] Meyers MA, Mishra A, Benson DJ. Mechanical properties of nanocrystalline materials. *Prog Mater Sci* 2006;51(4):427–556.
- [25] Ohsaki S, Hono K, Hidaka H, Takaki S. Characterization of nanocrystalline ferrite produced by mechanical milling of pearlitic steel. *Scripta Mater* 2005;52(4):271–6.
- [26] Blackburn LD, Kaufman L, Cohen M. Phase transformations in iron-ruthenium alloys under high pressure. *Acta. Metall* 1965;13(5):533–41.
- [27] Knothe K, Liebelt S. Determination of temperatures for sliding contact with applications for wheel-rail systems. *Wear* 1995;189(1–2):91–9.
- [28] Ertz M, Knothe K. A comparison of analytical and numerical methods for the calculation of temperatures in wheel/rail contact. *Wear* 2002;253(3–4):498–508.
- [29] Li Z, Zhao X, Esveld C, Dollevoet R, Molodova M. An investigation into the causes of squats—correlation analysis and numerical modelling. *Wear* 2008;265(9–10):1349–55.
- [30] Neilsen JB. Evolution of rail corrugation predicted with a non-linear wear model. *J Sound Vibration* 1999;227(5):915–33.



#### 4 Brown etching layer

---

[31] Zhao X, Li Z. The solution of frictional wheel–rail rolling contact with a 3D transient finite element model: Validation and error analysis. *Wear* 2011;271(1–2):444–52.

[32] Ivanisenko Y, Sauvage X, MacLaren I, Fecht H. -J. Nanostructuring and dissolution of cementite in pearlitic steels during severe plastic deformation. *Nanoscale Phenomena* 2009;2:41–55.

# 5

## CONCLUSIONS, APPLICATIONS AND RECOMMENDATIONS

### 5.1 Conclusions

Chapters 2-4 investigate the corrugation development with a 3D dynamic FE vehicle-track coupled model and rail material damages from corrugation. These studies address the research questions raised in Chapter 1.

*Q1: With a similar research methodology but different modelling approaches, could the corrugation grow?*

Chapter 2 aims to answer the research question Q1. Previous research with relatively simple models indicated that the corrugation would grow. In contrast, with more complex models in other research, the corrugation did not grow. Thus, we used the 3D dynamic FE vehicle-track model, which was initially developed to find the root causes of rail squats [1] to investigate the corrugation mechanisms further. The differential wear, treated as proportional to the frictional work, is considered the corrugation damage mechanism. All parameters in the system are modelled as the nominal track condition. From the analysis, the following conclusions are drawn:

- The differential wear is in phase with the corrugation in the model, and the corrugation will not grow.
- Through the comparison of main frequency components of differential wear, vertical and longitudinal contact forces, a novel finding is that the corrugation in the initiation stage is more correlated to the longitudinal contact force, which was later identified as being related to the longitudinal track dynamics.
- With the corrugation growth, the vertical track dynamics are more pronounced and tend to be dominant.
- Therefore, it is postulated that the corrugation initiation could be explained by the track longitudinal dynamics, while for the consistent initiation and growth of corrugation, the vertical track dynamics, the longitudinal track dynamics, the contact forces, and the differential wear should be with the same frequency or in other words, the same wavelength.
- This brings new insights to study the corrugation initiation mechanism.

*Q2: When considering the variations of track parameters, could the corrugation initiate and consistently grow? And what is the physical explanation for the corrugation formation mechanism?*

## 5 Conclusions, applications and recommendations

Chapter 3 aims to address the research questions Q2. Following the conclusion in Chapter 2, the next question is how to excite the longitudinal track dynamics to include the corrugation initiation conditions. This research includes an initial excitation in the 3D dynamic FE vehicle-track coupled model when the wheel is rolling over the smooth rail. The initial excitation is activated by variations in the modelling of the fastening system. Due to the initial excitations, the longitudinal contact forces show large amplitude vibrations in the short pitch corrugation wavelength range, and initial differential wear with a similar distribution in spatial and frequency domains is observed. The main conclusions are as follows:

- A hypothesized process for consistent corrugation initiation and growth is proposed and verified with numerical simulation.
- An initial excitation determined by railpad modelling is identified, which causes the high amplitude initial differential wear with main wavelength components in the range of short pitch corrugation.
- The initial differential wear is correlated with the longitudinal contact force. It has the same wavelength as the longitudinal contact force but with a slight phase difference.
- The corrugation from the initial differential wear was shown to initiate and consistently grow when the peak-to-trough distance is above 80  $\mu\text{m}$ .
- When the peak-to-trough distance continues to increase up to 160  $\mu\text{m}$ , the differential wear becomes in phase with the corrugation, which means the corrugation cannot further grow.
- Rail longitudinal compression modes cause corrugation. Contributions from vertical rail vibration, rail longitudinal sheared vibration and rail inclination are insignificant.
- Once the initial corrugation due to the initial excitation occurs, the continuous growth of the corrugation depends on the consistency in the wavelength and phase of the differential wear caused by both the initial excitation and the existing corrugation. If the differential wear caused by both the initial excitation and the existing corrugation has the same wavelength and a phase so that it adds to the existing corrugation, the corrugation can continuously and consistently grow.
- Multiple wavelength components can co-exist in the differential wear, the resulting corrugation, and the longitudinal and vertical contact forces. They are consistent when the corrugation is below a certain limiting amplitude. The limiting corrugation amplitude differs for different wavelength components.

## 5 Conclusions, applications and recommendations

---

- The consistency condition also means a wavelength selection mechanism of the corrugation: (a) only those wavelengths that satisfy the consistency can cause the corrugation; (b) components of longer wavelength have a lower limiting corrugation amplitude.
- It is observed that the amplitude of differential wear per wheel passage decreases with increasing corrugation amplitude when the corrugation is below limiting amplitude.

*Q3: How is the influence of the corrugation on rail material damages?*

Chapter 4 attempts to address the research question Q3. When wheels roll over rails with corrugation, impact vibrations are excited, and dynamic contact forces are amplified. The corrugation peak experiences higher contact forces than that at the corrugation trough. As a result, plastic deformation, work hardening, and material structural changes occur at the corrugation peak. Therefore, a metallurgical examination was conducted to study the mechanical property and microstructural features of the corrugated rail material. The conclusions are as follows:

- Similar to previous research, higher hardness is found at the corrugation peak.
- Microstructural features at the corrugation peak show that besides the commonly identified WEL, a possible new anti-etching layer was observed, i.e., the brown etching layer (BEL), due to its contrast under the optical microscopy.
- A significant feature of the BEL is that cracks can penetrate the BEL and grows vertically without branching. This can result in a rail fracture if no remedies are undertaken.
- The cause of the BEL due to the short pitch corrugation is another concern for both researchers and railway infra managers to get the corrugation problem under control.

To sum up, through the research into the mechanism of corrugation, the formation mechanism behind the enigma is understood. Some parameters which can influence the corrugation formation are also investigated. The material structural change due to the corrugation is understood with a new insight concerning the observation of the BEL. The research results can be used to optimize track parameters to avoid corrugation.

### 5.2 Applications of research findings

The variation of the railpad model in Chapter 3 shows that the corrugation can be reproduced with certain railpad models (representing the fastening system). This gives

insight into the corrugation control strategy by optimising relevant track components, such as the fastening system. With a parametric study, the FE vehicle-track numerical approach can provide some theoretical support to track design to suppress corrugation. Besides the fastening system, there could be some other components contributing to other types of corrugation or rail defects. The same or similar approach can be employed to evaluate the components parameters and their compatibility and optimize the design of the track structure as a whole.

### 5.3 Recommendations for future research

The study in the dissertation gives an insight into the mechanism of corrugation. There are several recommendations to extend the current work in future research with more practical considerations.

Through the variation of fastening (railpad) modelling, the corrugation initiation from the smooth rail is successfully reproduced, and the mechanism of corrugation is concluded as longitudinal rail dynamics. It should be noted that there could be other influential parameters, as well. Therefore, an extensive parametric variation study [2] should be implemented in future research to identify those relevant parameters for corrugation formation. Secondly, the current results explain a type of corrugation recorded from the Dutch railway network, while in the real world, there are many different types of corrugations, and the root causes could differ. Therefore, we should be cautious when extending this explanation to a different type of corrugation. Thirdly, knowing that fastening modelling contributes to corrugation formation, future research can focus on how to optimize the fastening design and from which to avoid or mitigate corrugation should be investigated. This can be practically employed to mitigate the corrugation problem.

### References

- [1] Li Z, Zhao X, Esveld C, Dollevoet R, Molodova M. An investigation into the causes of squats—correlation analysis and numerical modelling. *Wear* 265 (2008) 1349–1355.
- [2] Oyarzabal O, Gomez J, Santamaria J, Vadillo EG. Dynamic optimization of track components to minimize rail corrugation. *J Sound Vib* 319 (2009) 904–917.



## ACKNOWLEDGEMENT

在 Delft University of Technology (TU Delft) 的生活和学习即将结束了，在此静下来写一些话来给这段即使看上去不算完美的经历画上一个完美的句号——不留遗憾。数年博士生涯，中间多少崎岖坎坷、苦辣酸甜，不想有太多倾诉，冷暖自知；漫漫数载，经历了很多终身难忘的人和事，记录下来，以表我最诚挚的感谢！

Firstly, I would like to thank my daily supervisor and promotor, Prof. Zili Li, who gave me the opportunity to do my research at TU Delft and provided me support all these years. Thank you for your patience in spending the time on my papers and the final dissertation. Without your guidance, I could not finish my PhD research.

I am grateful to Prof. Rolf Dollevoet, who became my co-promoter since 2013. Thank you for your support, advice, and encouragement during my research. I also want to thank Prof. Andre Molenaar, who was my promotor and supervised me for the first two years.

My special and sincere thanks go to Dr. Alfredo Núñez for his effective and valuable help in preparing and editing the research papers and the final dissertation. He is intelligent, patient, and efficient in giving his feedback and constructive comments. I sincerely appreciate the memorable discussions with him.

I want to thank Jacqueline Barnhoorn, secretary of the Railway Engineering Section, for her kind help in daily issues. I also want to thank Sandra Ransdorp, the former executive secretary of Department Engineering Structures.

In addition, I would like to thank my friends and colleagues during my research and work. They are Xin Zhao, Maria Molodova, Nico Burgelman, Zilong Wei, Maider Oregui, Jan Moraal, Xiangyun Deng, Chang Wan, Haoyu Wang, Lizuo Xin, Zhen Yang, Xiangming Liu, Yuewei Ma, Zhiwei Qian, Chen Shen, Li Wang, Hongrui Wang, Siamak Hajizadeh, Meysam Naeimi, Anthonie Boogaard, Ali Jamshidi, Omid Hajizad, Jurjen Hendriks, Pan Zhang, Yunlong Guo, Chunyan He from the section of Railway Engineering, Gang Liu, Mingliang Li, Jingang Wang, Dongya Ren from the former section of Road and Railway Engineering, and Bas Beltman, Jeroen Staman, Stijn Stuart, Jeroen Reimerink, Martin Sunter, Ruben Nauw, Jacques de Flem, Pierre-Emmanuel Rabec, Oscar Sijberden, Loek Wisseborn, Frank Vermeulen, and Shulin Gao from Eurailscout Inspect & Analysis. With your help and companion, my research and working life become easy and beautiful.

I would also like to express my gratitude to the visiting Chinese scholars for spending pleasant moments together and for sharing their either research or life experience. They are Ziquan Yan, Yu Zhou, Pingrui Zhao, Rong Chen, Hongqin Liang, Fuhai Li, Yun Huang, Qian



## Acknowledgement

---

Xiao, Xiubo Liu, Xianmai Chen, Zhigang Liu, Lei Xu, Zhiwei Han, and Wenqiang Liu. I am also grateful to my friends Yiming Li, Wanpeng Song, Jianfeng Liu, Xiaoyong Li, Fei Zhang, Xiaotao Ding, Xiwu Zhang, Xiaoman and Ko Oldekamp for giving me help, support, and encouragement before and during my PhD research.

Last but not least, my sincerest gratitude goes to my family and especially my wife Cancan Sun, for their persisting support and patience on me.

## CURRICULUM VITAE

**Shaoguang Li**

Born in Henan province, PR China

-----

### EXPERIENCE

- |                |   |
|----------------|---|
| 2018.10–now    | Railway specialist at Eurailscout Inspection & Analysis B.V.                  |
| 2015.10–2018.9 | Postdoc at the section of Railway Engineering, Delft University of Technology |
- 

### EDUCATION

- |                |   |
|----------------|---|
| 2010.10–2015.9 | PhD candidate at the section of Railway Engineering, Delft University of Technology                                 |
| 2008.9–2010.7  | Master of Mechatronics at the faculty of Mechanical Engineering and Automation, Northeastern University             |
| 2004.9–2008.7  | Bachelor of Mechanical Engineering at the faculty of Mechanical Engineering and Automation, Northeastern University |
- 

### RESEARCH PROJECT EXPERIENCE

1. Development of Axle Box Acceleration (ABA) measurement system for detection of rail defects;
2. European project PM'n'IDEA for using ABA measurement system to detect the loosening bolts of fish plates;
3. EU Horizon 2020 programme: NeTIRail, for investigation on the mechanisms of rail corrugation.
4. Open research fund of Ministry of Education (MOE) Key Laboratory of High-speed Railway Engineering, Southwest Jiaotong University: High-speed wheel-rail contact and mechanisms of short pitch corrugation and control strategy



## LIST OF PUBLICATIONS

1. Li Z, **Li S**, Zhang P, Núñez A, Dollevoet R. Short Pitch Corrugation Formation Mechanism with A 3D Transient FE Vehicle-Track Model: Consistency in Initiation and Growth. Submitted to a journal.
2. Wang L, Wang P, Chen R, **Li S**, Li Z. Hyperelastic Modelling of Elastic Poured Compound Used in Metro Embedded Rail System. Submitted to a journal.
3. Zhang P, **Li S**, A Núñez, Z Li. Vibration modes and wave propagation of the rail under fastening constraint. *Mechanical Systems and Signal Processing* 160 (2021) 107933.
4. Liang H, Li W, Zhou Z, Wen Z, **Li S**, An D. Investigation on Rail Corrugation Grinding Criterion Based on Coupled Vehicle-Track Dynamics and Rolling Contact Fatigue Model. *Journal of Vibration and Control* (2021) doi:10.1177/1077546321989201.
5. Zhang P, **Li S**, A Núñez, Z Li. Multimodal dispersive waves in a free rail: numerical modelling and experimental investigation. *Mechanical Systems and Signal Processing* 150 (2021) 107305.
6. Wang L, Wang P, Chen R, **Li S**, Li Z. Experimental and numerical investigation of damage development in embedded rail system under longitudinal force. *Engineering Failure Analysis* 114 (2020) 104590.
7. **Li S**, Li Z, Núñez A, Dollevoet R. New insights into the short pitch corrugation enigma based on 3D-FE coupled dynamic vehicle-track modelling of frictional rolling contact. *Applied Science* 7 (2017) 807.
8. **Li S**, Wu J, Petrov RH, Li Z, Dollevoet R, Sietsma J. “Brown etching layer”: a possible new insight into the crack initiation of rolling contact fatigue in rail steels? *Engineering Failure Analysis* 66 (2016) 8–18.
9. Naeimi M, **Li S**, Li Z, Wu J, Petrov RH, Sietsma J, Dollevoet R. Thermomechanical analysis of the wheel-rail contact using a coupled modelling procedure. *Tribology International* 117 (2017) 250-260.
10. Oregui M, **Li S**, Núñez A, Li Z, Carroll R, Dollevoet R. Monitoring bolt tightness of rail joints using axle box acceleration measurements. *Structural Control and Health Monitoring* 24 (2016) 1-15.
11. **Li S**, Núñez A, Li Z, Dollevoet R. Automatic detection of corrugation: Preliminary results in the Dutch network using axle box acceleration measurements. *ASME/IEEE Joint Rail Conference* 56451, V001T01A023.
12. Wu J, Petrov RH, **Li S**, Li Z, Godet S, Malet L, Sietsma J. Characterization of structural change in rail surface using advanced automatic crystallographic orientation microscopy. *WIT Transactions on The Built Environment* 162, 367-376.